



**Biomimetic models – The support of cell
membranes on Micro Cavity Arrays**

By

Shane Maguire, B.Sc. (Hons)

A thesis submitted to Dublin City University for the award of MSc.

Supervisor:

Prof. Tia Keyes

Declaration

I hereby certify that this material, which I now submit for assessment on the programme of study leading to the award of MSc. is entirely my work, that I have exercised reasonable care to ensure that my work is original, and does not to the best of my knowledge breach any laws of copyright, and has not been taken from the work of others and to the extent that such work has been cited and acknowledged within the text of my work.

Signed: *Shane Maguire*

ID No.: 12328361

Date: 28/04/2021

Acknowledgements

First and foremost, I'd like to acknowledge the contribution of my supervisor, Professor Tia Keyes for her guidance, patience and encouragement over the last two years. I'd like to thank the technical staff in the School of Chemical Sciences and Josephine for everything and for keeping the day to day running of the facilities seem so effortlessly.

I would like to extend my sincere gratitude to the Keye's research group for all their support and to all of my mates for keeping me grounded throughout the years.

Finally, I would like to thank my family; Mum, Dad, Sinéad Niamh and Éadaoin for support and love, I strive to be better for you.

Table of contents

Acknowledgements	iii
Table of contents	iv
Abstract.....	vi
Abbreviations.....	viii
1.1 Self-Assembled Monolayers.....	2
1.2 Surface functionalisation	5
1.3 Physiochemical Characterisation of the SAMs	7
1.4 Applications of Self-Assembled Monolayers.....	10
1.5 Introduction into Model Lipid Bilayers	12
1.5.1 Membrane models	15
1.5.2 Lipid Vesicles	16
1.5.3 Black Lipid Membranes	18
1.5.4 Single Lipid Bilayers	19
1.5.5 Modified Supported Lipid Bilayers (SLBs)	20
1.6 Introduction to Gold arrays supported lipid bilayers.....	21
1.7 Electrochemical assessment of Lipid membranes	24
1.8 Conclusions	29
1.9 References.....	30
Chapter 2: The impact SAM on Bilayer formation and stability at lithographically prepared microcavity arrays	43
2.0 Introduction	44
2.1 Instrumentations	45
2.1.1 Scanning Electron Microscopy.....	45
2.1.2 Cyclic Voltammetry	46
2.1.3 Electrochemical Impedance Spectroscopy	47
2.1.4 Langmuir-Blodgett	49
2.1 Materials and methods.....	52
2.1.1 Materials	52
2.1.2 Methods	52
2.2 Results and Discussions.....	59

2.2.1 Comparison of solution deposition and μ CP functionalisation methods at planar gold surfaces	59
2.2.1 Characterisation and functionalisation of Gold microcavity Arrays by μ CP method	62
2.2.2 Electrochemical Impedance Spectroscopy of Lipid membrane on gold arrays	67
2.2.3 Determination of Lipid Bilayer formation and stability	73
2.3 Conclusions	79
2.4 References.....	80
Chapter 3: The impact SAM on Bilayer formation and stability at two-photon polymerised prepared microcavity arrays	85
3.0 Introduction	86
3.1 Methods and methods.....	87
3.1.1 Materials	87
3.1.2 Methods	87
3.2 Results and Discussion	90
3.2.1 Optimisation of cavity for SERs.....	90
3.2.2 Characterisation and functionalisation of two-photon polymerised microcavity array.....	93
3.2.3 Electrochemical Impedance Spectroscopy of Lipid membrane on a printed array	97
3.2.4 Determination of Lipid Bilayer formation and stability	101
3.3 Conclusions	106
3.4 References.....	107
Chapter 4: Future applications of microcavity array platform	110
4.1 References.....	115

Abstract

Cell membrane models are highly sought after to depict a realistic representation of the behaviour of the bilayer lipid membrane without the complexity of the living membrane. Biomimetic models can be used to understand the dynamic processes at the cell membrane of a cell, such as drug permeability, membrane signalling, and protein-membrane interactions across biology.

This thesis examines the impact of both substrate fabrication method and self-assembled monolayer (SAMs) identity on the stability of microcavity array supported lipid bilayer, on two separate microcavity array platforms. The presented study investigates the gold electrochemically deposited microcavity arrays and their capacity, after aqueous filling to support lipid bilayer membranes using lipid bilayer assembly methods previously reported. The impact of SAMs with varying end termini at two different types of microcavity array platforms on membrane stability was examined. Membrane stability was explored using electrochemical impedance spectroscopy (EIS) while membrane presence and formation was confirmed using Raman spectroscopy and cyclic voltammetry (CV).

Chapter 1 gives a background to the thesis. The chapter introduces SAMs, describes their basic properties and the impact they can exert on a metal interface and then discusses the different types of cell membrane models currently applied. It also covers the electrochemical methods used in this thesis to assess monolayer assembly and the lipid bilayers. Limitations of the current models are described with respect to stability.

Chapter 2 investigates the use of SAM with differing end termini on polystyrene sphere templated electrochemically deposited microcavity array supported lipid bilayer (MSLB).

Fabrication methods are described for electrochemically mesopore arrays and their functionalisation with 6-mercapto-1-hexanol, hydroxyl-terminated polyethylene glycol (PEG) thiol and 6-mercaptohexanoic acid SAMs using microcontact printing (μ CP). These modified arrays were investigated as whether they could support stable lipid bilayers prepared using the Langmuir-Blodgett method to form the first monolayers followed by vesical disruption to form a lipid bilayer.

In Chapter 3, an alternative microcavity array platform was fabricated using a two-photon polymerisation technique and its ability to support a lipid bilayer was examined as a function of SAM support using μ CP as a functionalisation method. DOPC membranes were successfully spanned across a microcavity array platform through μ CP using the same SAMs used in chapter 2.

Overall, this thesis demonstrates a new way to selectively modify the top surface of the gold cavity arrays using different types of substrates using 6-mercapto-1-hexanol, hydroxyl terminated PEG thiol and 6-mercaptohexanoic acid. Through EIS the stability of lipid bilayers on MSLBs using different SAMs with different end terminus on both was assessed on both sphere lithography electrochemically deposited and two-photon polymerisation fabricated microcavity arrays.

Abbreviations

μCP – microcontact printing

AC – Alternating current

AFM – Atomic force microscopy

AIPS - Amphiphilic invertible polymers

BLM – Black lipid membrane

CV – Cyclic voltammetry

DLW – Direct laser writing

DOPC – 1,2-dioleoylsn-glycero-3-phosphocholine

ECM – Equivalent circuit model

EIS – Electrochemical impedance spectroscopy

FDTD – Finite different time domain

HDT – Hexadecanethiol

Hr - Hour

LB - Lipid bilayer

LM – Liquid metals

LUV – Large unilamellar vesicles

MEF – Metal enhance fluorescence

MLV – Multilamellar vesicles

MSLB – Microcavity supported lipid bilayer

OTS – Octadecyl trichlorosilane

PBS – Phosphate buffer saline

PCA – Principal Component Analysis

PDA – Polydopamine

PDMS – Polydimethylsiloxane

PEG – Polyethylene glycol

PGMEA – Propylene glycol monomethyl ether acetate

SAM – Self-assemble monolayer

SERS – Surface enhanced raman spectroscopy

SLB – Supported lipid bilayer

STM – Scanning tunnelling microscopy

SUV – Small unilamellar vesicles

THF – Tetrahydrofuran

ToF-SIMS – Time of flight Secondary Ion Mass Spectrometry

UV – Ultraviolet

XPS – X-ray Photoelectron Spectroscopy

Chapter 1: Introduction

1.1 Self-Assembled Monolayers

Microcavity supported lipid bilayers (MSLBs), figure 1.1 have emerged in recent years as very valuable models of the cell membrane, possessing the fluidity of a liposome with the versatility and addressability of solid supported lipid bilayer (SLB). Firstly, this research compares solution deposition and microcontact printing (μ CP) methods as functionalisation methods of self-assembled monolayer (SAM) deposition methods. Different SAM end termini were assessed for supporting lipid membranes on two different substrates using cyclic voltammetry followed by SAM and lipid membrane stability on microcavity array platforms, using electrochemical impedance spectroscopy (EIS).

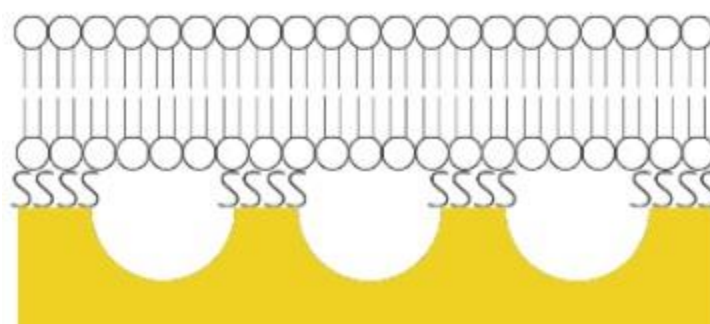


Figure 1.1: Representation of a lipid membrane supported on a microcavity array platform.

SAMs are ordered molecular assemblies formed through the adsorption of a surface active molecule on a solid surface. SAM assemblies are formed spontaneously onto a substrate through adsorption to form ordered domains.¹ Most commonly, SAMs are prepared using thiol derivatives adsorbed at a metallic substrate such as gold, silver and other non-precious metals. Gold is the most investigated metallic substrate for SAMs having elevated affinity for thiols leading to stable SAMs from days to weeks with a bond energy between gold and thiol (H_2S) being 19.98 KJ/ mol, while between silver and thiol (H_2S) is 7.98 KJ/ mol.^{2,3}

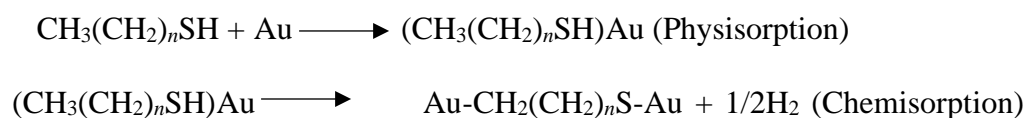
The preparation of thiol-layers on gold is straightforward as SAM formation occurs spontaneously through adsorption from either the vapor or liquid phase.

SAMs have been used for patterning purpose by using different techniques such as micro contact printing (μ CP), scanning probe lithography and photo-induced patterning. μ CP is a low-cost process for producing a SAM and can be applied as a pattern with a submicrometer lateral dimensions.⁴

SAMs have most commonly been assembled on silver, copper, platinum, palladium, and nickel surfaces. Nickel, silver, and copper surfaces can be easily oxidized, but this can be controlled by the use of self-absorbing monolayers. Gold metal surfaces adsorb sulfides (R-S-R), disulfides (R-S-S-R), and thiol groups (R-SH) because of their sulfur donor atoms.

There are several examples of surface active agent interactions which include gold–thiol monolayers, due to formation of the strong S–Au bond. Commonly studied monolayers comprise selenols on silver, alkyl phosphonates on zirconium, fatty acids on metal oxide surfaces and alkyl trichlorosilane layers on hydroxylated surfaces.⁵ The adsorbed monolayer formation is further stabilized and orientated by self-assembly which occurs as the side chains or backbone such as the methylene groups coupled laterally through Van der Waals interactions.⁶

Ulman examined the adsorption kinetics of thiol to gold surfaces.⁶ Physisorption was found to occur and spontaneously in the assembly of alkanethiols on Au(111) substrate via Van der Waals interactions. After physisorption in equation 1.1, the thiol head group is chemisorbed onto the gold surface via the sulfur head group (Au-S). The Au-S bonds can hinder the transition from the molecular orientation adsorbed horizontally to a vertical orientation, particularly for short dithiols, that have lower energy to gain from chain–chain interactions.⁷



Equation 1.1

For the two distinct steps that occur in the alkanethiol-gold process, the initial fast adsorption step, takes just a few minutes and the assembly process is much slower, taking several hours. The first stage comprises of the rapid adsorption of thiol to the edge and corner sites of gold surfaces, resulting in surface Au-Au bond length relaxation and distinct gold-to-ligand charge transfer. The second step which is much slower could be described by the Langmuir kinetics equation.⁸

Numerous factors, including temperature and solvent can affect kinetics of SAM formation. For the solution deposition method, Rozlosnik et al. changed the solvent polarity and the concentration of octadecyl trichlorosilane (OTS). He discovered that the use of OTS in heptane as a solvent encourages full-coverage self-assembled monolayer on hydrophilic silicon oxide over a broad range of concentrations (25 M to 2.5 mM) and humidities. AFM, X-ray reflectometry, and ellipsometry were used to analyse the self-assembled layers that resulted in multi-layered films resulting from the deposition of OTS from dodecane solutions.

Through the use of heptane as a solvent, on the other hand, resulted in the creation of high-quality monolayers. It was discovered that the influence of solvents (dodecane and heptane) and conditions on the formation of OTS layers on Si/SiO₂ surfaces was consistent and repeatable.⁹ Other factors include the structure and concentration of adsorbent, which affect SAM surface coverage and the substrate cleanliness, affecting the overall kinetics of SAM formation. Initially, sulphur from the alkanethiol binds to the gold substrate, the alkyl chain sits at an angle from the headgroup to that of the gold surface.

The angle is dependent on various factors such as the packing density on the substrate surface, the alkanethiol head group, and the interactions between the chains themselves. The degree of freedom on the molecular backbone changes its conformation.¹⁰

1.2 Surface functionalisation

The traditional and most common methods of surface functionalisation of a metal surface by alkane thiols is through solution deposition which involves placing gold or gold-coated substrate in a solution, typically an alcohol, containing the adsorbate alkanethiol, overnight.^{7,8}

Deposition concentrations vary across reports but are usually between 1 mM and 1 μ M and deposition times typically run from 12 to 24 hours. An alternative method for adsorption which is much faster, and offers the opportunity for patterning is microcontact printing μ CP as well as that the adsorption from a gas phase in ultrahigh vacuum.¹¹

The μ CP technique involves using a polydimethylsiloxane (PDMS) template to form patterns of SAMs on the surface on the substrate. The stamp is 'inked' with a solution of an alkanethiol in ethanol, and is dried prior to being brought into contact with gold substrates as seen in figure 1.2.

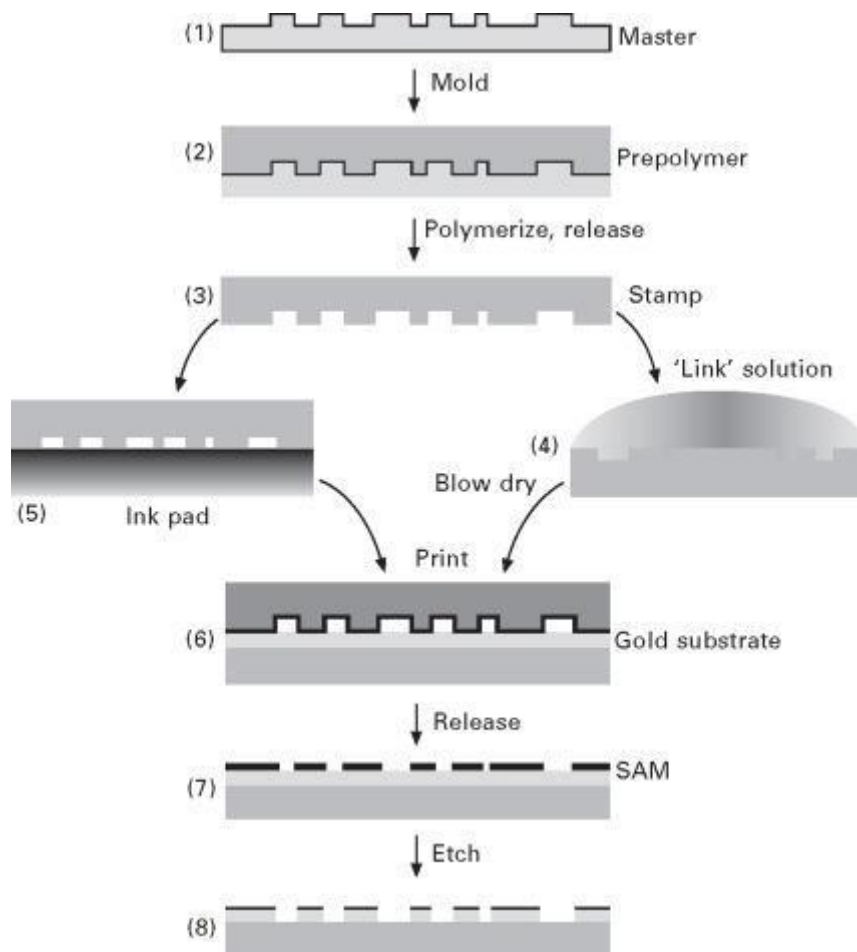


Figure 1.2: Diagram representation of the μ CP process.¹²

μ CP is used to produce a hydrophilic polydopamine (PDA) pattern with micrometre resolution. A compact PDA thin film is first developed on the hydrophobic surface during μ CP. The PDA-coated surface is put in contact with an active PDMS stamp. After the removal of the PDMS, the hydrophobic surface has a PDA pattern that is analogous to the stamp.⁹

Yalcintas et al. describes the use of μ CP method for producing liquid gallium alloy-based soft and bendable electronics in a repeatable manner. Integrating liquid metals (LM) into an elastomer matrix is one of the most popular ways to produce soft and bendable electronics. A variety of parameters affect SAM formation including deposition concentration and the duration of contact of the substrate with the gold surface.^{9,10,13} The movement from the substrate to the gold surface comprises an initial diffusion of thiols to the gold interface.

The diffusion of the thiols from the edges of the substrate across the gold surface is followed by the vapor transport through the gas phase. However, each of these mechanisms that form SAMs, either through contact with the substrate, or not, is not entirely understood.¹⁰

1.3 Physicochemical Characterisation of the SAMs

Adsorption of a molecular monolayer at a substrate's interface can profoundly alter the physicochemical properties of that interface. The affected parameters include hydrophobicity/hydrophilicity, wettability, charge, electrochemical resistance and refractive index. The SAM packing density controls the surface hydrophobicity rather than the chain length.¹⁴ The impact of packing on the surface hydrophobicity is directly associated with the alternation of the chain flexibility and surface roughness. Few SAMs are completely continuous, there are usually microscopic/nanoscale areas where SAMs fail to form and these are known as pinholes or as defects. The surface roughness of the underlying substrate can play a role in the extent to which these regions of discontinuity occur. As pinhole or defect allow electrolyte to the electrode surface, they can be interrogated electrochemically and can for example be observed as an increase in the capacitive current. Figure 1.3 shows commonly reported SAMs with varying headgroups, chain structures, and end groups.¹⁵

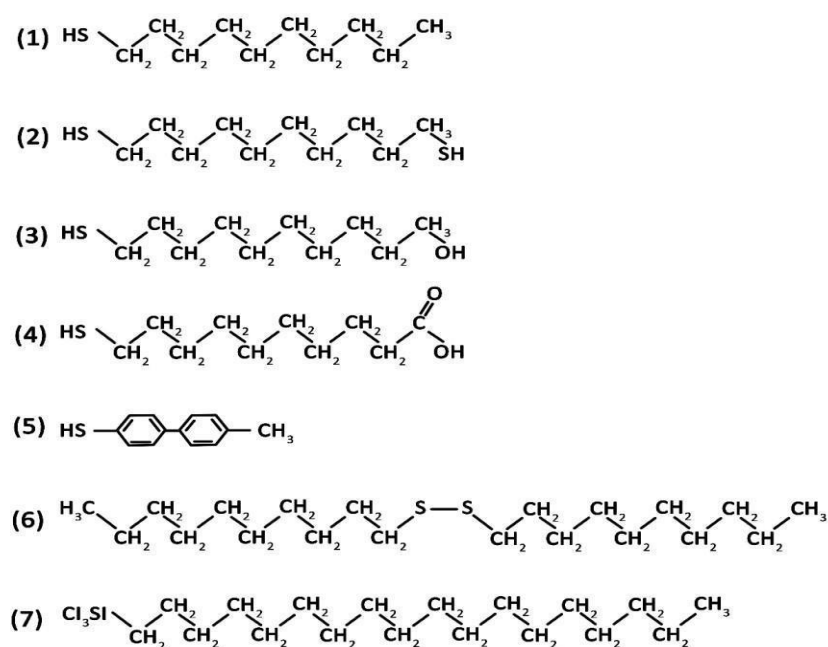
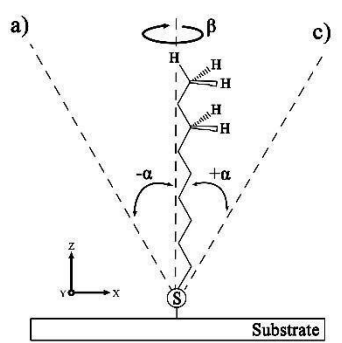


Figure 1.3: Frequently used compounds for SAMs with differing headgroups, chain structure, and end groups.¹⁵

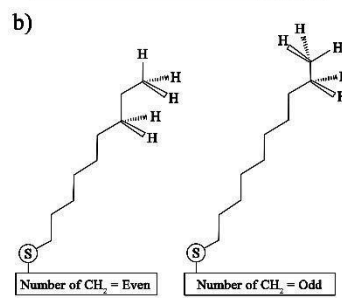
In this thesis, two hydroxyl terminated functional groups, and carboxylic acid terminated functional group are assessed to improve the stability of lipid molecules on two differing gold substrates. They are employed with these functionalities as a hydrophilic interface is required to support a bilayer with proper orientation where the hydrophilic interface orients outward with a hydrophobic core.

The physiochemical properties of alkanethiol-based SAMs have been studied on a variety of substrates; for instance, Laibinis et al. compared alkanethiolated SAMs formations on gold, silver, and copper substrates. It was found that substrates impacted the physicochemical properties of the films having varying angles of orientation, for instance silver and copper has $\sim 13^\circ$ on gold having $\sim 28^\circ$.¹⁶ The tilt angle, α , governs the orientation of molecules of the linear backbone relative to the surface and β , which is the angle of rotation can range between 0° - 90° which the long axis of molecules can rotate.¹⁷ As seen in table 1.1, alkanethiols on gold surfaces have a tilt angle close to that of 30° with an average angle of rotation close to 50° . Dependent on the substrate and the headgroup packing density, the average spacing between the hexagonal gold lattice surface and the alkanethiols is 5.0 \AA .

Table 1.1: (A) schematic representation of the tilt angle, α , to the surface with the angle of rotation β , to the surface. (B) demonstration of how the backbone changes the conformational shape of the individual molecule and α and β . (C) change in α and β contact angle for the alkanethiols depending on the substrate.¹⁸



a) Schematic representation of a SAM molecule on a substrate. The substrate is a horizontal plane. A sulfur atom (S) is bonded to the substrate. A chain of carbon atoms (C) is attached to the sulfur. The chain is oriented at an angle α relative to the substrate. The chain is also rotated around its own axis by an angle β . A coordinate system (x, y, z) is shown with the z-axis perpendicular to the substrate.



b) Demonstration of how the backbone changes the conformational shape of the individual molecule and α and β . Two molecules are shown: one with an even number of CH_2 groups and one with an odd number of CH_2 groups. The even number of CH_2 groups results in a more extended conformation, while the odd number of CH_2 groups results in a more compact conformation.

Molecular Constituent of SAM	Substrate	Tilt Angle (α)	Chain/Plane Rotation (β)	Characterization Method	Reference	
<i>n</i> -alkanethiols	Au(111)	28°	53°	RAIRS	26	
	Au(100)	14°	70°	RAIRS	27	
	Ag		$11-14^\circ$	45°	RAIRS	26
			$13\pm 2^\circ$	$44\pm 6^\circ$	RAIRS	27
			15°	45°	Surface Raman Scattering	151
					RAIRS	26
	Cu	12°	45°	RAIRS	26	
	Pd	$16\pm 2^\circ$	45°	RAIRS	30	
	Pt	$<15^\circ$	n.a.	RAIRS	32	
	Hg	0°	n.a.	X-ray scattering	69	
	0°	n.a.	Electrochemistry	284		
	GaAs(100)	$57\pm 3^\circ$	$45\pm 5^\circ$	RAIRS	285	
	InP(100)	$55\pm 6^\circ$	n.a.	XPS	286	
$\text{HS}(\text{CH}_2)_{21}\text{OH}$	Ag	$5\pm 5^\circ$	n.a.	Raman Spectroscopy	287	
	Cu	$5\pm 5^\circ$	n.a.	Raman Spectroscopy	287	
HS-C ₆ H ₅	Au(111)	$49\pm 5^\circ$	32°	NEXAFS	288	
	Ag(111)	$24\pm 5^\circ$	32°	NEXAFS	288	
HS-C ₆ H ₄ -C ₆ H ₅	Au(111)	$15\pm 5^\circ$	n.a.	NEXAFS	289	
	Ag(111)	$18\pm 5^\circ$	32°	NEXAFS	288	

In a close-packed monolayer, the hydrophilicity and wettability of the interface is most strongly influenced by terminal functional groups. Common terminals include ether, alcohol, halides, aldehyde, amide, nitrile, amine, ester, and carboxylic acids can be applied to modulate surface wettability, monolayers can be altered to have aromatics and amide structures.^{17,19} The impact of functional groups on surface wettability has been studied in detail by Tamada, and Lee. In their study contact angles of $102.78^\circ \pm 2.66^\circ$ were found for $-\text{CH}_3$ surfaces.^{19,20} SAMs with $-\text{NH}_2$ and COOH end terminus was found to have contact angles of $68.88^\circ \pm 3.64^\circ$ and $50.13^\circ \pm 1.69^\circ$, respectively. Work carried out by Yadav found that ΔA indicated the hydrophobicity of a SAM surface where higher ΔA values indicated a non-hydrophobic surface.^{16,20,21}

1.4 Applications of Self-Assembled Monolayers

SAM formation on metal surfaces not only has importance in the nano sciences through their study of interfacial phenomena but also broader industrial and commercial applications in promoting corrosion resistance, solar energy, control of wetting and adhesion, bio compatibility, molecular recognition, and sensitization for sensors.^{22,23,24} Examples of their use in controlling interfacial phenomena include control of charge transfer through molecules. Controlled electron transfer is important for a wide range of devices including transistors and photosynthesis and cell immobilisation.^{25,26}

Through their high performance and relative ease of processing as compared to traditional silicon solar cells, dye-sensitized solar cells have sparked recent interest. However, the high cost of platinum for counter electrodes, as well as the high cost and poor throughput of the sputtering technique, have rendered large-scale dye sensitised solar cell development impractical.

Carbon nanotubes and graphene have been tried as counter electrodes, but their poorer conductivity and catalytic behaviour resulted in a lower energy transfer rate as compared to the sputtered platinum electrode.²⁷ However, as opposed to the sputtered platinum electrode, these self-assembled monolayer based counter electrodes have been used with a fraction of the cost of platinum, and the fabrication process can be upgraded, allowing for cost-effective manufacturing of dye sensitised solar cells.²⁸ The current–voltage properties of alkanethiols sandwiched between gold electrodes were investigated by Wang et al. and they were able to differentiate between tunnelling and hopping systems by observing the temperature dependency of the current–voltage relationship.²⁹

SAMs have shown potential as a biodetection platforms. Spampinato et al. for instance have functionalised both planar gold and gold nanoparticles with 1- β -D-thio-glucose for the specific detection of maltose binding protein. Time of flight Secondary Ion Mass Spectrometry (ToFSIMS), Principal Component Analysis (PCA) and X-ray Photoelectron Spectroscopy (XPS) have been used to characterise the surface chemistry of gold substrates both before and after functionalisation with thiol-modified glucose self-assembled monolayers.³⁰ SAMs can offer the opportunity to provide specific ligands from which biomolecules such as cells can bind onto or act as blocking agents for protein adsorption. For instance, mixed SAMs composed of a SAM forming molecule and a ligand-presenting molecule can affect the ligand accessibility and, therefore, affect protein interaction.³¹

1.5 Introduction into Model Lipid Bilayers

The lipid bilayer is a selectively permeable barrier that mediates the exchange of materials between the cell's inner and outer environment. The plasma membrane depicted in figure 1.4, acts as a scaffold for the cell, allowing biochemical reactions to occur, transport of materials along with intercellular signalling.³² Lipid membranes are 6-10 nm in thickness and contain a matrix of phospholipids, sphingolipids, and sterols with about 50% by weight protein. The lipid membrane is an amphiphilic membrane comprised of two layers of lipid molecules containing a hydrophilic, polar phosphate head group and two hydrophobic nonpolar tail groups derived from fatty acids. The tails can differ in length (normally between 14 and 24 carbon atoms) and can also vary in level of saturation. The lipid bilayers (LB) is the barrier that keeps cell contents such as proteins and cell nutrients within the cell. Lipids, proteins, and carbohydrate are the main components of a cell membrane: fluidic structures that surround every cell.

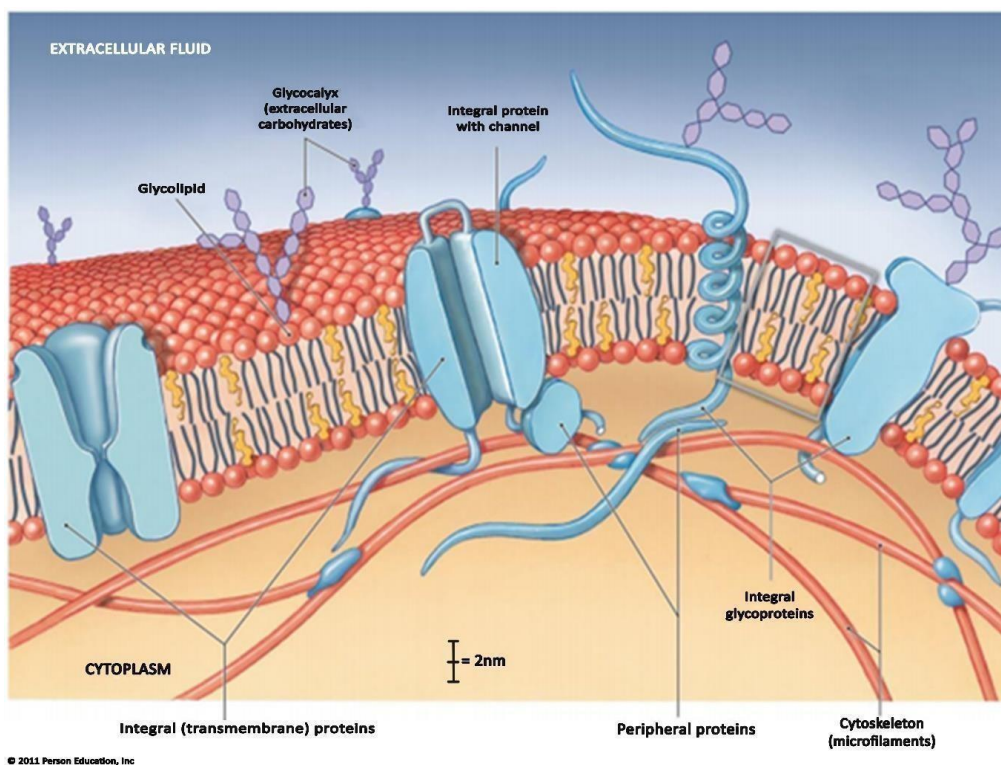


Figure 1.4: Structure of the plasma membrane comprising of a phospholipid bilayer with carbohydrates, embedded proteins, glycolipids, glycoproteins.³³

Lipid membrane associated proteins can be categorised into integral, transmembrane and peripheral proteins. Integral membrane protein, are proteins that are integrated into the membrane either partly or transmembrane proteins which extend from one side of the membrane to the other.³⁴ The domains of integral membrane proteins that span the membrane are hydrophobic in nature while those exposed to the cytoplasm tend to be hydrophilic in nature. Peripheral membrane proteins can be attached to either phospholipids or integral proteins and are found on both the outside and inside of membrane surface.³⁴

Carbohydrates are generally found on the outside surface of cells and are bound to either lipids forming glycolipids or to proteins forming glycoproteins. These carbohydrate chains can range between 2 - 60 monosaccharide units forming distinctive cellular markers.³⁵ Cholesterol molecules orient themselves within the bilayer with their hydroxyl groups orientated towards the polar head groups of the phospholipid molecules. The permeability of the bilayer to small molecules is decreased through decreasing the mobility of the CH₂ groups closest to the polar head groups. A change in cholesterol molar ratio within a cell membrane can have a significant impact on the membranes permeability. A typical DOPC membrane composed of a choline head groups and glycerophosphoric acid along with fatty acids, can have 5 - 6 orders of magnitude higher permeability than realistic lipid composition.³⁵

Membrane fluidity refers to the viscosity of the lipid bilayer of a cell membrane. The packing of the lipids affect its overall fluidity, the diffusion of proteins and other bio-molecules within the membrane. Membrane fluidity is influenced by fatty acid identity and specifically whether fatty acids are saturated or unsaturated. The absence of double bonds in saturated fatty acids decreases the membranes overall fluidity. Unsaturated fatty acids have at least one double bond increasing the membranes overall fluidity.³⁶

As the temperature decreases, the overall phospholipid bilayer fluidity decreases due to the phospholipids clustering more closely together. Conversely at high temperatures, membrane fluidity increases as phospholipids have enough kinetic energy to overcome the intermolecular forces holding the membrane together.³⁶

Phosphatidylethanolamine, phosphatidylserine, sphingomyelin, and phosphatidylcholine are the four main phospholipids present in plasma membranes, responsible for more than half of the lipid in certain membranes.²⁸ The phospholipids are distributed asymmetrically between the membrane bilayer's two parts. The outer leaflet of the plasma membrane is mostly made up of sphingomyelin and phosphatidylcholine, whereas the inner leaflet is mostly made up of phosphatidylserine and phosphatidylethanolamine, as seen in figure 1.5.³⁷

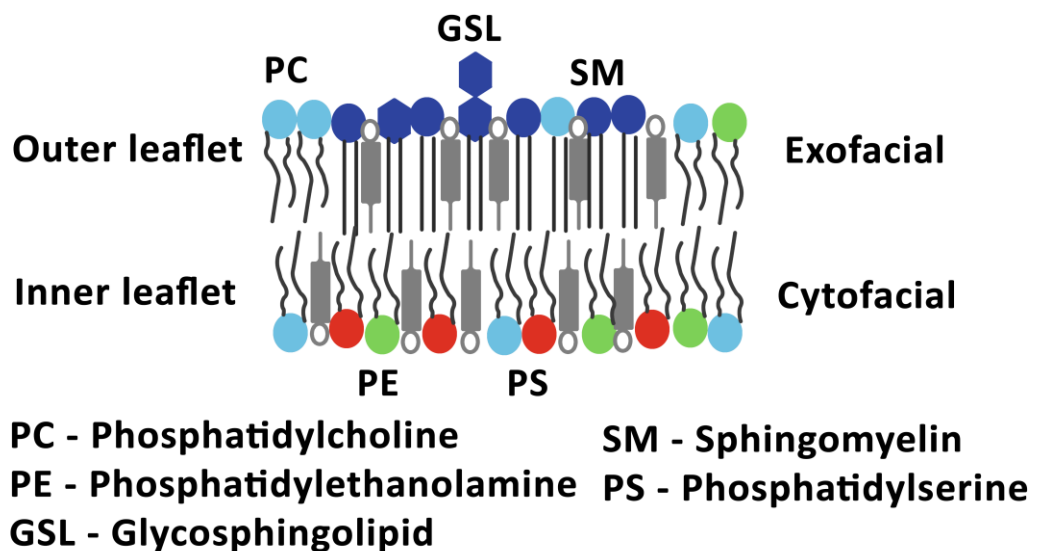


Figure 1.5: Representation of lipid asymmetry in lipid membranes.³⁸

Phosphatidylinositol, a sixth phospholipid, is also contained in the inner half of the plasma membrane. While phosphatidylinositol is a small aspect of the membrane, it plays a critical role in cell signalling. Both phosphatidylinositol and phosphatidylserine have negatively charged head groups, so their prevalence in the inner leaflet resulted in a net negative charge on the plasma membrane's cytosolic face.³⁹

Proteins are responsible for carrying out various membrane functions, while lipids are the basic structural components of membranes. Most plasma membranes are about 50% lipid and 50% protein by weight, with glycolipid and glycoprotein carbohydrate portions responsible for 5 to 10% of the membrane mass. This percentage correlates to around one protein molecule for every 50 to 100 lipid molecules, due to the fact that proteins are much bigger than lipids.⁴⁰

The fluid mosaic model of membrane structure suggested by Jonathan Singer and Garth Nicolson in 1972, is now commonly accepted as the fundamental framework for the arrangement of all biological membranes and are described as two-dimensional fluids in which proteins are incorporated into lipid bilayers in this model.^{41,42}

1.5.1 Membrane models

Table 1.2 describes different model membrane systems that offer invaluable insight into membrane behaviour including understanding drug interactions with complex membrane proteins away from the very great complexity of the living cell.⁴³ Demand for such information has led to many membrane models, including; black lipid membranes, supported lipid bilayer membrane, hybrid lipid membrane, air-stable lipid bilayer membrane, and many more.^{44,45,46,47}

Table 1.2: Description of model membrane systems.³⁴

Model System	Description	Surface-Sensitive Characterization	Electrical Sealing	Membrane Proteins	Air Stability
Lipid vesicles	Freely diffusing vesicles Suspended in aqueous solution	No	Yes	Yes	No
Black lipid Membrane	Lipid bilayer spans an open aperture	No	Yes	Yes	No
Supported lipid bilayer	Two-dimensional lipid bilayer physisorbed on solid support	Yes	Yes	No	Yes
Tethered lipid bilayer	Planar bilayer immobilized on solid support or soft cushion	Yes	Yes	Yes	Yes
Intact vesicle layer	Layer of intact vesicle physisorbed on solid support	Yes	No	Yes	No
Tethered vesicles	Intact vesicles immobilized to solid support or planar bilayer	Yes	No	Yes	No

1.5.2 Lipid Vesicles

The liposome was one of the first cell membrane models and was developed by Dr. Alec Bangham as he imaged gram-negative stained phospholipids using an electron microscope in 1964.⁴⁸ A liposome, as seen in figure 1.6 are artificial vesicles consisting of bilayer membranes. Liposomes offer promising possibilities for drug delivery systems due to their size and hydrophobic and hydrophilic character. The properties of the liposome differ considerably with composition, size, surface charge and preparation method.⁴⁹

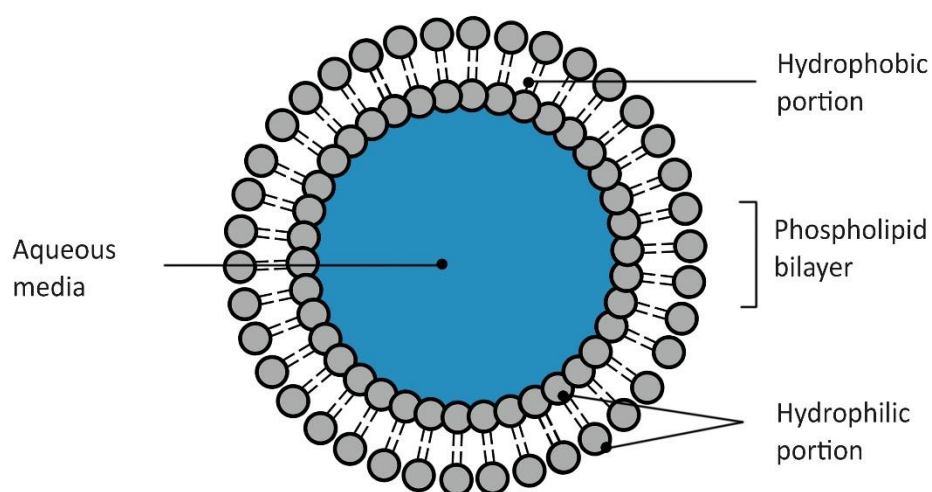


Figure 1.6: Representation of a liposome structure.⁵⁰

The size of the liposome can vary from 0.025 μ m to 2.5 μ m vesicles. On the basis of size and number of bilayers, liposomes can be categorised into two categories: (1) multilamellar vesicles (MLV) and (2) unilamellar vesicles. In unilamellar vesicles, vesicles can be classified into (1) large unilamellar vesicles (LUV) and (2) small unilamellar vesicles (SUVs).⁵¹ The vesicles in unilamellar liposomes have a single phospholipid bilayer sphere while multilamellar liposomes vesicles typically have several unilamellar vesicles formed inside one another.

The preparation of the liposome involves the hydration of dried lipids in a polar solvent, usually water, on a glass surface to form vesicles spontaneously. Multilamellar vesicles (MLV's) which are vesicles ranging from 0.2 - 50 μ m are not ideal cell membrane models due to their lack of biomimicry in multilamellar structure size which prevents molecular binding within the inner leaflet of the bilayer. To achieve MLV's of 20 - 50 nm require extensive sonication and extrusion through a defined pore size polycarbonate filter.

Small unilamellar vesicles (SUVs) are uniform with a single bilayer. They are 50 to 100nm in size. SUVs are formed through sonication or through extrusion through polycarbonate membranes, of MLV. SUVs which are asymmetric in composition can show some variability in size from the extrusion process or sonication.⁵² Alternatively, liposomes can be formed through their rehydration in the presence of an alternating current (AC) electric field. This method results in larger liposomes with a diameter of 10 to 100 μ m, known as giant unilamellar vesicles (GUV's).⁵³ These vesicles have proven useful for monitoring lipid dynamics, membrane fusion, lipid raft formations in addition to protein behavior.^{54,55,56}

Similarly, Bhuvana et al. used 3-mercaptopropionic acid immobilized on 2-dioleoyl-sn-glycerol-3-phosphoethanolamine (DOPE) liposome onto gold nanoparticles and assessed for DNA sensing applications using EIS.^{57,58} However, the liposomes lacked stability on electrode surfaces, which prevented EIS analysis over longer periods. The large size of GUVs makes them amenable to optical imaging but they are usually limited only to fluorescence experiments and imaging techniques due to stability at their interfaces.

1.5.3 Black Lipid Membranes

Black Lipid Membranes (BLM) was first mentioned by Mueller in 1962. These compositions consist of a lipid bilayer, which comprises of a thick annulus that forms across an open pore and the microlens, figure 1.7. As BLM bilayers are only a few nanometres in thickness, it leads them to appear black or grey in optical images. The surface tension required to form these bilayers do not enable long-term stability and only allows the fusion of transmembrane proteins for a very short lift time of approximately 1 hr. Unfortunately, BLMs' retention of solvents and short lifetime make them limited in their applications in studying protein interactions.⁵⁹

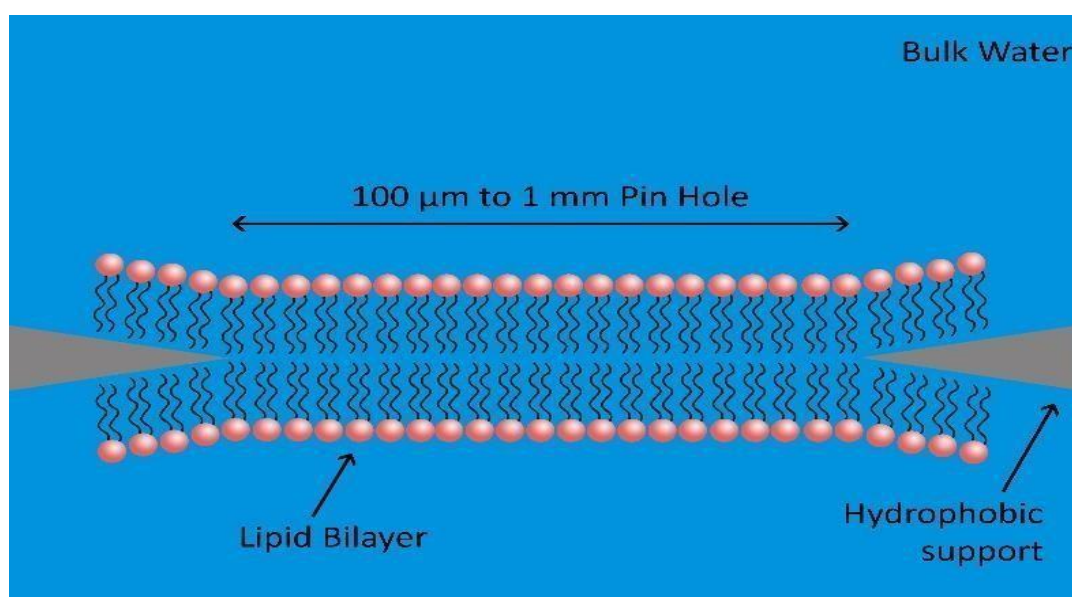


Figure 1.7: Schematic representation of a black lipid membrane.⁶³

1.5.4 Single Lipid Bilayers

The deposition of lipid bilayers onto a planar solid surface results in single lipid bilayers (SLB). This method has proven to be more stable than BLMs, but it requires hydrophilic, smooth, and clean surfaces.⁵³ The three techniques used to create SLBs are seen in figure 1.8. The first method involves using the Langmuir-Blodgett trough in which amphiphilic molecules are transferred from the air/water interface to the substrate. The lower lipid bilayer layer is created through the Langmuir-Blodgett method, while the second layer is created using the Langmuir-Schaefer method. This method is ideal for making asymmetric bilayers; however, the exposure to air in this method makes it unsuitable for incorporating transmembrane proteins. The second method involves the use of small unilaminar vesicles which involves the adsorption of unilaminar vesicles to the surface of the substrate. In this method, the vesicles form a planar supported bilayer by vesicle fusion. The bilayers' quality depends on the vesicle size, roughness, surface charge, ionic strength, solution pH, and osmotic pressure. One method of lipid membrane preparation involves the sonication, and the ultracentrifugation of the liquid suspension, with the other method involves the extrusion of the vesicles through a porous polycarbonate membrane using high pressure. The third method involves combining the first and second methods where a monolayer is formed by using the Langmuir-Blodgett trough and vesicle fusion. This method allows the formation of asymmetric bilayer with transmembrane proteins.⁵⁴

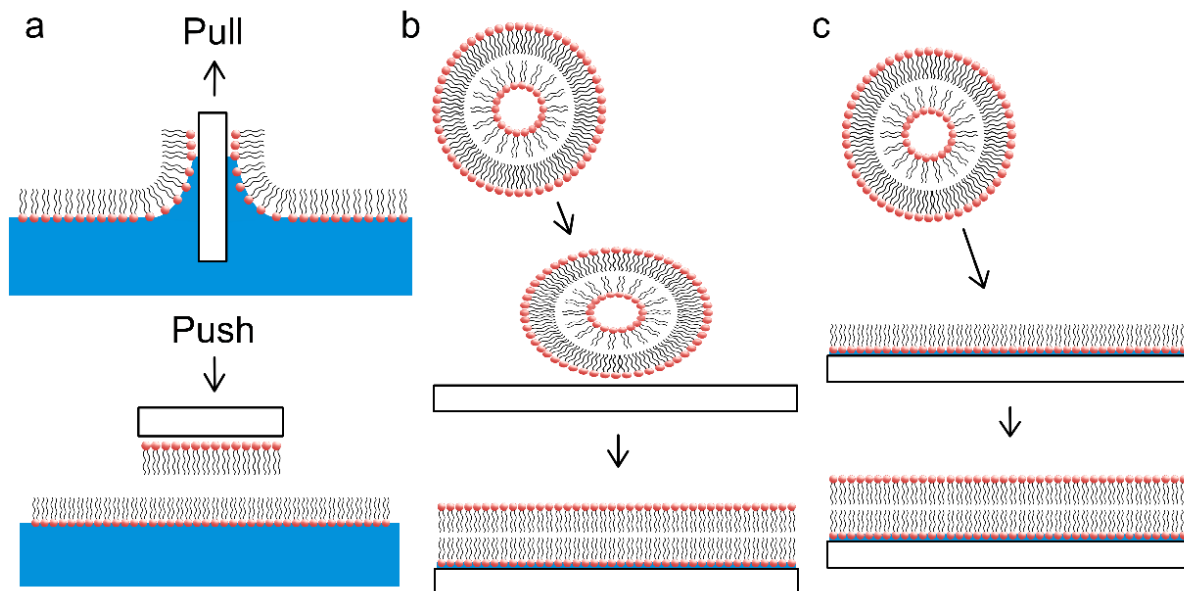


Figure 1.8: Schematic of forming supported lipid bilayers include (a) The Langmuir-Blodgett/Langmuir-Schafer method: initial deposition of a lipid monolayer on the substrate using the Langmuir-Blodgett method. Followed by the formation of a second layer by horizontally dipping the substrate using the Langmuir-Schafer method (b) The vesicle fusion method: it involves the addition of unilamellar vesicles to a hydrophilic substrate and results in the formation of a lipid bilayer (c) Langmuir-Blodgett/Vesicle fusion method: it involves the deposition of a monolayer in the substrate using the Langmuir-Blodgett method followed by the addition of unilamellar vesicles which fuse and forms the bilayer.⁵⁵

1.5.5 Modified Supported Lipid Bilayers (SLBs)

Stability is the fundamental quality of SLBs compared to other models, although a drawback is that SLB membrane interaction with substrates can affect the natural diffusion of membrane and any inserted proteins. These interactions between the substrate and the membrane seriously limit the application of SLBs due to lack of space below the membrane and also through direct surface interactions that can lead to the denaturation or inactivation of protein.⁶⁰ Therefore there is a particular interest in increasing the distance between the membrane and the substrate so that these frictional interactions do not occur. For instance, a dimyristoyl phosphatidylcholine bilayer on a Dextran substrate was found to be stable for seven days.⁶¹

Polymer cushions, as seen in figure 1.9, have been successful in distancing the bilayer from the substrate; however, interactions between the bilayer and the cushion have shown to cause issues similar to an unmodified supported lipid bilayer array with respect to diffusion rates.⁶²

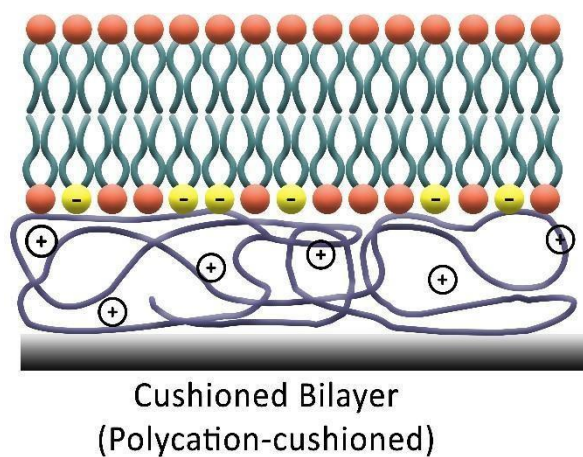


Figure 1.9: Polymer cushioned supported lipid bilayer.⁶³

The modification of substrates by thiols allows the self-assembly of lipids on gold surfaces and increases the distance between the bilayer and the substrate while reducing their frictional interactions.⁶⁴ The introduction of pore-supported lipid bilayers allowed the natural protein interactions and diffusion to occur on freestanding bilayers which do not have contact with the substrate.^{65,66}

1.6 Introduction to Gold arrays supported lipid bilayers

Microcavity array substrates at the micro and nano scale have been developed for sensing applications, surface-enhanced spectroscopy and photonics.^{67,68,69} This project builds upon the use of microcavity arrays to build upon lipid membranes that span across a cavity providing a aqueous interface on both sides of the membrane using different SAMs end termini.

There are several methods to build nanostructured arrays, such as porous alumina templates, electron beam lithography, nanoimprint lithography, and nanosphere lithography. Murphy et al. for instance used porous alumina oxide bound to a glass substrate and through electrodepositing of gold nanorods into pores were able to produce gold coaxial rod-tube nanocavities.⁷⁰ NaOH was used to etch around the rods where the rod's deposition took place, followed by a second treatment of NaOH and additional deposition of gold as seen in figure 1.10. Both the height and diameter of the rods are controlled via both the etching and electrodepositing time.

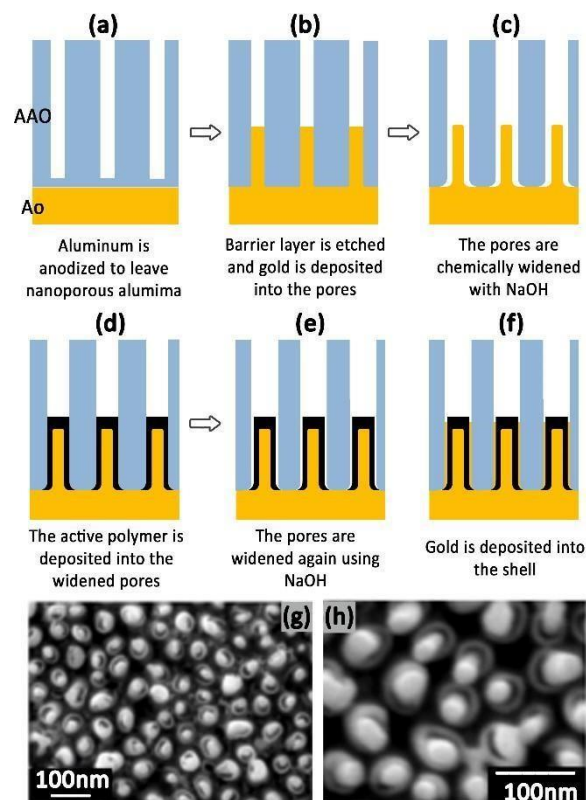


Figure 1.10: Fabrication of gold nanocavities using porous alumina.⁷⁰

Bartlett et al. also used the electrodeposition of gold under potentiostatic conditions at - 0.95 V using a saturated calomel reference electrode to fabricate cavities with diameters of 210 nm on lyotropic liquid crystalline phase templates and diameters of 20 - 1000 nm on colloidal crystalline templates. Bartlett et al. was able to apply his arrays for sensor application in energy storage and conversion, catalysis, and electroanalysis by exploiting the changes in the material's physical properties at the nano-scale range.⁷¹

Related studies by our group previously reported gold substrates being ideal for the preparation of cavity arrays but its value as an electrode make it ideal for studying the electrical properties of molecules interacting with bilayers and it enhances the plasmonic spectroscopic signals.⁷² Jose et al. for instance, developed a lipid bilayer spanned across nanocavities through prefilling the array with buffer and allowing the lipid membrane formation on the array, and allowing an aqueous environment on both sides of the suspended lipid bilayer.⁷³ This allows the membrane to have a biomimetic environment where further research into sensor applications such as drug-cell and protein incorporation interactions is required. The plasmonic behaviour of nanocavity arrays can be used to detect the luminescence of weakly emitting analytes when filled within the cavity. This was observed by Jose et al. where the intensity of emission of $[\text{Ru}(2,2'\text{-bipyridyl})_2(2,2':4,4'';3,3''\text{-quarterpyridyl})]^{2+}$ and fullerene (C_{60}) increased in order of magnitude in 820 nm diameter nanocavities compared to that of the bulk solution using confocal fluorescence microscopy.⁷³ The enhanced signal intensity improved the sensitivity which is ideal for sensing application. Similarly, Liu et al. developed a biosensing technique where the oligonucleotides' immobilisation produced the fluorescence signal within the cavity array with 200 nm in diameter and having complementary target oligonucleotides in solution.⁵²

The enhanced fluorescence was seen in the target molecules that were bound within the cavity. While unbound target molecules, outside the cavity cannot transmit their fluorescent emission efficiently through the substrate, and thus demonstrating an effective biosensing substrate.³⁹ Research carried out by Gimenez et al. similarly demonstrated the potential for nanostructured periodic arrays for sensing applications where more than 10^4 improvement over Surface Enhanced Raman Spectroscopy (SERS) and a 200-fold improvement over Metal Enhanced Fluorescence (MEF).⁷⁴ While research carried out by Sarangi et al. demonstrates the use of MSLBs as biomimetic platforms to gain an insight into the interaction of Miltefosine on lipid membranes using electrochemical impedance spectroscopy.⁷⁵

1.7 Electrochemical assessment of Lipid membranes

Defects or impurities on a substrate's surface are found due to substrate preparation, substrate cleanliness, and solution purity. These defects, which present themselves on the monolayer, can affect the reactivity of the electrode surface. Specifically, in the case of alkanethiol on gold, defects on monolayers' surface result in missing rows of alkanethiols. Vericat et al. for instance, discussed how impurities could arise from insufficient annealing procedures, the partial extension of hydrocarbons resulting in the change of tilt angle, or potential desorption of Au from the substrate surface.⁷⁶

CV is an electrochemical technique sensitive enough to detect both nanoamp and picoamp levels of current, suitable to detect such defects.¹⁹ CVs can be used to reveal the impurity of an array or the density of a SAM through the current rate of modified and unmodified electrodes. Conversely, a decrease in current is indicative of the presence of SAM which hinders redox reactions. The surface coverage of SAMs can also be determined by electrochemistry. For instance, Weisshaar et al. used voltametric measurements to assess different monolayer films' surface coverage through reductive desorption.⁷⁷

This was done where the charge for the one-electron desorption of the Au-S bond was measured through voltammogram in an alkaline buffer. Dodecanthiol and two ferrocene-terminated thiols were the thiols used in this experiment. Weisshaar determined the surface coverage of three various monolayer films through volumetric measurements by reductive desorption. The following equation:

$$\Gamma = \frac{Q}{nFA}$$

Equation 1.2

Where Γ is the monolayer surface coverage (mol cm^{-1}), n is the number of electrons taking part in the transfer, F is Faraday's constant (C mol^{-1}), A is the electroactive surface area (cm^2) and Q is charge, measured in coulombs (C) and is in direct proportion to the surface coverage. Electrochemical impedance spectroscopy (EIS) is a non-destructive electrochemical method used to assess the interfacial electrical properties of an electrode system using Ohm's law:

$$R = \frac{V}{I}$$

Equation 1.3

Where R is the resistance, E is the potential, and I is the current. Ohm's law describes an ideal resistor in a circuit; the resistance is independent of the AC frequency and the current and voltage passing through the circuit in phase. The impedance is measured by the phase shift change in the AC potential within the electrochemical cell. An AC potential applied to the system gives a pseudo linear response.

A sinusoidal wave function is produced from the AC potential, and if it is pseudo linear, the corresponding current response will be sinusoidal at the same frequency, but phase-shifted, Φ .^{78,79,80} EIS measures the current response where the impedance Z is fixed by the applied voltage causing a perturbation of the sinusoidal wave and given in the following equation:

$$\text{System: } Z(t) = \frac{V(t)}{I(t)} = \frac{V_0 \sin(2\pi ft)}{I_0 \sin(2\pi ft + \Phi)}$$

Equation 1.4

However, in the case of a system containing a lipid bilayer, a phase separation occurs between the applied alternating current (AC) voltage and current reflecting the system's impedance.⁸¹

V_0 and I_0 represent the voltage and current signals within the system, f is the sinusoidal wave frequency, t is time, and Φ is the phase shift between current and time, and voltage and time functions. As seen in figure 1.11, the data obtained from impedance are represented on Nyquist or Bode plots. Nyquist plots typically comprise a high frequency semi-circular segment, representing the electron transfer process, while the low frequency straight angled line represents the diffusion-limited process as seen in the image.⁸²

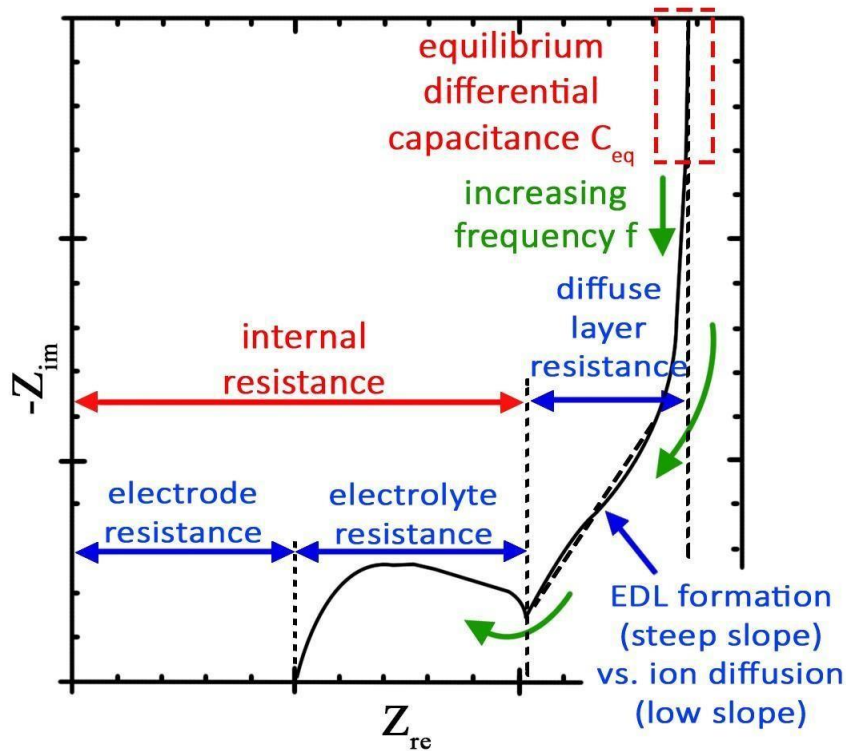


Figure 1.11: Nyquist plot illustration depicting the high-frequency semi-circular region and the straight angled region for electric double layer capacitor electrodes.⁸³

The impedance of a given circuit is represented by the vector's length from 0 to a specific point, along with the angle of the vector known as the phase shift. Quantitative results can be obtained by fitting an equivalent circuit model (ECM) through a combination of resistance and capacitance elements arranged in series or parallel. To choose the correct ECM, insight into the electrochemical system is needed to ensure correct physical and chemical components are put in place. Although the allocation of ECM components is often based on educated thought, in cases in specific models where only one parameter significantly changes useful information can be produced. As seen in figure 1.12, an ECM for a bio-faradaic process for a gold working electrode contains a double layer capacitance (C_{dl}), the ohmic resistance of the electrolyte (R_s), charge transfer resistance (R_{ct}), and Z_w is the Warburg impedance.^{78,84}

A typical ECM for a supported lipid bilayer is shown in figure 1.11 contains both a resistor and a capacitor in parallel to the bilayer (R_m , C_m) and solution resistor element (R_s), along with a double layer capacitor for the electrode and solution interface (C_{dl}).^{85,86,87,88} Steinem et al. used impedance spectroscopy to analyse the supported lipid bilayers.

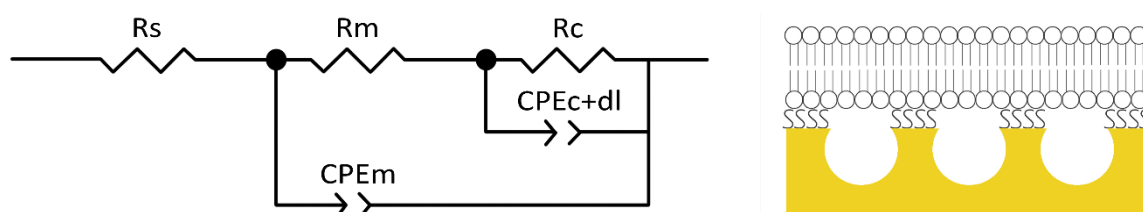


Figure 1.12: An ECM used in fitting of lipid bilayer impedance data.

MSLBs, or microcavity assisted lipid bilayers, have been used by our group to investigate protein-membrane interactions and aggregation at the membrane interface through gold microcavity arrays using polystyrene sphere lithography. Berselli et al. assessed the effect of transmembrane lipid asymmetry on lipid diffusion, membrane viscosity and cholera toxin ganglioside across six symmetric and asymmetric membranes.⁸⁸ Fluorescence lifetime correlation spectroscopy was used to determine the lateral mobility of the lipid membrane and protein while EIS was used to detect protein-membrane assembly at the nanometer scale. It was found that transmembrane leaflet asymmetry had a profound impact on the membrane resistance, as the resistance of ternary symmetric bilayers was found to be 2.6 times higher than the asymmetric membranes with an analogous composition in the distal leaflet composed of only DOPC.⁸⁸

1.8 Conclusions

Chapter 1 describes the current lipid membrane model systems. These model membranes have been applied to research questions from lipid dynamics to drug membrane interactions. Cell membrane models have advanced significantly and offer useful approaches to understanding the behaviour of real membranes separate to the complex cell environment. The dynamics and complexity of these membranes have sparked a lot of interest in lipid membrane science, which can cover a wide variety of topics, including protein-drug interactions, drug permeation, and aggregation for biomimetic applications. While considerable progress has been made in supported lipid bilayers, improvements in reproducibility and stability are still needed. This thesis aims to use microcavity arrays in which membrane stability is assessed using three different SAMs. This will be achieved by spanning support lipid bilayers across microcavity array substrates. Using two different variations of gold microcavity arrays, an electrochemically deposited microcavity array, and two-photon polymerisation fabricated substrates, this study addresses the surface chemistry involved in the stabilisation of cell membrane models.

1.9 References

- (1) Kumar, K.; Isa, L.; Enger, A.; Schmidt, R.; Textor, M.; Reimhult, E. Formation of Nanopore-Spanning Lipid Bilayers through Liposome Fusion. *Langmuir* **2011**, *27* (17), 10920–10928. <https://doi.org/10.1021/la2019132>.
- (2) Wang, Y.-S.; Yau, S.; Chau, L.-K.; Mohamed, A.; Huang, C.-J. Functional Biointerfaces Based on Mixed Zwitterionic Self-Assembled Monolayers for Biosensing Applications. *Langmuir* **2019**, *35* (5), 1652–1661. <https://doi.org/10.1021/acs.langmuir.8b01779>.
- (3) Porter, M. D.; Bright, T. B.; Allara, D. L.; Chidsey, C. E. D. Spontaneously Organized Molecular Assemblies. 4. Structural Characterization of n-Alkyl Thiol Monolayers on Gold by Optical Ellipsometry, Infrared Spectroscopy, and Electrochemistry. *J. Am. Chem. Soc.* **1987**, *109* (12), 3559–3568. <https://doi.org/10.1021/ja00246a011>.
- (4) Kwak, S. K.; Lee, G. S.; Ahn, D. J.; Choi, J. W. Pattern Formation of Cytochrome c by Microcontact Printing and Dip-Pen Nanolithography. *Materials Science and Engineering: C* **2004**, *24* (1), 151–155. <https://doi.org/10.1016/j.msec.2003.09.015>.
- (5) Barbosa, M. A.; Martins, M. C. L.; Barbosa, J. N. 4 - Cellular Response to the Surface Chemistry of Nanostructured Biomaterials. In *Cellular Response to Biomaterials*; Di Silvio, L., Ed.; Woodhead Publishing Series in Biomaterials; Woodhead Publishing, **2009**; pp 85–113. <https://doi.org/10.1533/9781845695477.1.85>.
- (6) Ulman, A. Formation and Structure of Self-Assembled Monolayers. *Chem. Rev.* **1996**, *96* (4), 1533–1554. <https://doi.org/10.1021/cr9502357>.

- (7) Vericat, C.; Vela, M. E.; Salvarezza, R. C. Self-Assembled Monolayers of Alkanethiols on Au(111): Surface Structures, Defects and Dynamics. *Phys. Chem. Chem. Phys.* **2005**, *7* (18), 3258–3268. <https://doi.org/10.1039/B505903H>.
- (8) Boccafoschi, F.; Fusaro, L.; Cannas, M. 15 - Immobilization of Peptides on Cardiovascular Stent. In *Functionalised Cardiovascular Stents*; Wall, J. G., Podbielska, H., Wawrzyńska, M., Eds.; Woodhead Publishing, **2018**; pp 305–318. <https://doi.org/10.1016/B978-0-08-100496-8.00016-0>.
- (9) Yalcintas, E. P.; Ozutemiz, K. B.; Cetinkaya, T.; Dalloro, L.; Majidi, C.; Ozdoganlar, B. O. Soft Electronics Manufacturing Using Microcontact Printing. *Adv. Funct. Mater.* **2019** *29* (51). <https://doi.org/10.1002/adfm.201906551>.
- (10) Love, J. C.; Wolfe, D. B.; Chabinyc, M. L.; Paul, K. E.; Whitesides, G. M. Self-Assembled Monolayers of Alkanethiolates on Palladium Are Good Etch Resists. *J. Am. Chem. Soc.* **2002**, *124* (8), 1576–1577. <https://doi.org/10.1021/ja012569l>.
- (11) Schreiber, F. Structure and Growth of Self-Assembling Monolayers. *Progress in Surface Science* **2000**, *65* (5–8), 151–257. [https://doi.org/10.1016/S0079-6816\(00\)00024-1](https://doi.org/10.1016/S0079-6816(00)00024-1).
- (12) Harvey, E.; Ghantasala, M. 12 - Nanofabrication. In *Nanostructure Control of Materials*; Hannink, R. H. J., Hill, A. J., Eds.; Woodhead Publishing, 2006; pp 303–330. <https://doi.org/10.1533/9781845691189.303>.
- (13) Wu, H.; Wu, L.; Zhou, X.; Liu, B.; Zheng, B. Patterning Hydrophobic Surfaces by Negative Microcontact Printing and Its Applications. *Small* **2018**, *14* (38), e1802128. <https://doi.org/10.1002/sml.201802128>.

- (14) Yadav, H. O. S.; Kuo, A.-T.; Urata, S.; Shinoda, W. Effects of Packing Density and Chain Length on the Surface Hydrophobicity of Thin Films Composed of Perfluoroalkyl Acrylate Chains: A Molecular Dynamics Study. *Langmuir* **2019**, *35* (44), 14316–14323. <https://doi.org/10.1021/acs.langmuir.9b02656>.
- (15) Delamarche, E.; Schmid, H.; Bietsch, A.; Larsen, N. B.; Rothuizen, H.; Michel, B.; Biebuyck, H. Transport Mechanisms of Alkanethiols during Microcontact Printing on Gold. *J. Phys. Chem. B* **1998**, *102* (18), 3324–3334. <https://doi.org/10.1021/jp980556x>.
- (16) Schreiber, F. Structure and Growth of Self-Assembling Monolayers. *Progress in Surface Science* **2000**, *65* (5), 151–257. [https://doi.org/10.1016/S0079-6816\(00\)00024-1](https://doi.org/10.1016/S0079-6816(00)00024-1).
- (17) Whitesides, G. M.; Grzybowski, B. Self-Assembly at All Scales. *Science* **2002**, *295* (5564), 2418–2421. <https://doi.org/10.1126/science.1070821>.
- (18) Nelson, A.; Auffret, N.; Borlakoglu, J. Interaction of Hydrophobic Organic Compounds with Mercury Adsorbed Dioleoylphosphatidylcholine Monolayers. *Biochimica et Biophysica Acta (BBA) - Biomembranes* **1990**, *1021* (2), 205–216. [https://doi.org/10.1016/0005-2736\(90\)90035-M](https://doi.org/10.1016/0005-2736(90)90035-M).
- (19) Forster, R.; Johannes, G. V.; Keyes, T. E. Interfacial Supramolecular Assemblies. *J. Am. Chem. Soc.* **2003**, *125* (44), 13620. <https://doi.org/10.1021/ja033539g>.
- (20) Tamada, Y.; Ikada, Y. Fibroblast Growth on Polymer Surfaces and Biosynthesis of Collagen. *J. Biomed. Mater. Res.* **1994**, *28* (7), 783–789. <https://doi.org/10.1002/jbm.820280705>.
- (21) Jadhav, S. A. Functional Self-Assembled Monolayers (SAMs) of Organic Compounds on Gold Nanoparticles. *J. Mater. Chem.* **2012**, *22* (13), 5894–5899. <https://doi.org/10.1039/C2JM14239B>.

- (22) Carignano, P.; Ma, C.; Rj, N.; I, S. Hydrophobic-Induced Surface Reorganization: Molecular Dynamics Simulations of Water Nanodroplet on Perfluorocarbon Self-Assembled Monolayers. *Soft Matter* **2010**, *6* (8), 1644–1654. <https://doi.org/10.1039/b923392j>.
- (23) Lee, J. H.; Jung, H. W.; Kang, I. K.; Lee, H. B. Cell Behaviour on Polymer Surfaces with Different Functional Groups. *Biomaterials* **1994**, *15* (9), 705–711. [https://doi.org/10.1016/0142-9612\(94\)90169-4](https://doi.org/10.1016/0142-9612(94)90169-4).
- (24) Chimisso, V.; Maffei, V.; Hürlimann, D.; Palivan, C. G.; Meier, W. Self-Assembled Polymeric Membranes and Nanoassemblies on Surfaces: Preparation, Characterization, and Current Applications. *Macromol. Biosci.* **2020**, *20* (1), 1900257. <https://doi.org/10.1002/mabi.201900257>.
- (25) Wenzl, I.; Yam, C. M.; Barriet, D.; Lee, T. R. Structure and Wettability of Methoxy-Terminated Self-Assembled Monolayers on Gold. *Langmuir* **2003**, *19* (24), 10217–10224. <https://doi.org/10.1021/la035227x>.
- (26) Chidsey, C. E. D.; Murray, R. W. Electroactive Polymers and Macromolecular Electronics. *Science* **1986**, *231* (4733), 25–31. <https://doi.org/10.1126/science.231.4733.25>.
- (27) Zhang, H.; Yasutake, Y.; Shichibu, Y.; Teranishi, T.; Majima, Y. Tunneling Resistance of Double-Barrier Tunneling Structures with an Alkanethiol-Protected Au Nanoparticle. *Phys. Rev. B* **2005**, *72* (20), 205441. <https://doi.org/10.1103/PhysRevB.72.205441>.
- (28) Cooper, G. M. *Structure of the Plasma Membrane*; Sinauer Associates, 2000.
- (29) Calvin, M. Chemical Evolution and the Origin of Life. *Chemical Evolution and the Origin of Life* **1955**, 24.

- (30) Spampinato, V.; Parracino, M. A.; La Spina, R.; Rossi, F.; Ceccone, G. Surface Analysis of Gold Nanoparticles Functionalized with Thiol-Modified Glucose SAMs for Biosensor Applications. *Front Chem.* **2016**, *4*, 8. <https://doi.org/10.3389/fchem.2016.00008>.
- (31) Salomon, A.; Cahen, D.; Lindsay, S.; Tomfohr, J.; Engelkes, V. B.; Frisbie, C. D. Comparison of Electronic Transport Measurements on Organic Molecules. *Adv. Mater.* **2003**, *15* (22), 1881–1890. <https://doi.org/10.1002/adma.200306091>.
- (32) Yousaf, M. N.; Chan, E. W. L.; Mrksich, M. The Kinetic Order of an Interfacial Diels-Alder Reaction Depends on the Environment of the Immobilized Dienophile. *Angew Chem. Int. Ed. Engl.* **2000**, *39* (11), 1943–1946. [https://doi.org/10.1002/1521-3773\(20000602\)39](https://doi.org/10.1002/1521-3773(20000602)39).
- (33) Mader, S.; Windelspecht, M. *Biology*; 2018.
- (34) Jackman, J. A.; Knoll, W.; Cho, N.-J. Biotechnology Applications of Tethered Lipid Bilayer Membranes. *Materials(Basel)* **2012**, *5* (12), 2637–2657. <https://doi.org/10.3390/ma5122637>.
- (35) Rivel, T.; Ramseyer, C.; Yesylevskyy, S. The Asymmetry of Plasma Membranes and Their Cholesterol Content Influence the Uptake of Cisplatin. *Scientific Reports* **2019**, *9* (1), 5627. <https://doi.org/10.1038/s41598-019-41903-w>.
- (36) Alberts, B.; Johnson, A.; Lewis, J.; Raff, M.; Roberts, K.; Walter, P. The Lipid Bilayer. *Molecular Biology of the Cell. 4th edition* **2002**.
- (37) Fujimoto, T.; Parmryd, I. Interleaflet Coupling, Pinning, and Leaflet Asymmetry—Major Players in Plasma Membrane Nanodomain Formation. *Front. Cell Dev. Biol.* **2017**, *4*. <https://doi.org/10.3389/fcell.2016.00155>.

- (38) St. Clair, J. R.; Wang, Q.; Li, G.; London, E. Preparation and Physical Properties of Asymmetric Model Membrane Vesicles. In *The Biophysics of Cell Membranes: Biological Consequences*; Epand, R. M., Ruyschaert, J.-M., Eds.; Springer Series in Biophysics; Springer: Singapore, 2017; pp 1–27. https://doi.org/10.1007/978-981-10-6244-5_1.
- (39) Ramadurai, S.; Kohut, A.; Sarangi, N. K.; Zholobko, O.; Baulin, V. A.; Voronov, A.; Keyes, T. E. Macromolecular Inversion-Driven Polymer Insertion into Model Lipid Bilayer Membranes. *J. Colloid Interface Sci.* **2019**, *542*, 483–494. <https://doi.org/10.1016/j.jcis.2019.01.093>.
- (40) Cooper, G. M. Structure of the Plasma Membrane. *The Cell: A Molecular Approach. 2nd edition* **2000**.
- (41) Sharma, A.; Sharma, U. S. Liposomes in Drug Delivery: Progress and Limitations. *Int. J Pharm.* **1997**, *154* (2), 123–140. [https://doi.org/10.1016/S0378-5173\(97\)00135-X](https://doi.org/10.1016/S0378-5173(97)00135-X).
- (42) Maher, S.; Basit, H.; Forster, R. J.; Keyes, T. E. Micron Dimensioned Cavity Array Supported Lipid Bilayers for the Electrochemical Investigation of Ionophore Activity. *Bioelectrochemistry* **2016**, *112*, 16–23. <https://doi.org/10.1016/j.bioelechem.2016.07.002>.
- (43) Knobloch, J.; Suhendro, D. K.; Zieleniecki, J. L.; Shapter, J. G.; Köper, I. Membrane–Drug Interactions Studied Using Model Membrane Systems. *Saudi J. Biol. Sci.* **2015**, *22* (6), 714–718. <https://doi.org/10.1016/j.sjbs.2015.03.007>.
- (44) Tamm, L. K.; McConnell, H. M. Supported Phospholipid Bilayers. *Biophys J* **1985**, *47* (1), 105–113. [https://doi.org/10.1016/S0006-3495\(85\)83882-0](https://doi.org/10.1016/S0006-3495(85)83882-0).
- (45) Mueller et al. - 1962 - Reconstitution of Excitable Cell Membrane Structur.Pdf.

- (46) Plant, A. L. Supported Hybrid Bilayer Membranes as Rugged Cell Membrane Mimics. *Langmuir* **1999**, *15* (15), 5128–5135. <https://doi.org/10.1021/la981662t>.
- (47) Xiaoyang, Z.; Deng, Y.; Wang, Y.; Barriet, D.; Guo, A. Air-Stable Supported Lipid Bilayer Membranes. WO2008118688A2, October 2, 2008.
- (48) Bangham, A. D. Surrogate Cells or Trojan Horses. The Discovery of Liposomes. *BioEssays* **1995**, *17* (12), 1081–1088. <https://doi.org/10.1002/bies.950171213>.
- (49) Akbarzadeh, A.; Rezaei-Sadabady, R.; Davaran, S.; Joo, S. W.; Zarghami, N.; Hanifehpour, Y.; Samiei, M.; Kouhi, M.; Nejati-Koshki, K. Liposome: Classification, Preparation, and Applications. *Nanoscale Res. Lett.* **2013**, *8* (1), 102. <https://doi.org/10.1186/1556-276X-8-102>.
- (50) Deb, P. K.; Al-Attraqchi, O.; Chandrasekaran, B.; Paradkar, A.; Tekade, R. K. Protein/Peptide Drug Delivery Systems: Practical Considerations in Pharmaceutical Product Development. In *Basic Fundamentals of Drug Delivery*; Tekade, R. K., Ed.; Advances in Pharmaceutical Product Development and Research; Academic Press, 2019; pp 651–684. <https://doi.org/10.1016/B978-0-12-817909-3.00016-9>.
- (51) Sharma, A.; Sharma, U. S. Liposomes in Drug Delivery: Progress and Limitations. *Int. J. Pharm.* **1997**, *154* (2), 123–140. [https://doi.org/10.1016/S0378-5173\(97\)00135-X](https://doi.org/10.1016/S0378-5173(97)00135-X).
- (52) Liu, Y.; Kim, Y. J.; Siriwon, N.; Rohrs, J. A.; Yu, Z.; Wang, P. Combination Drug Delivery via Multilamellar Vesicles Enables Targeting of Tumor Cells and Tumor Vasculature. *Biotechnol. Bioeng.* **2018**, *115* (6), 1403–1415. <https://doi.org/10.1002/bit.26566>.
- (53) Walde, P.; Cosentino, K.; Engel, H.; Stano, P. Giant Vesicles: Preparations and Applications. *ChemBiochem.* **2010**, *11* (7), 848–865. <https://doi.org/10.1002/cbic.201000010>.

- (54) Colbasevici, A.; Voskoboinikova, N.; Orekhov, P. S.; Bozdaganyan, M. E.; Karlova, M. G.; Sokolova, O. S.; Klare, J. P.; Mulkidjanian, A. Y.; Shaitan, K. V.; Steinhoff, H.-J. Lipid Dynamics in Nanoparticles Formed by Maleic Acid-Containing Copolymers: EPR Spectroscopy and Molecular Dynamics Simulations. *Biochim Biophys Acta Biomembr* **2020**, *1862* (5), 183207. <https://doi.org/10.1016/j.bbamem.2020.183207>.
- (55) Chernomordik, L. V.; Kozlov, M. M. Mechanics of Membrane Fusion. *Nat. Struct. Mol. Biol.* **2008**, *15* (7), 675–683. <https://doi.org/10.1038/nsmb.1455>.
- (56) Dietrich, C.; Bagatolli, L. A.; Volovyk, Z. N.; Thompson, N. L.; Levi, M.; Jacobson, K.; Gratton, E. Lipid Rafts Reconstituted in Model Membranes. *Biophys. J.* **2001**, *80* (3), 1417–1428.
- (57) Czogalla, A.; Grzybek, M.; Jones, W.; Coskun, U. Validity and Applicability of Membrane Model Systems for Studying Interactions of Peripheral Membrane Proteins with Lipids. *Biochim. Biophys. Acta* **2014**, *1841* (8), 1049–1059. <https://doi.org/10.1016/j.bbalip.2013.12.012>.
- (58) Bhuvana, M.; Narayanan, J. S.; Dharuman, V.; Teng, W.; Hahn, J. H.; Jayakumar, K. Gold Surface Supported Spherical Liposome-Gold Nano-Particle Nano-Composite for Label Free DNA Sensing. *Biosens. Bioelectron.* **2012**, *15* (41), 802–808. <https://doi.org/10.1016/j.bios.2012.10.017>.
- (59) Castellana, E. T.; Cremer, P. S. Solid Supported Lipid Bilayers: From Biophysical Studies to Sensor Design. *Surf. Sci. Rep.* **2016**, *61* (10), 429–444.

- (60) Elender, G.; Kühner, M.; Sackmann, E. Functionalisation of Si/SiO₂ and Glass Surfaces with Ultrathin Dextran Films and Deposition of Lipid Bilayers. *Biosens. Bioelectron.* **1996**, *11* (6–7), 565–577. [https://doi.org/10.1016/0956-5663\(96\)83292-1](https://doi.org/10.1016/0956-5663(96)83292-1).
- (61) Zhang, L.; Granick, S. Lipid Diffusion Compared in Outer and Inner Leaflets of Planar Supported Bilayers. *J. Chem. Phys.* **2005**, *123* (21), 211104. <https://doi.org/10.1063/1.2138699>.
- (62) Cooper, M. A. Optical Biosensors in Drug Discovery. *Nat. Rev. Drug Discov.* **2002**, *1* (7), 515–528. <https://doi.org/10.1038/nrd838>.
- (63) Lang, H.; Duschl, C.; Vogel, H. A New Class of Thiolipids for the Attachment of Lipid Bilayers on Gold Surfaces. *Langmuir* **1994**, *10* (1), 197–210. <https://doi.org/10.1021/la00013a029>.
- (64) Steltenkamp, S.; Müller, M. M.; Deserno, M.; Hennesthal, C.; Steinem, C.; Janshoff, A. Mechanical Properties of Pore-Spanning Lipid Bilayers Probed by Atomic Force Microscopy. *Biophys. J.* **2006**, *91* (1), 217–226. <https://doi.org/10.1529/biophysj.106.081398>.
- (65) Han, X.; Studer, A.; Sehr, H.; Geissbühler, I.; Di Berardino, M.; Winkler, F. K.; Tiefenauer, L. X. Nanopore Arrays for Stable and Functional Free-Standing Lipid Bilayers. *Adv. Mater.* **2007**, *19* (24), 4466–4470. <https://doi.org/10.1002/adma.200700468>.
- (66) Oo, S. Z.; Silva, G.; Carpignano, F.; Noual, A.; Pechstedt, K.; Mateos, L.; Grant-Jacob, J. A.; Brocklesby, B.; Horak, P.; Charlton, M.; Boden, S. A.; Melvin, T. A Nanoporous Gold Membrane for Sensing Applications. *Sensing and Bio-Sensing Research* **2016**, *7*, 133–140. <https://doi.org/10.1016/j.sbsr.2016.01.001>.

- (67) Šakalys, R.; Kho, K. W.; Keyes, T. E. A Reproducible, Low Cost Microfluidic Microcavity Array SERS Platform Prepared by Soft Lithography from a 2 Photon 3D Printed Template. *Sensors and Actuators B: Chemical* **2021**, *340*, 129970. <https://doi.org/10.1016/j.snb.2021.129970>.
- (68) Kessler, T.; Hagemann, C.; Grebing, C.; Legero, T.; Sterr, U.; Riehle, F.; Martin, M. J.; Chen, L.; Ye, J. A Sub-40-MHz-Linewidth Laser Based on a Silicon Single-Crystal Optical Cavity. *Nat. Photonics* **2012**, *6* (10), 687–692. <https://doi.org/10.1038/nphoton.2012.217>.
- (69) Murphy, A.; Sonnefraud, Y.; Krasavin, A. V.; Ginzburg, P.; Morgan, F.; McPhillips, J.; Wurtz, G.; Maier, S. A.; Zayats, A. V.; Pollard, R. Fabrication and Optical Properties of Large-Scale Arrays of Gold Nanocavities Based on Rod-in-a-Tube Coaxials. *Appl. Phys. Lett.* **2013**, *102* (10), 103103. <https://doi.org/10.1063/1.4794935>.
- (70) Bartlett, P. N.; Baumberg, J. J.; Coyle, S.; Abdelsalam, M. E. Optical Properties of Nanostructured Metal Films. *Faraday Discuss.* **2004**, *125* (0), 117–132. <https://doi.org/10.1039/B304116F>.
- (71) Jose, B.; Mallon, C. T.; Forster, R. J.; Blackledge, C.; Keyes, T. E. Lipid Bilayer Assembly at a Gold Nanocavity Array. *Chem. Comm.* **2011**, *47* (46), 12530. <https://doi.org/10.1039/c1cc15709d>.
- (72) Jose, B.; Steffen, R.; Neugebauer, U.; Sheridan, E.; Marthi, R.; Forster, R. J.; Keyes, T. E. Emission Enhancement within Gold Spherical Nanocavity Arrays. *Phys. Chem. Chem. Phys.* **2009**, *11* (46), 10923–10933. <https://doi.org/10.1039/B908385E>.

- (73) Gimenez, A. V.; Kho, K. W.; Keyes, T. E. Nano-Substructured Plasmonic Pore Arrays: A Robust, Low Cost Route to Reproducible Hierarchical Structures Extended across Macroscopic Dimensions. *Nanoscale Adv.* **2020**, *2* (10), 4740–4756. <https://doi.org/10.1039/D0NA00527D>.
- (74) Sarangi, N. K.; Prabhakaran, A.; Keyes, T. E. Interaction of Miltefosine with Microcavity Supported Lipid Membrane: Biophysical Insights from Electrochemical Impedance Spectroscopy. *Electroanalysis* **2020**, *32* (12), 2936–2945. <https://doi.org/10.1002/elan.202060424>.
- (75) Vericat, C.; Vela, M. E.; Benitez, G.; Carro, P.; Salvarezza, R. C. Self-Assembled Monolayers of Thiols and Dithiols on Gold: New Challenges for a Well-Known System. *Chem. Soc. Rev.* **2010**, *39* (5), 1805–1834. <https://doi.org/10.1039/B907301A>.
- (76) Weisshaar, D. E.; Walczak, M. M.; Porter, M. D. Electrochemically Induced Transformations of Monolayers Formed by Self-Assembly of Mercaptoethanol at Gold. *Langmuir* **2002**, *9* (1), 323–329. <https://doi.org/10.1021/la00025a061>.
- (77) Yang, L.; Bashir, R. Electrical/Electrochemical Impedance for Rapid Detection of Foodborne Pathogenic Bacteria. *Biotechnol. Adv.* **2008**, *26* (2), 135–150. <https://doi.org/10.1016/j.biotechadv.2007.10.003>.
- (78) Zhu, C.; Dong, S. Energetic Graphene-Based Electrochemical Analytical Devices in Nucleic Acid, Protein and Cancer Diagnostics and Detection. *Electroanalysis* **2014**, *26* (1), 14–29. <https://doi.org/10.1002/elan.201300056>.

- (79) Niu, J.; Lee, J. Y. A New Approach for the Determination of Fish Freshness by Electrochemical Impedance Spectroscopy. *J. Food Sci.* **2000**, *65* (5), 780–785. <https://doi.org/10.1111/j.1365-2621.2000.tb13586.x>.
- (80) Janshoff, A.; Steinem, C. Transport across Artificial Membranes—an Analytical Perspective. *Anal. Bioanal. Chem.* **2006**, *385* (3), 433–451. <https://doi.org/10.1007/s00216-006-0305-9>.
- (81) Zhu, C.; Guo, S.; Fang, Y.; Dong, S. Reducing Sugar: New Functional Molecules for the Green Synthesis of Graphene Nanosheets. *ACS Nano* **2010**, *4* (4), 2429–2437. <https://doi.org/10.1021/nn1002387>.
- (82) Mei, B.-A.; Munteshari, O.; Lau, J.; Dunn, B.; Pilon, L. Physical Interpretations of Nyquist Plots for EDLC Electrodes and Devices. *J. Phys. Chem C* **2018**, *122* (1), 194–206. <https://doi.org/10.1021/acs.jpcc.7b10582>.
- (83) Jiang, J.; Y, X.; D, W.; M, C.; F, Z. GUITAR-Enhanced Facile Discrimination of Aged Chinese Baijiu Using Electrochemical Impedance Spectroscopy. *Anal. Chim. Acta.* **2019**, *1059*, 36–41. <https://doi.org/10.1016/j.aca.2019.01.050>.
- (84) Basit, H.; Van der Heyden, A.; Gondran, C.; Nysten, B.; Dumy, P.; Labbé, P. Tethered Bilayer Lipid Membranes on Mixed Self-Assembled Monolayers of a Novel Anchoring Thiol: Impact of the Anchoring Thiol Density on Bilayer Formation. *Langmuir* **2011**, *27* (23), 14317–14328. <https://doi.org/10.1021/la202847r>.
- (85) Schmitt, E. K.; Nurnabi, M.; Bushby, R. J.; Steinem, C. Electrically Insulating Pore-Suspending Membranes on Highly Ordered Porous Alumina Obtained from Vesicle Spreading. *Soft. Matter.* **2008**, *4* (2), 250–253. <https://doi.org/10.1039/B716723G>.

- (86) Wiegand, G.; Arribas-Layton, N.; Hillebrandt, H.; Sackmann, E.; Wagner, P. Electrical Properties of Supported Lipid Bilayer Membranes. *J. Phys. Chem. B* **2002**, *106* (16), 4245–4254. <https://doi.org/10.1021/jp014337e>.
- (87) Steinem, C.; Janshoff, A.; Ulrich, W. P.; Sieber, M.; Galla, H. J. Impedance Analysis of Supported Lipid Bilayer Membranes: A Scrutiny of Different Preparation Techniques. *Biochim. Biophys. Acta* **1996**, *1279* (2), 169–180. [https://doi.org/10.1016/0005-2736\(95\)00274-x](https://doi.org/10.1016/0005-2736(95)00274-x).
- (88) Berselli, G. B.; Sarangi, N. K.; Ramadurai, S.; Murphy, P. V.; Keyes, T. E. Microcavity-Supported Lipid Membranes: Versatile Platforms for Building Asymmetric Lipid Bilayers and for Protein Recognition *Appl. Bio Mater.* **2019**, *2* (8), 3404–3417. <https://doi.org/10.1021/acsabm.9b00378>.

**Chapter 2: The impact SAM on Bilayer
formation and stability at lithographically
prepared microcavity arrays**

2.0 Introduction

Phospholipid bilayers spanned across a solid substrate can provide useful information for studying the behaviours and interactions of biological membranes.¹ The support of a membrane to a surface allows it to be studied by a variety of techniques available in surface science, allowing for the basis of new sensor technologies in diverse fields such as drug delivery studies and disease diagnostics.² Several methods have been used to deposit lipid membranes onto either uncoated, pre-modified surfaces and self-assembled tethered methods such as Langmuir-Blodgett and vesicle fusion methods.^{3,4} Lipid membranes model membrane interactions, including microcavity supported lipid bilayers (MSLBs) allowing an insight into passive membrane permeability along with membrane toxicological problems.⁵ A variety of approaches to develop porous substrates have been reported including photolithographic methods and high cost electron beam.^{6,7,8,9,10} Herein, the effect of functional terminals on the different self-assembled monolayer (SAM) of bilayer formation and stability, on electrochemically deposited microcavity array platform as the working electrode was assessed. SAMs have shown appeal in sensors, interfaces, microfabrication, and lipid membrane models.^{11,12}

Over the last 30 years, there has been significant development in the lipid membrane model and it is of keen interest.¹³ The SAMs used to support lipid bilayers and their overall stability on the platform were 6-mercapto-1-hexanol, hydroxyl terminated polyethene glycol (PEG) thiol and 6-mercaptohexanoic acid. The thiols groups at the end of these SAMs allow for straight-chained alkane groups to bind onto the Au surface. EIS measurements and Raman spectroscopy techniques were employed for characterisation purpose.

2.1 Instrumentation

2.1.1 Scanning Electron Microscopy

Scanning electron microscopy (SEM) is a versatile instrument that allows for the examination of structures and chemical composition characterisation across many fields. As per figure 2.1, an SEM instrument contains an electron gun which accelerates electrons at a range between 0.1-30 keV between a cathode and an anode. Electromagnetic lenses and apertures focus the beam of electrons onto the specimen was mounted onto the stage and analysed under vacuum. Electrons traverse through lenses which are focused coarsely initially and then finely to obtain a well-defined image in the nanometer size range. Images can be formed either from secondary or backscattered electrons which can provide information relating to a substrates topography, morphology and composition.¹⁴ Although SEM is a technique which is both easy to operate and requires limited sample preparation, electrically insulating sample do require gold sputter coating to make the sample more conductive.

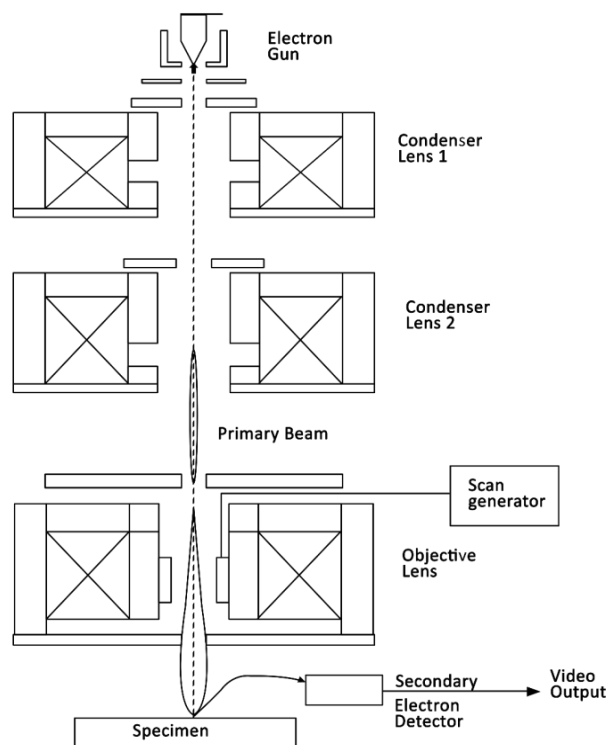


Figure 2.1: Schematic diagram of an scanning electron microscope setup.¹⁴

2.1.2 Cyclic Voltammetry

Cyclic voltammetry (CV) has been widely used to explain chemical reactions and to assess diffusion coefficients for solution species. The characterisation of modified electrodes is also made possible through the use of this technique. Thus, this technique gives a large amount of information over a potential range over a short time span. CV can be used to assess charge transport rates for modified electrodes, through the analysis of the current response.¹⁵ Where a semi-infinite diffusion regime is kept, the peak current of a CV for a modified electrode is given by the Randles-Sevcik equation:

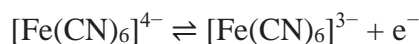
$$I_p = 0.446nFAC\left(\frac{nFvD}{RT}\right)^{1/2}$$

Equation 2.1

Where I_p is the peak current, n the number of electrons passed, F the Faraday constant, A the area of the electrode in cm^2 , D_{CT} and C are the charge transport diffusion coefficients and concentration of the electroactive species within the film and v is the scan rate V/s .¹⁵

As the potential is scanned positively, $\text{Fe}(\text{CN})_6^{4-}$ becomes oxidised with the anodic current.

As the potential is scanned negatively for the reverse scan, the electrode surface becomes a reductant, $\text{Fe}(\text{CN})_6^{3-}$ will be reduced by the electrode process, resulting in a cathodic current:



Equation 2.3

A redox reaction is were half of the reaction rapidly exchanges electrons at the surface of the working electrode are said to be electrochemically reversible couples. The reduction potential E_o' for a reversible couple is the mean of E_{pa} and E_{pc} .

$$E_o' = 0.5(E_{pa} + E_{pc})$$

Equation 2.4

The number of electrons involved in a redox reaction for reversible couple is related to the difference of peak potentials by:

$$E_{pa} - E_{pc} = \frac{57.0(mV)}{n}$$

Equation 2.5

2.1.3 Electrochemical Impedance Spectroscopy

Resistance is the measure of an electrical circuit's ability to resist the flow of electrical current and it is defined by Ohm's law, where v is potential and I is current:

$$R = \frac{V}{I}$$

Equation 2.2

Ohm's law describes an ideal resistor. An ideal resistor shows that the resistance is independent of applied current frequency such that an alternating current (AC) and voltage signals passed through a resistor are in phase. However, for lipid bilayers on working electrodes, the phase separation exists between the applied AC voltage and the corresponding current reflects the impedance of the system.¹⁶ Impedance is measured by applying an AC potential to an electrochemical cell and studying the AC response.

In EIS, a small AC potential is applied to the cell to give a pseudo-linear response. As the AC potential signal is a sinusoidal function, if the potential is pseudo-linear, the current response will have a shifted phase but will have a sinusoidal function at the same frequency.¹⁷ The fitting of impedance data to an equivalence circuit model (ECM) can provide quantitative information on the resistance and capacitance of both bilayers.¹⁸ It is of key importance to understand the physical elements and dielectrical properties within the equivalence circuit model system to ensure that the correct fitting model is used for the impedance spectra for the supported lipid bilayers. Information on the resistance and capacitance of bilayers can be obtained through the fitting of impedance data to an ECM. This enables the extraction of electrical and dielectrical properties of the system. It is important to select the correct ECM depending on the system being studied.^{19,20,21,22} EIS has been used considerably to assess the electrical properties of supported lipid bilayers. For instance, impedance has been used by Steinem et al. to examine the different ways to assess the properties and formation of supported lipid bilayers.¹⁹

2.1.4 Langmuir-Blodgett

The Langmuir-Blodgett method is a method that utilises amphiphilic surfactants ability to self-assemble at an air/water interface as seen in figure 2.2. This method is commonly used due to its precise control of the monolayer thickness, which allows for the homogenous deposition formation of multi composition structures. Amphiphilic substrates are commonly applied to Langmuir-Blodgett methods through the ability of the polar areas to remain in the water interface and the non-polar area to orientate to the liquid phase.²³ Through applying pressure, a close packed homogenous monolayer will form through the compression of these substrates to form a Langmuir film. The formation of the monolayer is affected by the chain length with long chains will crystallise on the air/water interface while too short of a chain may form a micelle.²³

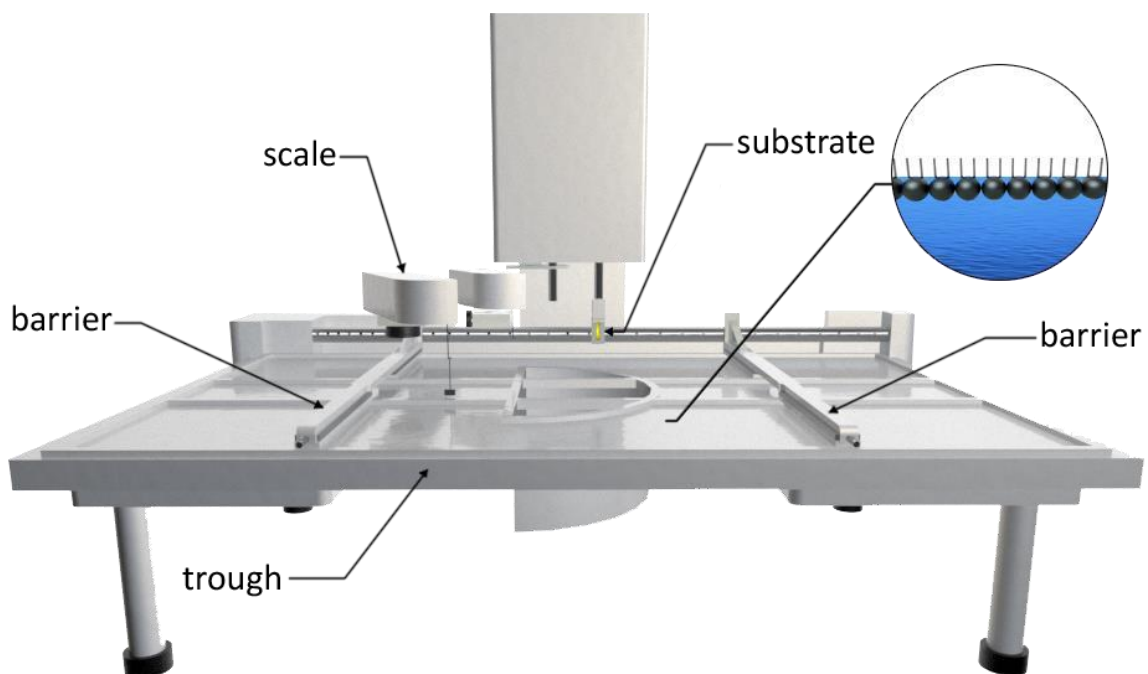


Figure 2.2: Schematic diagram of a Langmuir-Blodgett trough which demonstrates the barriers being compressed allowing the monolayers to orientate.

The film is first organised through compressions from a two dimensional gas phase moving to liquid and then finally the solid phase by a surface pressure-area isotherm as seen in figure 2.3. In the gaseous phase, the molecules are largely separated from one another. As the barriers close, the surface area decreases and surface pressure rises as the molecules become better packed.

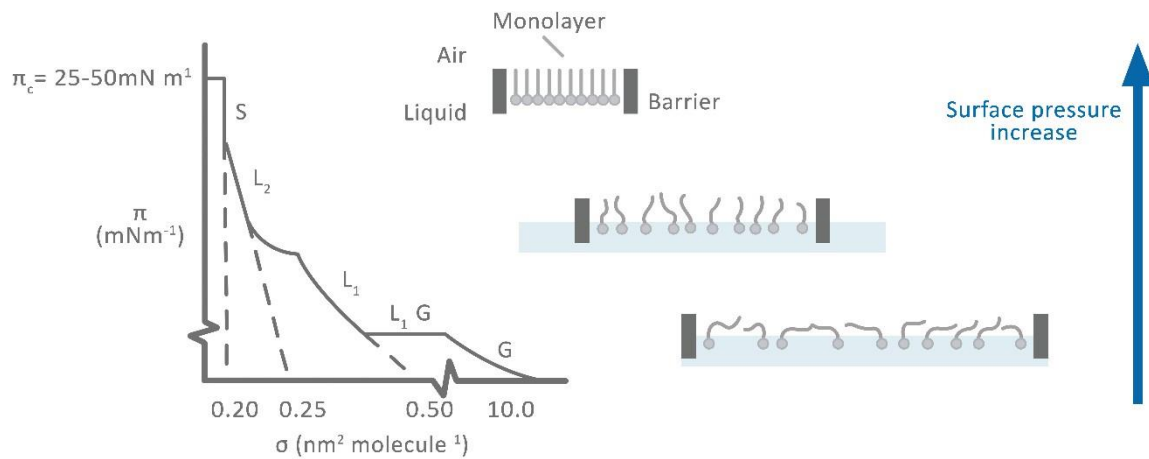


Figure 2.3: Schematic representation of a pressure-area isotherm.²⁴

A typical Langmuir-Blodgett trough is made from Teflon or Delrin, which is a hydrophilic material which prevents monolayers from going beneath the barrier. The surface pressure (Π) of the monolayer is monitored by the Wilhelmy-plate method. This technique involves a plate being partially suspended within the subphase, the force due to the surface tension. The surface pressure is equal to the surface of the liquid phase (γ) minus the surface tension with the monolayer (γ_0).²⁵ For the deposition of the amphiphilic monolayer from the trough to the solid substrate (figure 2.4), the surface pressure must be kept constant throughout. The pressure is of critical importance to ensure homogenous, uniform packing, with pressures below 10 mN/cm usually is ineffective and above 40 mN/cm, can pose film rigidity and lead to buckling.

The transfer ratio of the surface pressure of the packed monolayer and the deposition stroke parameter reflects both the quantity and quality of the deposition of the bilayer onto the substrate. This being the decrease in monolayer area during deposition stroke and the area of the substrate and in the ideal situation should be equal to 1.²⁵

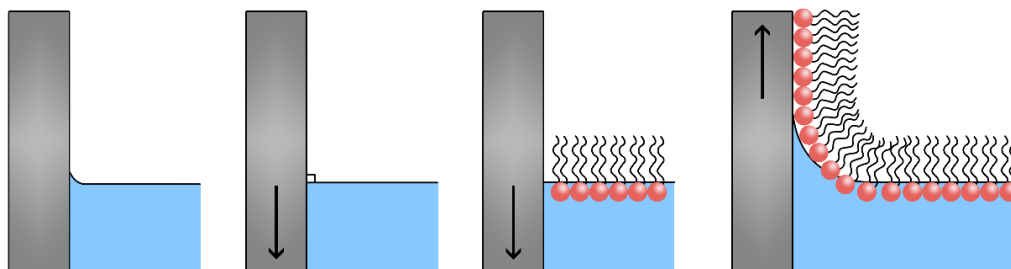


Figure 2.4: Schematic showing the process of monolayer deposition on a substrate using the Langmuir Blodgett technique.

The substrate's affinity for water dictates the order in which a Langmuir-Blodgett film is transferred. In the case for our hydrophilic substrate, the first layer of the film is transferred by raising the substrate from the sub-phase through the monolayer. This results in polar ends being bound to the substrate while the non-polar end being in the gas phase.

2.1 Materials and methods

2.1.1 Materials

1,2-dioleoylsn-glycero-3-phosphocholine (DOPC) were purchased with the maximum degree of purity (>99%) from Avanti Polar Lipids (Alabama, USA) without the need for further purification. Phosphate buffer saline (PBS) tablets were purchased from Sigma-Aldrich(Wicklow, Ireland). Gold wafers were purchased from AMS Biotechnology (Abingdon, UK).Polybead microspheres were purchased from Polysciences Europe GmbH (BadenWürttemberg, Germany) Aqueous solutions were prepared using MilliQ water (18 m Ω) (Millipore Corp. Bedford, USA). 6-mercapto-1-hexanol, 6-mercaptohexanoic acid where both purchased from Sigma Aldrich (Wicklow, Ireland), hydroxyl-terminated PEG thiol (N7) were purchases from Polypure AS (Oslo, Norway). Mica sheets 100 x 50mm x 25mm x 0.15mm purchased from SPI (West Chester, PA, USA). Polydimethylsiloxane silicon elastomer (PDMS) was purchased from Dow GmbH (Wiesbaden, Germany) and mixed following supplier's instructions. The gold salt solution used in the fabrication of the microcavity arrays which is a commercial gold plating solution, was purchased from Technic Inc, Sodium Gold Sulfite Solution, Cranston, RI, USA. Tetrahydrofuran (THF, 99%), Chloroform (> 99.5%) and, ethanol (> 99.5%) or equal were all purchased from Sigma Aldrich, Ireland.

2.1.2 Methods

2.1.2.1 Fabrication of gold cavity arrays

The gold microcavity arrays were prepared using the method previously reported by Basit et al. As seen in figure 2.5, polystyrene microspheres of 2 μ m in size were dropped casted onto vapour deposited gold coated silicon wafers (1.5 cm x 0.8 cm). The polystyrene spheres (PS) were dried overnight in a 4 °C refrigerator. Gold was electrodeposited onto the polystyrene microsphere covered gold silicon by using the gold coated silicon as the working electrode.

A potential of - 0.6 mV (vs Ag/AgCl) was held until the gold had deposited to the equator of the PS. Following deposition, the array was rinsed with ethanol to remove any remaining gold solution. After, PS were removed by sonication in THF for 10 mins and rinsed with ethanol.

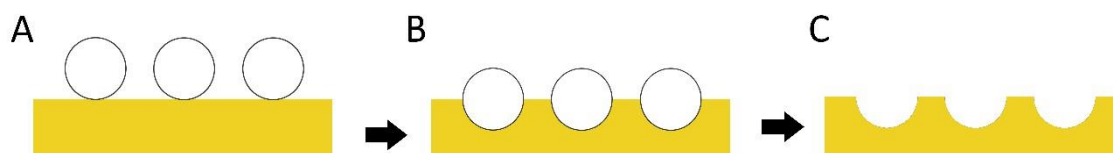


Figure 2.5: Schematic representation of the fabrication of gold microcavity array (A) polystyrene microspheres of 2 μm in size were dropped casted onto a 100 nm gold wafer manufactured by vapour deposition. (B) Using the gold as a working electrode, gold was electrodeposited onto the wafer by holding the electrode at a potential of -0.6 V (vs Ag/AgCl). (C) The PS was removed from the substrates through sonication in THF for 10 mins and rinsed with ethanol.

2.1.2.2 Scanning Electron Microscopy

The morphology of the microcavity array platform was characterised by Scanning Electron Microscopy (SEM). SEM images were obtained using a Hitachi S-3200n scanning electron microscopy. All measurements were carried out at a probe current of 35 μA , aperture size 3 and an accelerating voltage of 10 kV. Images were taken across 3 different sections per sample.

2.1.2.3 Surface modification

The exterior surface of the arrays were selectively modified with 10 mM 6-mercapto-1-hexanol, hydroxyl terminated PEG thiol and 6-mercaptohexanoic acid to allow for the binding and formation of a bilayer. The surface modification occurs through the binding of the thiol SH group to the gold, resulting in an ordered monolayer. Cavities were functionalised micro contact printing (μCP). μCP involves the use (block and ink) of a PDMS template. As per figure 2.6, PDMS substrates were made at a 10:1 ratio. Mica templates of an area 1.5 cm^2 were placed onto a glass slide.

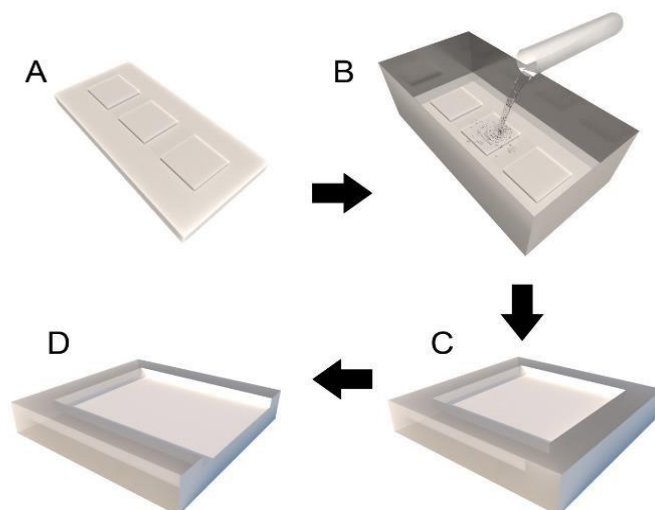


Figure 2.6: Schematic representation of the fabrication of the PDMS templates. (A) Mica pieces were glued to a glass slide. (B) PDMS was poured into the tinfoil and thermally cured at 100°C for 1 hr. (C) Templates were removed from the glass slide. (D) One side of the template was cut.

The PDMS substrates were treated with a Harrick PDC-002 Plasma (Harrick Plasma Inc.) and air plasma cleaner for 10 seconds at 1000 mT of pressure, using air as the process gas, to render the surface hydrophilic. As shown in figure 2.7, the plasma oxidises the methyl groups on the surface of the PDMS leading to a SiO_x network with interfacial hydroxyl groups being formed giving a hydrophilic surface.^{26,27}

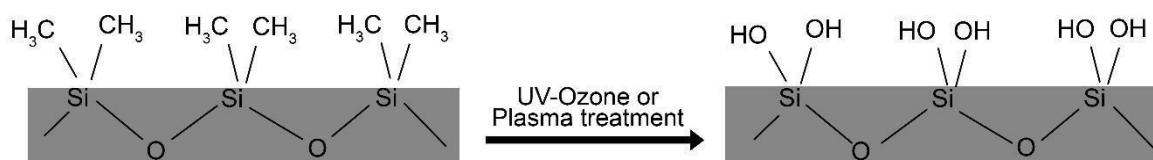


Figure 2.7: Shows a schematic of a PDMS substrate before plasma treatment and post plasma treatment.²⁸

The SAM was then inked onto the plasma treated PDMS template as seen in figure 2.8. The ethanol was allowed to evaporate prior to adding the microcavity arrays onto the functionalised PDMS template as seen in figure 2.8.

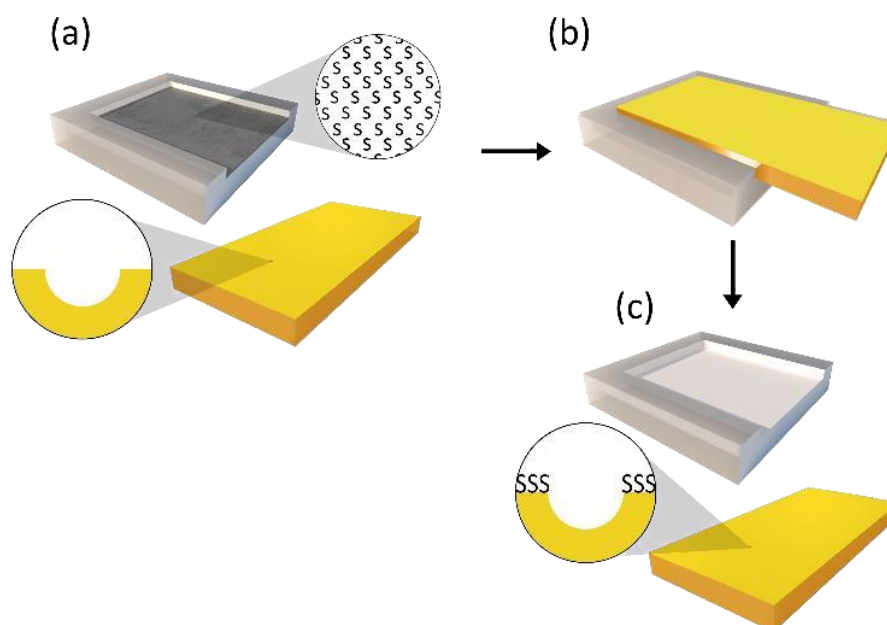


Figure 2.8: Diagram of the surface modification of the cavity array. (a) is the PDMS “inked” with SAM (b) Functionalisation of the cavity surface. (c) Post cavity functionalisation.

2.1.2.4 Electrochemical characterisation

2.1.2.4.1 Cyclic voltammetry

The assembly of the SAM and subsequent bilayer at the microcavity array was evaluated by Cyclic voltammetry (CV). CVs were collected using a three electrode cell, the substrate as a working electrode, Ag/AgCl as a reference electrode and a platinum wire as a counter electrode. 10 mM potassium ferricyanide was used as a redox probe in 1 M potassium chloride (KCl). Post surface functionalisation, initially at different time intervals followed by different pressure intervals, CV was used to characterise the array surface by evaluating its capacity to block ferricyanide oxidation. The potential was varied from 0 to 0.6 V.

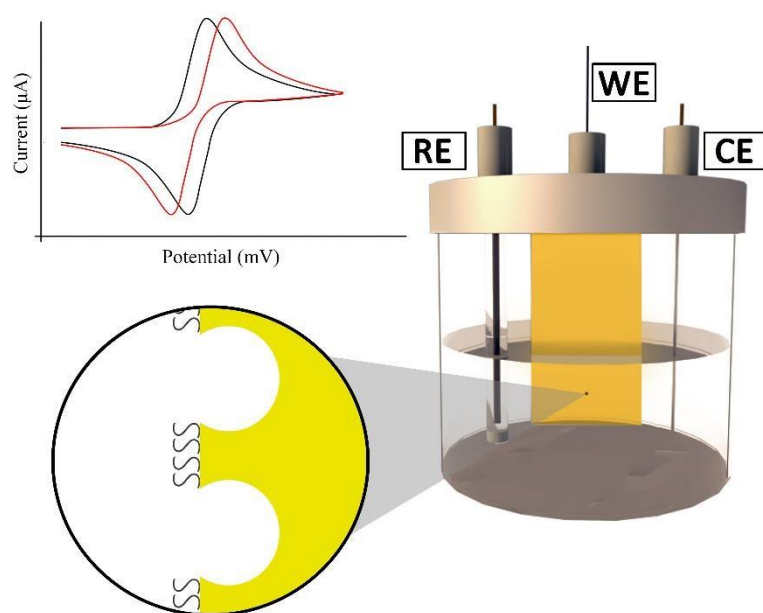


Figure 2.9: Schematic of an electrochemical cell of a three electrode working system where the working electrode is the MSLB. Where RE is the reference electrode, WE are the working electrode and CE is the counter electrode.

2.1.2.5 Formation of lipid bilayers

Vesicles were prepared by taking 20 μl of a lipid solution (Avanti) of a 50 mg/ml stock in chloroform and evaporating it in a glass vial under a constant stream of nitrogen. To ensure full drying of the lipids, the vial was placed under vacuum for 30 mins before resuspension in 1ml of PBS. The vesicles are extruded through 100 nm polycarbonate membrane a minimum of 11 times, to form monodisperse vesicles. To form a monolayer by Langmuir-Blodgett methods, DOPC in chloroform was placed onto the air-water interface on the NIMA 120 cm Langmuir-Blodgett trough (NIMA Inc.) using Milli-Q water for the water phase. The trough was left for 10 min to allow the evaporation of the chloroform.

Prior to the microcavity being lowered into the interface and withdrawn to allow the monolayer to transfer onto the surface, it was sonicated in PBS, pH 7.4 to ensure aqueous filling of the pores. As seen in figure 2.10, gold microcavity arrays were clipped to the dipper of the instrument and immersed at a speed of 150 mm/min, the barriers were compressed at a pressure of 32 mN/m and removed at 5 mm/min. The array was then immersed in vesicle solution for 1 hr to form a bilayer.

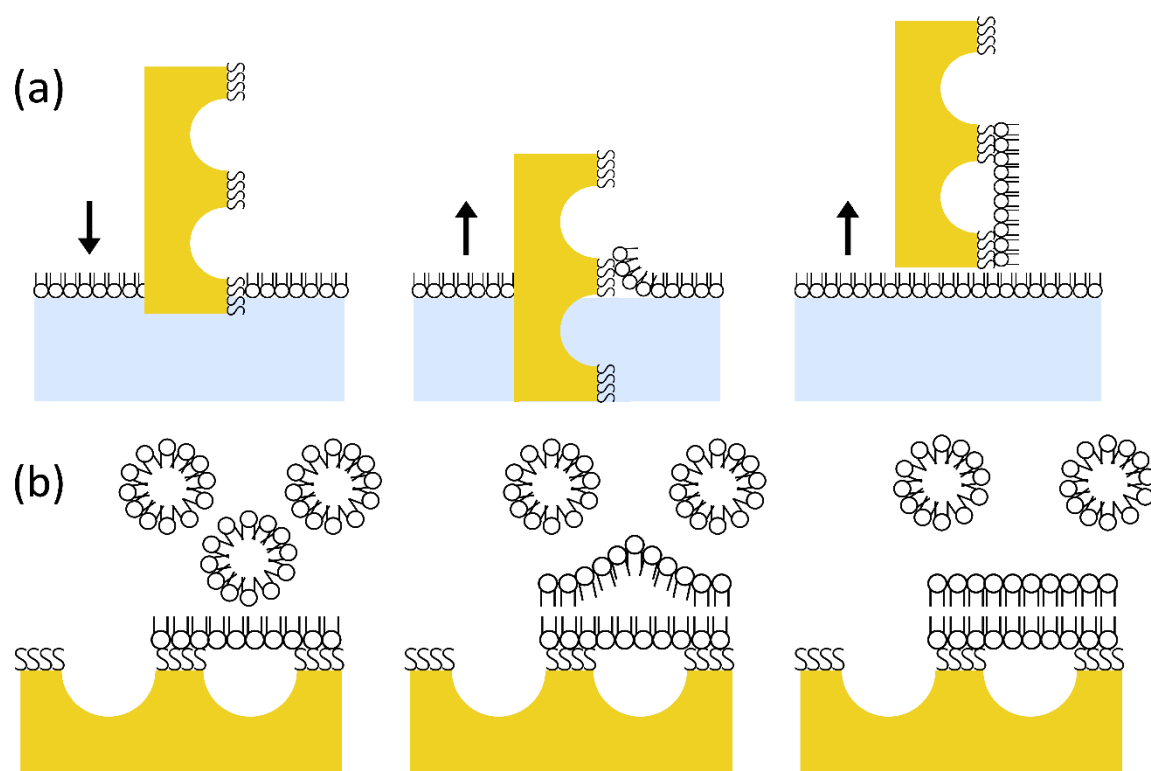


Figure 2.10: The modified microcavity array is placed in the Langmuir-Blodgett trough with lipids compressed at the surface. (a) Where a monolayer is formed as the array is slowly removed from the trough and the lipids self-assemble across the sample. (b) The sample is incubated in a vesicle solution, the vesicles disrupt forming the outer layer of the bilayer.

2.1.2.6 Surface enhanced Raman Spectroscopy

A Horiba LabRAM was used with a 50x magnification objective. A 785 nm was used as the excitation wavelength and a 300 μm slit was used for measurements. A silicon wafer along with the Rayleigh line was used to calibrate the instrument before use.

2.1.2.7 Electrochemical Impedance Spectroscopy

EIS was carried out using a CH Instrument model 760E Electrochemical workstation. The electrochemical cell comprised of a three electrode system comprising of a platinum wire as an auxiliary electrode, an Ag/AgCl reference electrode and the microcavity array as the working electrode. EIS measurements were measured with an AC modulation amplitude of 0.01 V at a potential bias of 0 V (vs Ag/AgCl) over a frequency range of 100,000 Hz to 0.01 Hz. The electrochemical impedance response was performed in a 5 mL PBS pH 7.4 in a 10 mL glass beaker and measured every 1 hr over a 20 hr period, each measurement taking 10 min and was carried out at room temperature (20°C).

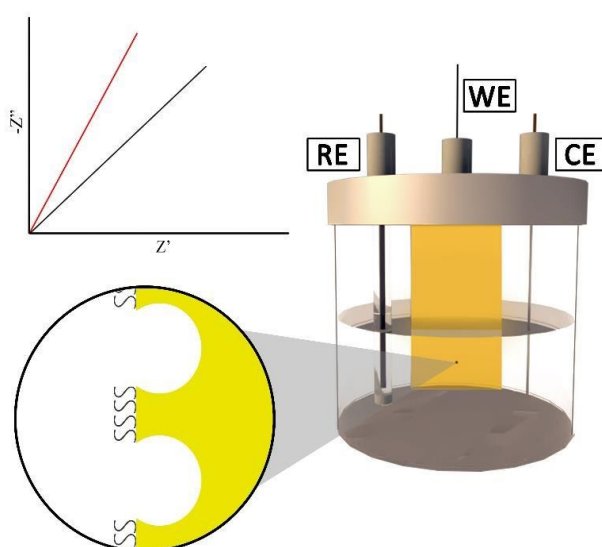


Figure 2.11: Schematic of an electrochemical cell of a three electrode working system where the working electrode is the MSLB. Where RE is the reference electrode, WE is the working electrode and CE is the counter electrode.

2.1.2.8 Cyclic Voltammetry

As described in section 2.2.2.4

2.2 Results and Discussions

Keyes research group have demonstrated that solution deposition as an effective method for selectively modifying the top surface of the array using PS spheres to mask the interior of the cavity. Although this is an effective method for surface functionalisation it is a time consuming process that requires several steps including a 12 hr solution deposition step followed by a THF wash step to remove the PS spheres. Here we examine a new and alternative method for selective SAM deposition at the cavity array top surface by applying μ CP as an alternative approach to solution deposition.

2.2.1 Comparison of solution deposition and μ CP functionalisation methods at planar gold surfaces

In order to compare the effectiveness of the surface functionalisation methods surface coverage of 10 mM 6-mercapto-1-hexanol at arrays prepared by solution phase deposition was compared to those prepared by microcontact printing (μ CP). CVs were collected using 10 mM potassium ferricyanide in 1 M KCl as the electrolyte on three plain gold arrays. Using the planar gold wafer as the working electrode, CVs were collected at various scan rates between the potential 0 to 0.6 V, as seen in figure 2.12.

The Randles-Sevcik equation, which relates the peak current to diffusion coefficient of a reversible redox reaction and if D is known it can be used to estimate the electroactive area of the working electrode by applying i_p versus $v^{1/2}$, where i_p is the peak current according to equation 2.6, where n is the number of electrons transferred, F is the Faradays constant, A being the area of the electrode in cm^2 , D is the diffusion coefficient for the potassium ferricyanide ($7.09 \times 10^{-6} \text{ cm}^2/\text{s}$), C is the concentration of potassium ferricyanide used in mol/cm^3 and v is the scan rate in V/s .

$$i_p = 0.44643 nFA C \left(\frac{nFvD}{RT}\right)^{\frac{1}{2}}$$

Equation 2.6

A plot of $(\text{scan rate})^{1/2}$ vs. peak current for the substrate along with the linear fit is shown in figure 2.12.

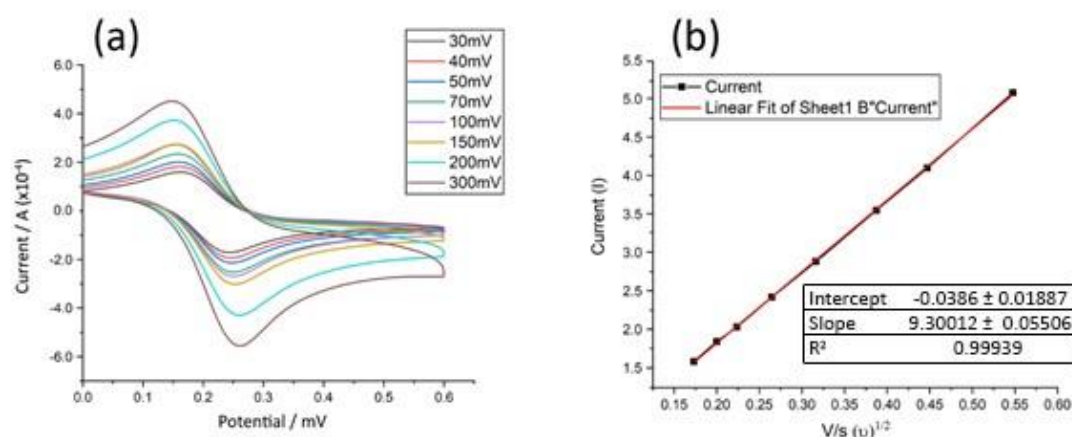


Figure 2.12: (a) A CV of a planar gold array measured in 10 mM $\text{K}_4[\text{Fe}(\text{CN})_6]$ and 1 M KCl as the electrolyte at 300, 200, 150, 100, 70, 50, 40, 30 mV/s . (b) Shows a plot of $\sqrt{\text{Scan rate}}$ Vs. oxidation peak current. The current plotted is the average oxidation peak of 3 different untreated planar gold electrodes (vs. Ag / AgCl). All electrodes were measured using a standard 3 electrode set up in using 10 mM potassium ferricyanide in 1 M KCl as the supporting electrolyte and measured from 0 to 0.6 V (vs. Ag/AgCl) at a scan rate of 100 mV/s

It can be seen from the plot of i_p versus $v^{1/2}$ that the trend line R^2 of 0.99 that the Fc couple is well behaved at the unmodified cavity array electrode surface. The surface of the plot in figure 2.12 (b) was fitted to the Randles-Sevcik (equation 2.6)

An average geometric area for planar gold arrays was estimated to be 1.05 cm^2 with a standard deviation of $\pm 0.27 \text{ cm}^2$. The small deviation between the electrodes means that the planar gold arrays were prepared with acceptable uniformity. The surface coverage can be estimated from the oxidation peak of the CV using the following equation to calculate the surface coverage of the ferrocene:

$$\Gamma = \frac{Q}{nFA}$$

Equation 2.6

Where Q is the oxidation peak area, n is the number of electrons transferred (which is 1), F is Faraday's constant ($9.6487 \times 10^4 \text{ C / mol}$) and A is the electro-active area of the electrode. CV's of the gold cavities were measured in 10 mM potassium ferricyanide to see the effect of the surface functionalisation on the surface electrochemistry of the working electrode. the electro-active surface of each electrode for the two methods is seen in table 2.1.

Table 2.1: Comparison of the surface coverage of 10 mM 6-mercapto-1-hexanol solution deposition overnight and the electroactive surface area of in 10 mM 6-mercapto-1-hexanol using 30 min μ CP on planar gold substrates. This was conducted using Randles-Sevciks equation using the charge from 100 mV CV of soaked and μ CP CV on 3 different planar gold. All electrodes were measured using a standard 3 electrode set up in using 10 mM potassium ferricyanide in 1 M KCl as the supporting electrolyte and measured from 0 to 0.6 V (vs. Ag/AgCl) at a scan rate of 100 mV/s.

Electrode	Solution deposition (mol cm ⁻²)	μ CP (mol cm ⁻²)
1	1.04 x 10 ⁻¹⁰	1.09 x 10 ⁻¹⁰
2	1.22 x 10 ⁻¹⁰	1.56 x 10 ⁻¹⁰
3	1.03 x 10 ⁻¹⁰	1.07 x 10 ⁻¹⁰
Average	1.10 x 10 ⁻¹⁰	1.24 x 10 ⁻¹⁰
Standard Deviation	0.11	0.28

This result indicates that the solution deposition method is comparable to the μ CP method, with μ CP offering the possibility of functionalising the surface of the array similar to that of solution deposition without modifying the cavities interior.

2.2.1 Characterisation and functionalisation of Gold microcavity Arrays by μ CP method

SEM was used to characterise the topology of the gold cavity arrays fabricated by sphere lithography and gold electrodeposition as described in section 2.1.2.1. THF was used to remove the spheres prior to imaging the structures of the cavities were assessed by SEM as seen figure 2.13.²⁹ The data confirm the sphere lithographic method used, which is a recently improved method, leads to a well order, packed arrays as seen in figure 2.13.

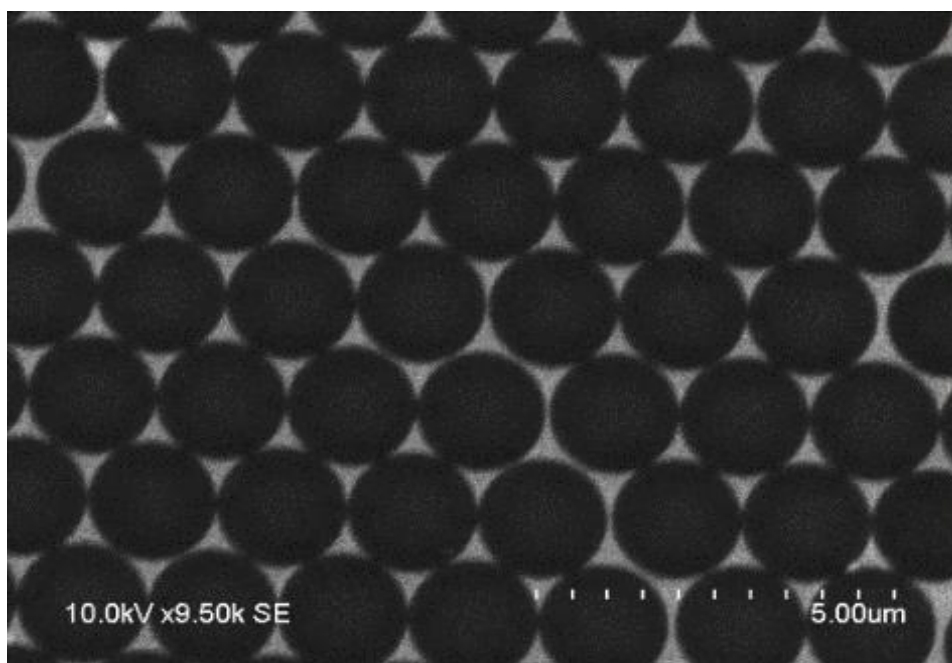


Figure 2.13: SEM of 1.83 μm of sphere lithography electrochemically deposited array.

Figure 2.14 shows a close up image of array diameters of 1.83 μm of the electrochemically deposited gold arrays following the removal of 2 μm onto polystyrene microspheres using THF. This image shows that the gold electro-deposition technique produces arrays formed to approximately the equator of the deposition sphere as reported previously.^{11,30} However, although the potential of - 0.6 V (vs Ag/AgCl) was held until the gold had deposited to the equator of the PS there is a degree of variability within this method. The electrodeposition method relies on the judgement based on the coulometric curve in the manufacturing of the array, whether the gold has deposited to the PS diameter and hence the degree of variability.

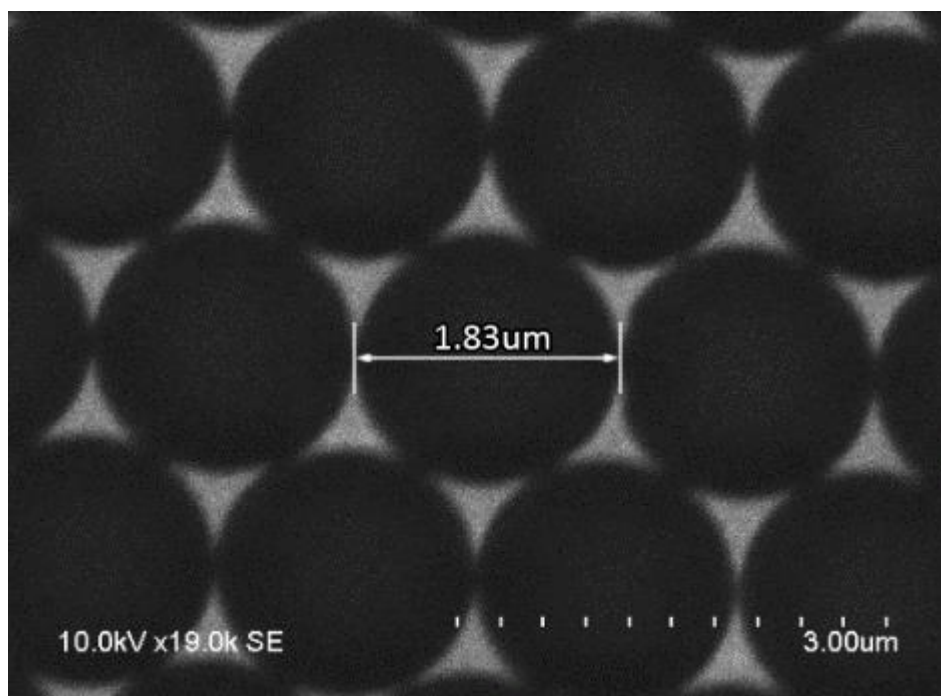


Figure 2.13: SEM of 1.83 μm packed cavity array.

2.2.2.8 Optimisation of microcontact printing parameters

To optimise the μCP conditions described above for planar electrodes to the microcavity array electrodes, voltammograms of the array functionalised at different time intervals followed by different pressure intervals were conducted using 10 mM potassium ferricyanide in 1 M KCl at 100 mV/s scan rate between a potential of 0 – 0.6 V. From the 10 mM 6-mercapto-1-hexanol μCP timed experiment, figure 2.14 it can be seen a peak to peak separation, ΔE of an unmodified array of 0.08 V. However, between the 15 min, 30 min and 24 hr voltammograms, the anode peak measured at 0.358 V for 15 min, 0.388 V for 30 min and 0.392 V for 24 hr. With a small difference in peak separation between the 30 min and 24 hr voltammogram, the 30 min μCP time was used the optimal time which was then applied to studies to determine the optimal pressure to apply between deposition surface and μCP substrate.

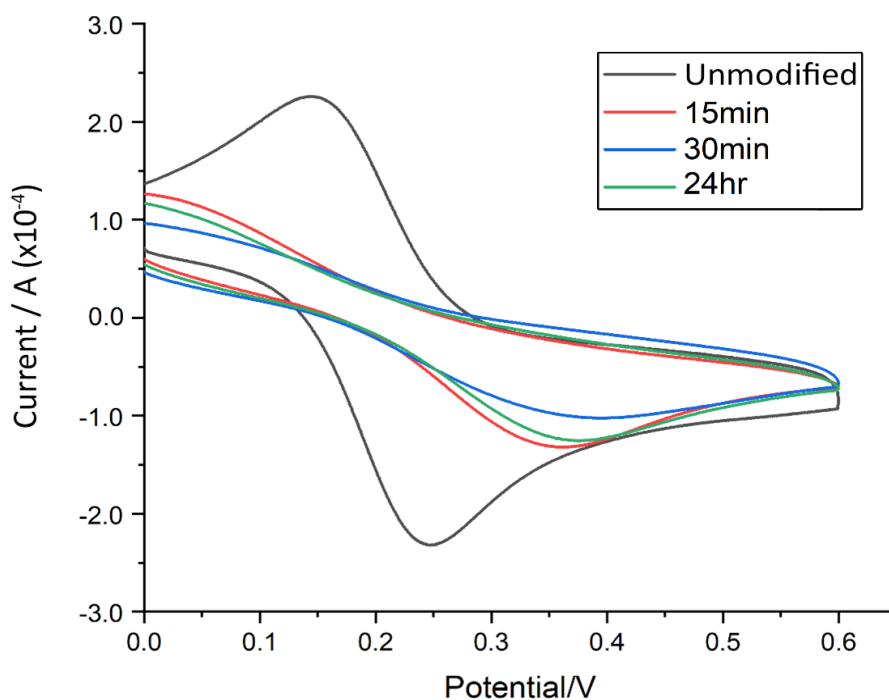


Figure 2.14: Comparison of voltammetry of electrochemically deposited platform at different μ CP time intervals of 10 mM 6-mercapto-1-hexanol using cyclic voltammetry.

Where the grey is no surface coverage, red is coverage after 15 min μ CP, blue is coverage after 30 min μ CP and green is coverage after 24 hr μ CP. All electrodes were measured using a standard 3 electrode set up in using 10 mM potassium ferricyanide in 1 M KCl as the supporting electrolyte and measured from 0 to 0.6 V (vs. Ag/AgCl) at a scan rate of 100 mV/s.

Using the 30 min μ CP time different pressures for the contact printing were applied to optimise coverage, ranging from 0.06 Pa to 1.8 Pa using 10 mM 6-mercapto-1-hexanol and the result assessed by CV. In comparison to the unmodified array platform, it is evident from voltammetry that thiol deposition decreases in voltametric response due to blocking of the electrode between 0.3 Pa and 1.2 Pa (figure 2.16).

This is evident from the peak shift of the array functionalised with a 30 min μ CP with no pressure applied was 0.29 V.

There was a significant increase in the surface coverage of the modified surface with the anodic peak at 0.36 V with 30 min μ CP with 0.3 Pa of pressure. Similarly, there is little further change to the voltammetric response of the modified array following deposition at 0.6 Pa, 0.9 Pa or 1.2 Pa with only modest shifts of the anodic peak from 0.37 V to 0.382 V and 0.412 V with further increases in pressure. This indicates there are only small changes in surface coverage with increasing pressure between the 0.6 Pa and 1.2 Pa . These large changes in voltammetric responses, particularly at higher pressures could be credited to the functionalisation of the interior of the array. This suggests that using lower pressures for deposition as a precaution to avoid the functionalisation of the cavities interior.

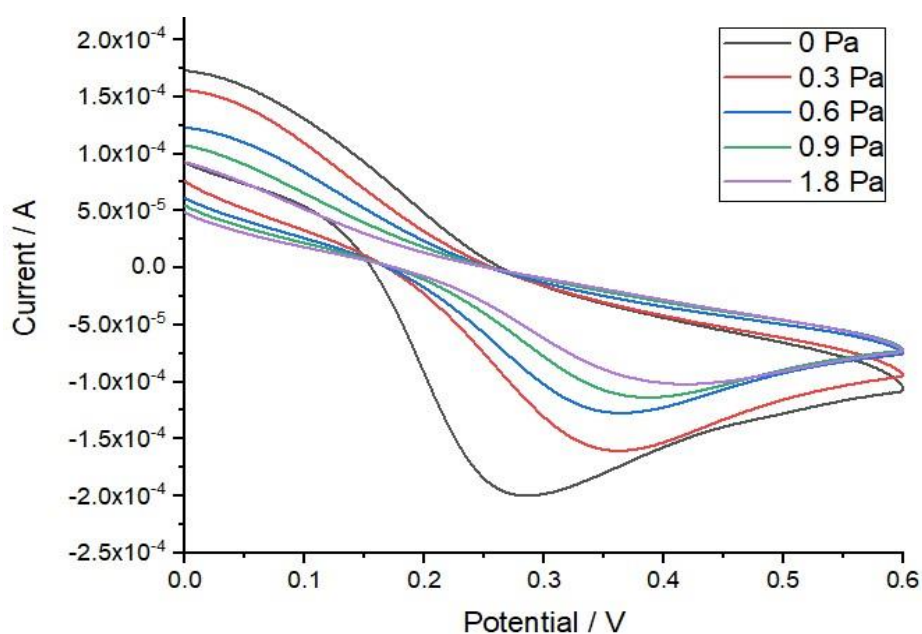


Figure 2.16: Cyclic voltammetry of platform at different 30 min μ CP at pressure intervals using 10 mM 6-mercapto-1-hexanol. Where black is of a platform at 30 min time, 30 min is μ CP time at 0.3 Pa, blue is of 30 min μ CP time at 0.6 Pa, green is of 30 min μ CP time at 0.9 Pa and purple is of 30 min μ CP time at 1.8 Pa. All electrodes were measured using a standard 3 electrode set up in using 10 mM potassium ferricyanide in 1 M KCl as the supporting electrolyte and measured from 0 to 0.6 V (vs. Ag/AgCl) at a scan rate of 100 mV/s.

2.2.2 Electrochemical Impedance Spectroscopy of Lipid membrane on gold arrays

EIS was used to analyse the effect of SAMs with separate end termini on the array's capacity to sustain a bilayer on three separate electrodes. EIS is a highly sensitive tool that reflects changes in electrode impedance as a result of surface chemical changes, offering clear insight into membrane admittance, packing, permeability, and stability. Since the cavity order differs slightly from array to array, and hence the electrode geometric area varies, relative resistance changes are discussed here to facilitate comparison, rather than absolute resistance changes.

Figure 2.22 shows the microcavity array with the PS spheres dissolved. Upon 30 min μ CP under 0.6 Pa pressure using 10 mM 6-mercapto-1-hexanol, an increase in resistance is seen as a SAM forms on the gold surface. There is a further increase in resistance as seen caused by the addition of the lipid membrane to the array by Langmuir-Blodgett method followed by vesicle fusion.

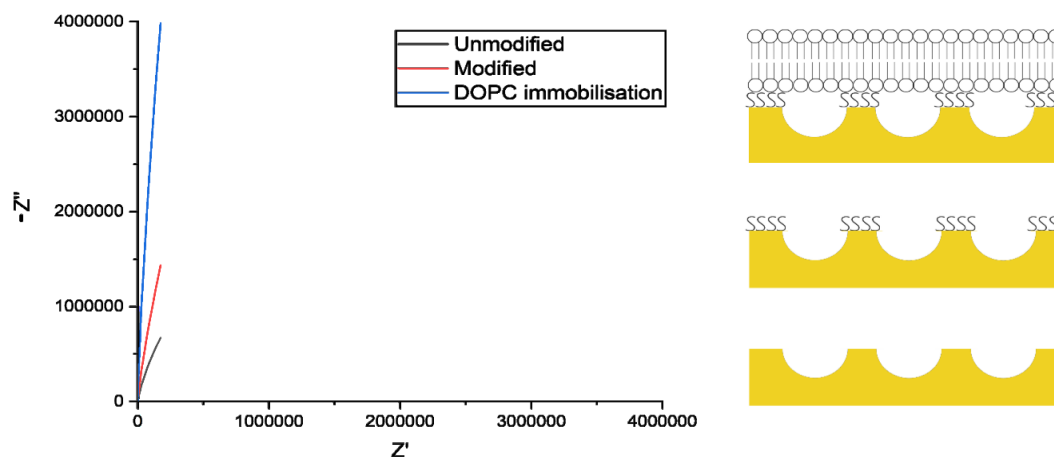


Figure 2.22: Electrochemical impedance spectroscopy Nyquist plot of the fabrication steps for MSLB, using LB followed by vesicle fusion on a PS lithographically prepared pre-aqueous filled microcavity array modified with 10 mM 6-mercapto-1-hexanol. Black represents bare microcavity array. Red represents the microcavity array functionalised in 6-mercapto-1-hexanol where blue presents the microcavity array supporting a DOPC bilayer. All measurements were measured in triplicate and conducted using a 30 min μ CP time with 0.6 Pa pressure in PBS buffer at pH 7.4 within the experimental window of 20 hrs. A standard 3-electrode system at 0 V (vs Ag/AgCl) using an AC amplitude of 0.01 V with a frequency range of 1 MHz to 0.01 Hz.

Nyquist plots contain complex impedance data originating from both the resistance and capacitance of the cell. This data results from both real, Z_{re} and imaginary, Z_{im} components. The graphical representations of impedance offer significant insight into the change of membrane over time. However, equivalent circuit models (ECM) can be used to get actual resistance values of the lipid bilayer shown in the figure 2.23. The ECM model can be applied to impedance data and should represent the system in question. These model membranes were applied to electrochemical impedance spectroscopy where the bilayers stability is assessed by their corresponding EIS signal over 20 hrs. The circuit in figure 2.23 for instance consists of R_s , which is the solution resistance in series the resistor, R_m and capacitor, C_m in parallel corresponds to the self-assembled monolayer and the lipid bilayer on the surface.

The circuit consists of a resistance component, which corresponds to the resistance of the microcavities (R_c) and a double layer capacitance C_{dl} . The circuit uses a Constant Phase Element (CPE) component, given by $Z_{CPE} = Q^{-1} (j\omega)^{-\alpha}$ Where the magnitude of the capacitance is given by Q , the angular frequency is ω and α being a real number between 1 and 0.

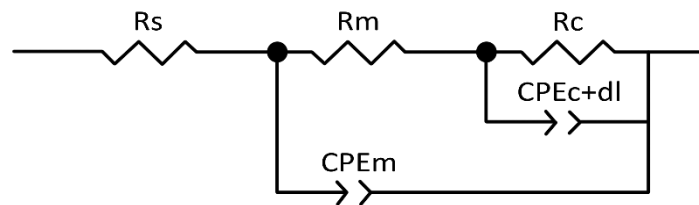


Figure 2.23: ECM model used in fitting AC impedance data. Where R_s , R_c and R_m are the resistance of the solution, the cavities resistance and resistance of the membrane. CPE_{c+dl} and CPE_m are the electrode double layer constant phase element and the constant phase element of the membrane.

It is not expected that the R_s of the contacting solution will change. Similarly, R_c is not expected to change during the measurement. Similarly, with biological cells, the biomimetic MSLB acts as a semi-permeable barrier. To evaluate the effectiveness in a SAM in supporting a lipid bilayer across the aqueous filled arrays, the stability of the bilayers at each SAM type were explored by EIS. Impedance measurements were carried out on a DOPC supported using 10 mM of 6-mercapto-1-hexanol.

As shown in figure 2.24 (a) below, following 4 hrs for the lipid membrane to reach its equilibrium the membrane resistance of the DOPC symmetric bilayer was found to be stable for 7 hrs. Figure 2.24 (b) shows that the impedance response significantly alters over 60 min with very little change after. This shows that after 60 mins that the 6-mercapto-1-hexanol on the array is stable.

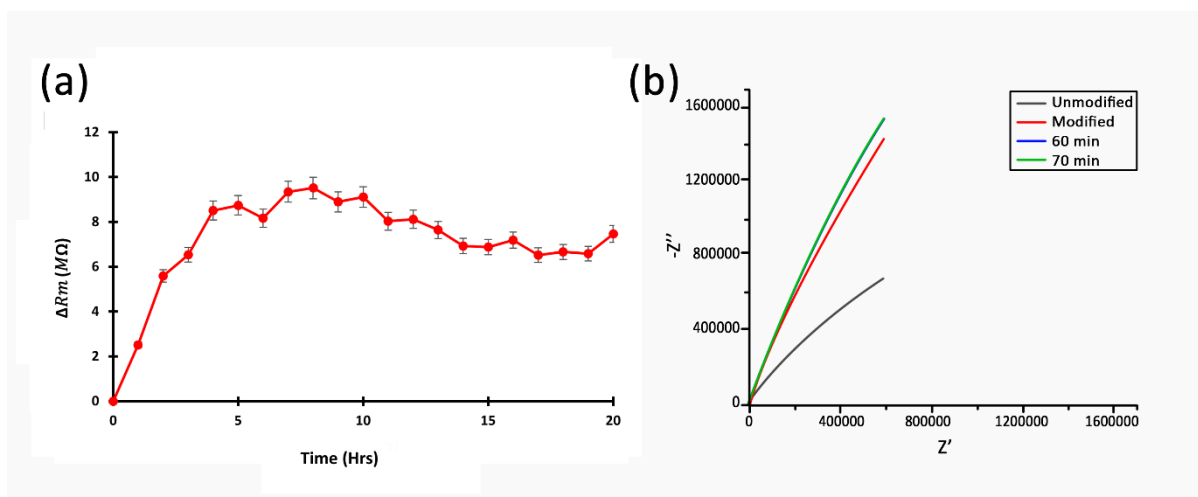


Figure 2.24: (a) The relative change in resistance of a DOPC bilayer prepared using LB followed by vesicle fusion on a PS lithographically prepared pre-aqueous filled microcavity array platform modified with 10 mM 6-mercapto-1-hexanol. (b) Nyquist plot of this substrate, unfunctionalised (grey), post after functionalisation (red), 60 min post modification (blue) 70 min post modification (green). All measurements were conducted using a 30 min μ CP time with 0.6 Pa pressure in PBS buffer at pH 7.4 within the experimental window of 20 hrs. A standard 3-electrode system at 0 V (vs Ag/AgCl) using an AC amplitude of 0.01 V with a frequency range of 1 MHz to 0.01 Hz.

The array functionalised with 10 mM hydroxyl terminated PEG thiol was used to support a DOPC bilayer membrane. Prepared as before, at pre-aqueous filled arrays using DOPC LB and then vesicle fusion as shown in the figure 2.25 (a), the membrane resistance of the DOPC symmetric bilayer was found to be stable for 8 hrs.

In comparison to the DOPC membrane supported by 6-mercapto-1-hexanol to membranes supported by hydroxyl terminated PEG thiol 6-mercapto-1-hexanol shows less membrane stability but comparable change in membrane resistance.

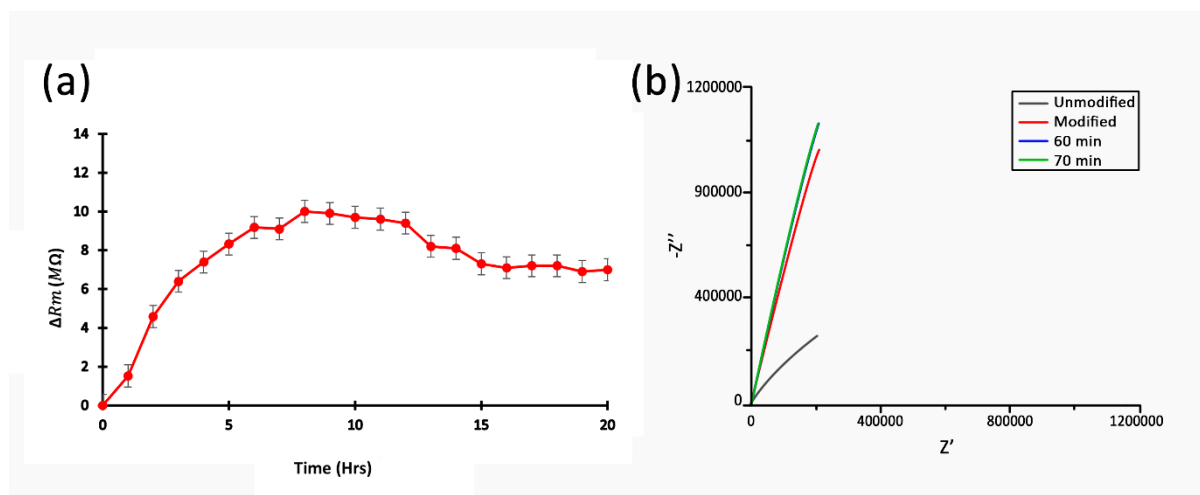


Figure 2.25: (a) The relative change in resistance of a DOPC bilayer prepared using LB followed by vesicle fusion on a PS lithographically prepared pre-aqueous filled microcavity array platform modified with 10 mM hydroxyl terminated PEG thiol. (b) Nyquist plot this substrate, unfunctionalised (grey), post after functionalisation (red), 60 min post modification (blue) 70 min post modification (green). All measurements were conducted using a 30 min μ CP time with 0.6 Pa pressure in PBS buffer at pH 7.4 within the experimental window of 20 hrs. A standard 3-electrode system at 0 V (vs Ag/AgCl) using an AC amplitude of 0.01 V with a frequency range of 1 MHz to 0.01 Hz.

The array was then functionalised using 10 mM 6-mercaptophexanoic acid was used to support a DOPC membrane. As shown in figure 2.26 below, the membrane resistance of the DOPC symmetric bilayer was found to be completely unchanging within experimental error for 5 hrs but with only very modest changes over 10 hours.

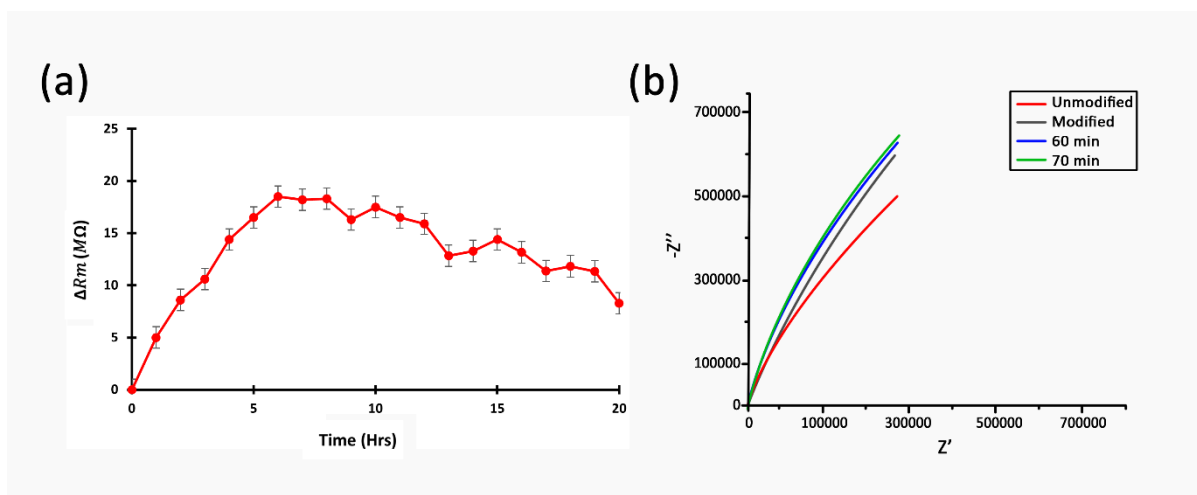


Figure 2.26: (a) The relative change in resistance of a DOPC bilayer prepared using LB followed by vesicle fusion on a PS lithographically prepared pre-aqueous filled microcavity array platform modified with 10 mM 6-mercaptophexanoic acid. (b) Nyquist plot of this substrate, unfunctionalised (red), post after functionalisation (grey), 60 min post modification (blue) 70 min post modification (green). All measurements were conducted using a 30 min μ CP time with 0.6 Pa pressure in PBS buffer at pH 7.4 within the experimental window of 20 hrs. A standard 3-electrode system at 0 V (vs Ag/AgCl) using an AC amplitude of 0.01 V with a frequency range of 1 MHz to 0.01 Hz.

However, in contrast to a DOPC membrane supported on 6-mercapto-1-hexanol and hydroxyl terminated PEG thiol, a DOPC membrane supported by 6-mercaptophexanoic acid shows a membrane stability of 5 hrs. The hydroxyl terminated end groups of both the 6-mercapto-1-hexanol and the hydroxyl terminated PEG thiol yielded similar results in terms of membrane stability and relative change in membrane resistance over a 20 hr period.

The similar results between these two SAMs is expected, as both SAMs possess the same hydroxyl terminated end groups, which in a well packed monolayer will mainly dictate the surface chemistry. In figure 2.26, 6-mercaptophexanoic acid with a carboxylic acid end terminixhibited significantly less membrane stability with no changes within the standard deviation at 5 hrs.

The Nyquist plots, of 6-mercapto-hexanol, hydroxyl terminated PEG thiol and 6-mercaptohexanoic acid SAM formation on the gold interface was stable after 60 mins which suggests the difference in stability between 6-mercapto-1-hexanol and the hydroxyl terminated down to the carboxylic acid end terminus. Critically the scale of change in membrane resistance, is very different between the two hydroxyl terminated SAMs at 8 to 10 m Ω for hydroxyl compared with the carboxylic acid with changes in membrane resistance of 16 to 18 m Ω over the time scale explored.

2.2.3 Determination of Lipid Bilayer formation and stability

2.2.3.1 Surface enhanced Raman Spectroscopy

To support a DOPC phospholipid bilayer on the gold microcavity array, the substrates top surface was modified with 10 mM 6-mercapto-1-hexanol by using 30 min μ CP under 0.6 Pa and was rendered hydrophilic. The cavities were sonicated with PBS for 20 min to ensure properly filling of the cavities.³¹ After sonication, the lipid bilayer were formed using Langmuir-Blodgett methods to form the proximal leaflet followed by vesicle fusion to form the distal leaflet as described in section 2.1.2.5.

After the formation of a DOPC bilayer on the functionalised microcavity array. Its presence was assessed using Raman spectroscopy, figure 2.16. A 785 nm laser wavelength was chosen for excitation as it coincides with both DRAQ7 which is a cell impermeable dye and the anticipated plasmon excitation for the 1.83 μ m microcavity arrays. Figure 2.18, shows a Raman spectrum of a DOPC bilayer supported by 6-mercapto-1-hexanol on a microcavity array platform. Initially, a spectrum was taken after five hours of bilayer formation, with no vibrational modes being present. After plasmonic disruption vibrational modes 429, 445 cm^{-1} as well as 1240, 1280 and 1322 cm^{-1} which is unique to DRAQ7 are present which indicates the presence of a membrane on the platform.

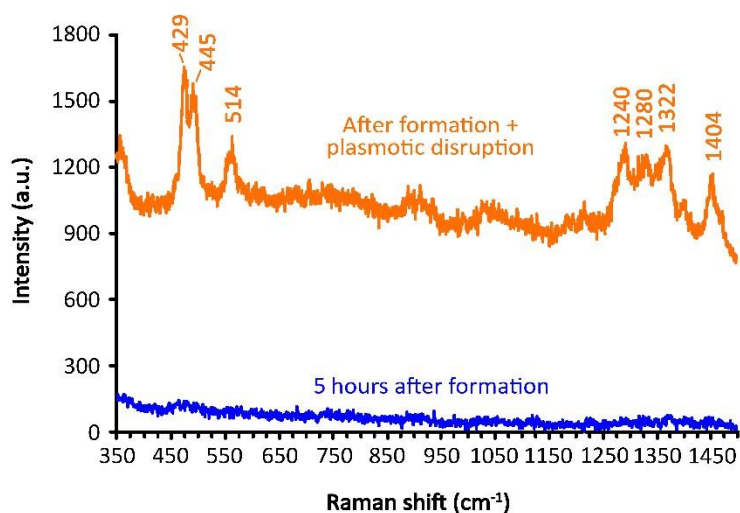


Figure 2.18: Shows an overlay of Raman spectra of a DOPC bilayer with 5 μM DRAQ7 over a PS lithography microcavity array using 785 nm excitation line at an incident laser power of 2.4 mW. The blue spectra were measured 5 hrs after LB followed by vesicle fusion, with no DRAQ7 signatures detected. While the orange spectra is of DOPC bilayer after plasmonic disruption were DRAQ7 signatures being detected. The array was functionalised using 6-mercapto-1-hexanol for 30 min μCP time with 0.6 Pa pressure.

Using six separate gold substrates, the effect of the topography of the underlying gold surface on the integrity of self-assembled monolayers (SAMs) of hexadecanethiol (HDT) formed by solution assembly and microcontact printing was investigated. Scanning tunnelling microscopy was used to inspect the bare substrates for roughness and flaws (STM). Surface methods (STM) and electrochemical measurements were used to assess the structural integrity of self-assembled monolayers on these substrates.³²

Interestingly, the quality of the monolayer is often best when fabricated on the flattest substrates. It is worth noting, though, that layer consistency is not always related to coverage variations. Given the fact that STM photographs of both the solution-formed and printed SAMs appeared identical, electrochemical inspection of the SAM integrity showed that the printed SAMs were inferior, creating a less efficient passivating barrier with more pinholes.

Rolling the inked stamp over the gold surface rather than positioning it horizontally on the substrate will vastly improve the consistency of printed SAMs. This second printing process, which involved rolling the stamp over the surface, created SAMs that were slightly inferior to those made with solution but could be manufactured in less than a minute instead of 24 hours.³³

2.2.3.2 Cyclic Voltammetry of Lipid membrane on the gold array

Cyclic voltammetry was used to assess the blocking of the redox probe from the surface and by inference the surface coverage of the SAMs as well as the lipid membranes on the electrode surface. The electron transfer at the electrode interface can occur in several ways; the first being through the permeation of the redox species into the monolayer, followed by the electron transfer at the electrode interface. The second interference occurring by the diffusion to defect sites or pinholes of the electroactive compound and the third source of diffusion by the direct tunnelling of the electrons through the monolayer.¹⁹

During the oxidation or reduction process, charge transfer occurs on the gold/solution interface where gold cavity was measured in 10 mM potassium ferricyanide to examine the effect of surface functionalisation on bilayer support. Figure 2.19 shows CVs of a microcavity array, one where the top surface is unmodified with the anodic peak being 0.233 V, followed by the surface modified by 10 mM 6-mercapto-1-hexanol, the anodic peak shifted to 0.321, followed by the support of a lipid bilayer on the SAM coated array where the anodic peak then shifted to 0.342 V.

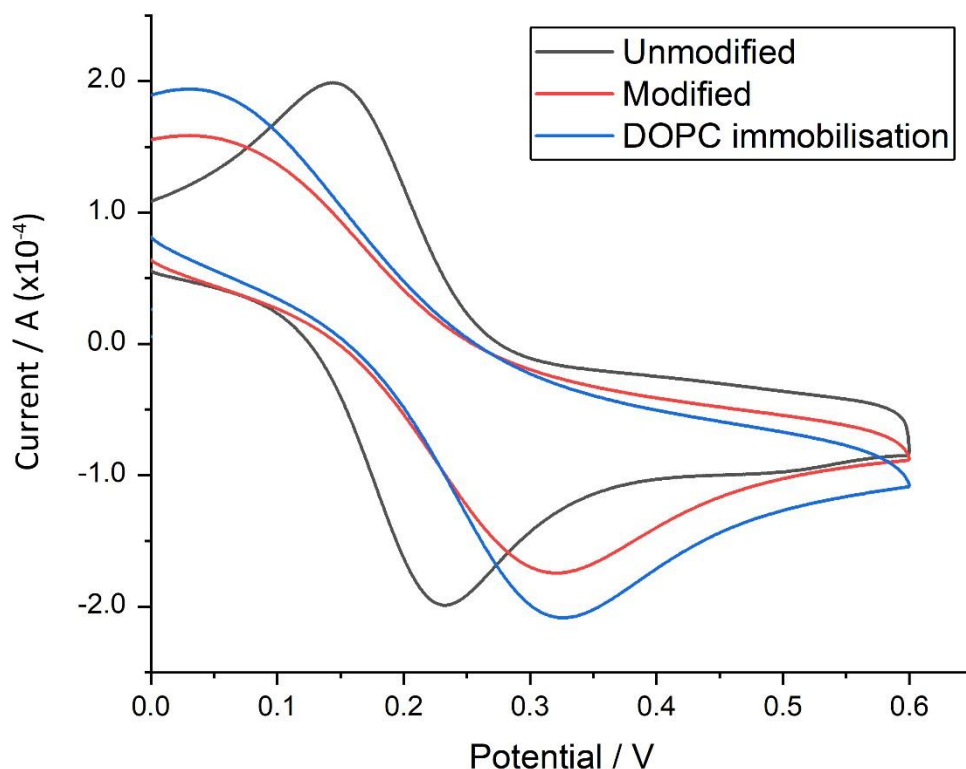


Figure 2.19: CVs of a PS lithography microcavity array treated with 10 mM

6-mercapto-1-hexanol on the top surface supporting a DOPC bilayer using LB followed by vesicle fusion on a PS lithographically prepared pre-aqueous filled microcavity array platform. The grey voltammogram is the unmodified array, red voltammogram is of the functionalised with 6-mercapto-1-hexanol using a 30 min μ CP time with 0.6 Pa pressure and blue is the support of the DOPC lipid membrane. All electrodes were measured in triplicate using a standard 3 electrode set up in using 10 mM potassium ferricyanide in 1 M KCl as the supporting electrolyte and measured from 0 to 0.6 V (vs. Ag/AgCl) at a scan rate of 100 mV/s.

In figure 2.20 after functionalisation using 10 mM hydroxyl terminated PEG thiol, the redox signal can no longer be seen. This loss in redox signal seen in the voltammogram signifies a “blocking effect” of the modified surface, which indicates a slowdown of the electron transfer at the electrode surface. The change in position of the anodic peak of 0.255 V from the unmodified array to 0.368 V following the functionalisation of the array is more significant to that of figure 2.20. Furthermore, after the addition of a DOPC membrane onto the array surface, there is a suppression of the redox signal of the probe which indicates a continuous well packed membrane which effectively inhibits the permeation of ions to the underlying surface.

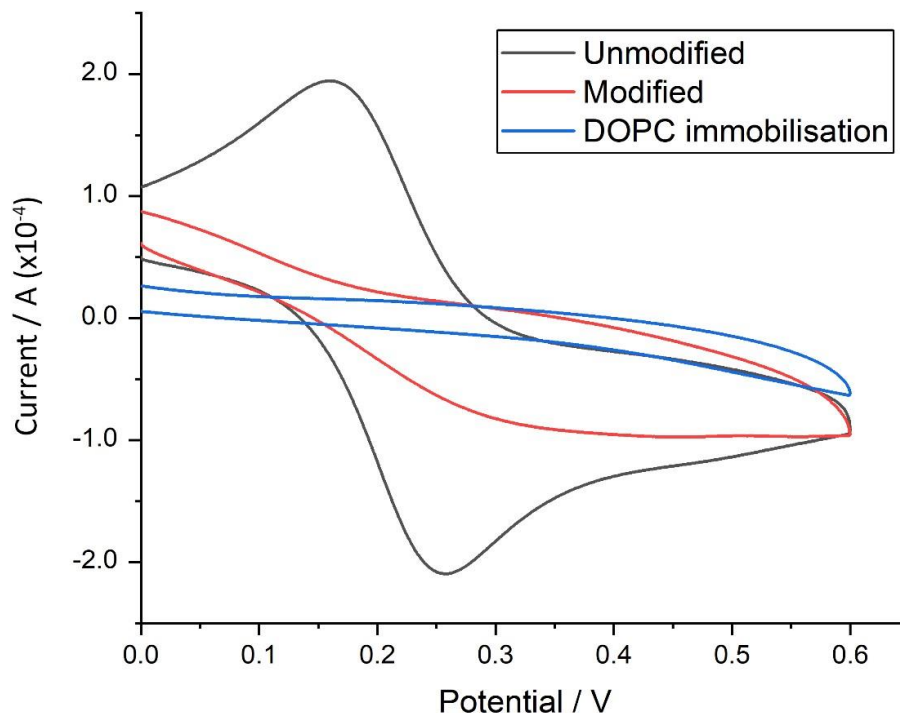


Figure 2.20: CVs of PS lithography microcavity array treated with 10 mM hydroxyl terminated PEG thiol on the top surface supporting a DOPC bilayer using LB followed by vesicle fusion on a PS lithographically prepared pre-aqueous filled microcavity array platform. The grey voltammogram is the unmodified array, red voltammogram is of the array functionalised with hydroxyl terminated PEG thiol using a 30 min μ CP time with 0.6 Pa pressure and blue is the support of the DOPC lipid membrane. All electrodes were measured in triplicate using a standard 3 electrode set up in using 10 mM potassium ferricyanide in 1 M KCl as the supporting electrolyte and measured from 0 to 0.6 V (vs. Ag/AgCl) at a scan rate of 100 mV/s.

In figure 2.21, after the functionalisation of carboxylate termini thiol; 6-mercaptohexanoic acid onto the array surface, there is a shift in the anodic peak from 0.254 V to 0.406 V for the functionalised array. The probe's redox signal was further suppressed, as predicted, after the assembly of a DOPC membrane onto the array surface, with the anodic peak shifting to 0.45 V.

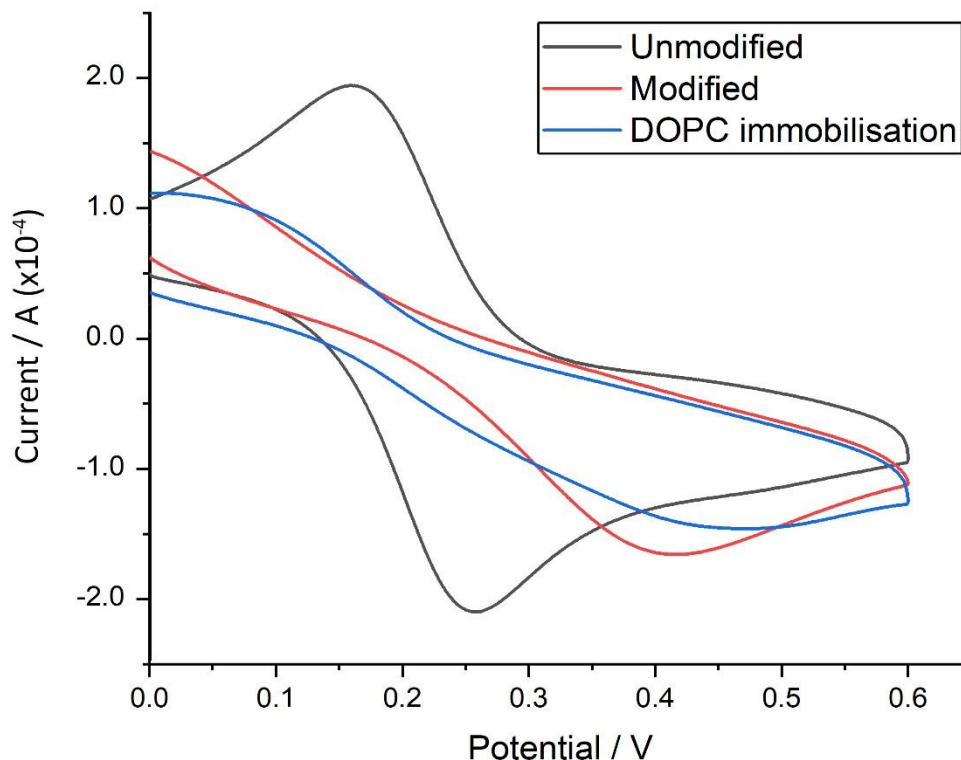


Figure 2.21: CVs of a PS lithography microcavity array treated with 10 mM 6-mercaptohexanoic acid on the top surface supporting a DOPC bilayer using LB followed by vesicle fusion on a PS lithographically prepared pre-aqueous filled microcavity array platform.

The grey voltammogram is the unmodified array, red voltammogram is of the array functionalised with 6-mercaptohexanoic acid using a 30 min μ CP time with 0.6 Pa pressure and blue is the support of the DOPC lipid membrane. All electrodes were measured in triplicate using a standard 3 electrode set up in using 10 mM potassium ferricyanide in 1 M KCl as the supporting electrolyte and measured from 0 to 0.6 V (vs. Ag/AgCl) at a scan rate of 100 mV/s.

Interestingly, for the modified electrodes the hydroxyl terminated PEG thiol supporting a DOPC membrane was able to suppress ferricyanide access to the electrode to a greater degree than 6-mercapto-1-hexanol and 6-mercaptohexanoic acid. These results demonstrate that the DOPC membrane is well distributed on hydroxyl terminated PEG thiols, allowing for a continuous well packed layer which effectively inhibits the permeation of ions to the underlying gold surface.

2.3 Conclusions

Chapter 2 examined the use of SAM functionalised 1.83 μm PS sphere lithography microcavity arrays to support lipid bilayers where the SAM was prepared using a new μCP method to selectively modify the top surface. A comparison was made between the solution deposition and the μCP method in functionalising gold surfaces was explored. Cyclic voltammetry was used to assess the functionalisation of the array on SAM formation at different time pressure intervals in an effort to optimise μCP parameters.

Aqueous filled microcavity supported lipid membranes were prepared at uniform 1.83 μm microcavity arrays and their surface coverage was assessed using CV. The magnitude of the surface coverage of the DOPC bilayer on PEG thiol was much greater than that of 6-mercapto-1-hexanol and 6-mercaptohexanoic acid. EIS stability experiments show that DOPC membranes supported by the hydroxyl terminus PEG thiol to have greater stability but a smaller change in membrane resistance in comparison to 6-mercapto-1-hexanol and 6-mercaptohexanoic acid. All the SAMs used in this chapter will be used in chapter 3.

2.4 References

- (1) Dufourc, E. J. Sterols and Membrane Dynamics. *J. Chem. Biol.* **2008**, *1* (1–4), 63–77. <https://doi.org/10.1007/s12154-008-0010-6>.
- (2) Arotiba, O. A.; Baker, P. G.; Mamba, B. B.; Iwuoha, E. I. The Application of Electrodeposited Poly(Propylene Imine) Dendrimer as an Immobilisation Layer in a Simple Electrochemical DNA Biosensor. *Int. J. Electrochem. Sci.* **2011**, *6* (3). <https://doi.org/10.3390/s8116791>
- (3) Berselli, G. B.; Sarangi, N. K.; Gimenez, A. V.; Murphy, P. V.; Keyes, T. E. Microcavity Array Supported Lipid Bilayer Models of Ganglioside – Influenza Hemagglutinin1 Binding. *Chem. Commun.* **2020**, *56* (76), 11251–11254. <https://doi.org/10.1039/D0CC04276E>.
- (4) Velázquez, M. M.; Alejo, T.; López-Díaz, D.; Martín-García, B.; Dolores Merchán, M. Langmuir-Blodgett Methodology: A Versatile Technique to Build 2D Material Films; **2016**. <https://doi.org/10.5772/63495>
- (5) Sarangi, N. K.; Prabhakaran, A.; Keyes, T. E. Interaction of Miltefosine with Microcavity Supported Lipid Membrane: Biophysical Insights from Electrochemical Impedance Spectroscopy. *Electroanalysis* **2020**, *32* (12). <https://doi.org/10.1002/elan.202060424>.
- (6) Bartlett, P. N.; Baumberg, J. J.; Birkin, P. R.; Ghanem, M. A.; Netti, M. C. Highly Ordered Macroporous Gold and Platinum Films Formed by Electrochemical Deposition through Templates Assembled from Submicron Diameter Monodisperse Polystyrene Spheres. *Chem. Mater.* **2002**, *14* (5), 2199–2208. <https://doi.org/10.1021/cm011272j>.
- (7) Baca, A. J.; Truong, T. T.; Cambrea, L. R.; Montgomery, J. M.; Gray, S. K.; Abdula, D.; Banks, T. R.; Yao, J.; Nuzzo, R. G.; Rogers, J. A. Molded Plasmonic Crystals for Detecting and Spatially Imaging Surface Bound Species by Surface-Enhanced Raman Scattering. *Appl. Phys. Lett.* **2009**, *94* (24), 243109. <https://doi.org/10.1063/1.3155198>.

- (8) Abu Hatab, N. A.; Oran, J. M.; Sepaniak, M. J. Surface-Enhanced Raman Spectroscopy Substrates Created via Electron Beam Lithography and Nanotransfer Printing. *ACS Nano* **2008**, *2* (2), 377–385. <https://doi.org/10.1021/nn7003487>.
- (9) Yue, W.; Wang, Z.; Yang, Y.; Chen, L.; Syed, A.; Wong, K.; Wang, X. Electron-Beam Lithography of Gold Nanostructures for Surface-Enhanced Raman Scattering. *J. Micromech. Microeng.* **2012**, *22*, 125007. <https://doi.org/10.1088/0960-1317/22/12/125007>.
- (10) Brolo, A. G.; Gordon, R.; Leathem, B.; Kavanagh, K. L. Surface Plasmon Sensor Based on the Enhanced Light Transmission through Arrays of Nanoholes in Gold Films. *Langmuir* **2004**, *20* (12), 4813–4815. <https://doi.org/10.1021/la0493621>.
- (11) Jose, B.; Mallon, C. T.; Forster, R. J.; Blackledge, C.; Keyes, T. E. Lipid Bilayer Assembly at a Gold Nanocavity Array. *Chem. Commun.* **2011**, No. 46, 12530–12532. <https://doi.org/10.1039/C1CC15709D>.
- (12) Berselli, G. B.; Sarangi, N. K.; Ramadurai, S.; Murphy, P. V.; Keyes, T. E. Microcavity-Supported Lipid Membranes: Versatile Platforms for Building Asymmetric Lipid Bilayers and for Protein Recognition *Appl. Bio Mater.* **2019**, *2* (8), 3404–3417. <https://doi.org/10.1021/acsabm.9b00378>.
- (13) Sarangi, N. K.; Prabhakaran, A.; Keyes, T. E. Interaction of Miltefosine with Microcavity Supported Lipid Membrane: Biophysical Insights from Electrochemical Impedance Spectroscopy. *Electroanalysis* **2020**, *32* (12), 2936–2945. <https://doi.org/10.1002/elan.202060424>.

- (14) Khursheed, A. Scanning Electron Microscope Optics and Spectrometers <https://www.worldscientific.com/worldscibooks/10.1142/7094> (accessed 2020 -12 -26).
- (15) Elgrishi, N.; Rountree, K. J.; McCarthy, B. D.; Rountree, E. S.; Eisenhart, T. T.; Dempsey, J. L. A Practical Beginner's Guide to Cyclic Voltammetry. *J. Chem. Educ.* **2018**, *95* (2), 197–206. <https://doi.org/10.1021/acs.jchemed.7b00361>.
- (16) El-Beyrouthy, J.; Freeman, E. Characterizing the Structure and Interactions of Model Lipid Membranes Using Electrophysiology. *Membranes* **2021**, *11* (5), 319. <https://doi.org/10.3390/membranes11050319>.
- (17) Markov, M. S. Electric and Magnetic Fields Bioeffects. In *Encyclopedia of Applied Electrochemistry*; Kreysa, G., Ota, K., Savinell, R. F., Eds.; Springer: New York, NY, 2014; pp 379–384. https://doi.org/10.1007/978-1-4419-6996-5_261.
- (18) Hosen, M. S.; Gopalakrishnan, R.; Kalogiannis, T.; Jaguemont, J.; Van Mierlo, J.; Berecibar, M. *Impact of Relaxation Time on Electrochemical Impedance Spectroscopy Characterization of the Most Common Lithium Battery Technologies – Experimental Study and Chemistry-Neutral Modeling*; SSRN Scholarly Paper ID 3778330; Social Science Research Network: Rochester, NY, 2021. <https://doi.org/10.2139/ssrn.3778330>.
- (19) Römer, W.; Steinem, C. Impedance Analysis and Single-Channel Recordings on Nano-Black Lipid Membranes Based on Porous Alumina. *Biophys. J.* **2004**, *86* (2), 955–965.
- (20) Basit, H.; Van der Heyden, A.; Gondran, C.; Nysten, B.; Dumy, P.; Labbé, P. Tethered Bilayer Lipid Membranes on Mixed Self-Assembled Monolayers of a Novel Anchoring Thiol: Impact of the Anchoring Thiol Density on Bilayer Formation. *Langmuir* **2011**, *27* (23), 14317–14328. <https://doi.org/10.1021/la202847r>.

- (21) Schmitt, E. K.; Nurnabi, M.; Bushby, R. J.; Steinem, C. Electrically Insulating Pore-Suspending Membranes on Highly Ordered Porous Alumina Obtained from Vesicle Spreading. *Soft Matter* **2008**, *4* (2), 250–253. <https://doi.org/10.1039/B716723G>.
- (22) Wiegand, G.; Arribas-Layton, N.; Hillebrandt, H.; Sackmann, E.; Wagner, P. Electrical Properties of Supported Lipid Bilayer Membranes. *J. Phys. Chem. B* **2002**, *106* (16), 4245–4254. <https://doi.org/10.1021/jp014337e>.
- (23) Hussain, S. A.; Dey, B.; Bhattacharjee, D.; Mehta, N. Unique Supramolecular Assembly through Langmuir – Blodgett (LB) Technique. *Heliyon* **2018**, *4* (12), e01038. <https://doi.org/10.1016/j.heliyon.2018.e01038>.
- (24) Langmuir & Langmuir Blodgett | Measurements <https://www.biolinscientific.com/measurements/langmuir-and-langmuir-blodgett> (accessed 2021 -01 -26).
- (25) Langmuir Films. *Nanoscience Instruments*.
- (26) Hovis, J. S.; Boxer, S. G. Patterning and Composition Arrays of Supported Lipid Bilayers by Microcontact Printing. *Langmuir* **2001**, *17* (11), 3400–3405. <https://doi.org/10.1021/la0017577>.
- (27) Kung, L. A.; Kam, L.; Hovis, J. S.; Boxer, S. G. Patterning Hybrid Surfaces of Proteins and Supported Lipid Bilayers. *Langmuir* **2000**, *16* (17), 6773–6776. <https://doi.org/10.1021/la000653t>.
- (28) Mirley, C. L.; Koberstein, J. T. A Room Temperature Method for the Preparation of Ultrathin SiO_x Films from Langmuir-Blodgett Layers. *Langmuir* **1995**, *11* (4), 1049–1052. <https://doi.org/10.1021/la00004a001>.

- (29) Madzharova, F.; Heiner, Z.; Kneipp, J. Surface-Enhanced Hyper Raman Spectra of Aromatic Thiols on Gold and Silver Nanoparticles. *J. Phys. Chem. C* **2020**, *124* (11), 6233–6241. <https://doi.org/10.1021/acs.jpcc.0c00294>.
- (30) Maher, S.; Basit, H.; Forster, R. J.; Keyes, T. E. Micron Dimensioned Cavity Array Supported Lipid Bilayers for the Electrochemical Investigation of Ionophore Activity. *Bioelectrochemistry* **2016**, *112*, 16–23. <https://doi.org/10.1016/j.bioelechem.2016.07.002>.
- (31) Kresák, S.; Hianik, T.; Naumann, R. L. C. Giga-Seal Solvent-Free Bilayer Lipid Membranes: From Single Nanopores to Nanopore Arrays. *Soft Matter* **2009**, *5* (20), 4021–4032. <https://doi.org/10.1039/B907661A>.
- (32) Losic, D.; Shapter, J. G.; Gooding, J. J. Influence of Surface Topography on Alkanethiol SAMs Assembled from Solution and by Microcontact Printing. *Langmuir* **2001**, *11* (17), 3307–3316.
- (33) Porter, M. D.; Bright, T. B.; Allara, D. L.; Chidsey, C. E. D. Spontaneously Organized Molecular Assemblies. 4. Structural Characterization of n-Alkyl Thiol Monolayers on Gold by Optical Ellipsometry, Infrared Spectroscopy, and Electrochemistry. *J. Am. Chem. Soc.* **1987**, *109* (12), 3559–3568. <https://doi.org/10.1021/ja00246a011>.

**Chapter 3: The impact SAM on Bilayer
formation and stability at two-photon
polymerised prepared microcavity
arrays**

3.0 Introduction

In this chapter, we explore the prospect of using microfabrication instruments for the manufacture of microcavity arrays. The microfabrication process produces structures which can be fabricated within the substrate of a material or on the surface of the substrate through micromachining.^{1,2} This is an easy, reproducible and low cost means of fabricating pore arrays that eliminates the need for extensive user skill required for PS sphere templating.³ To date the devices have been made and characterised but it has not been established that they can support a bilayer in analogous fashion to PS sphere templated microcavity arrays. The focus of this chapter is to establish if bilayer assembly occurs and evaluate suitable surface chemistry modification method and to assess the stability of the bilayer in comparison to lithographically prepared arrays.

Here using the same approach to chapter 2, microcontact printing (μ CP) is used to functionalise a two-photon polymerised microcavity array platforms manufactured by photolithography, allowing the formation of alkanethiols SAMs on the gold sputter coated fabricated array. Specifically, 6-mercapto-1-hexanol, hydroxyl terminated PEG thiol and 6-mercaptopentanoic acid were used as SAMs. The differing functional group endings of these SAMs were used to support lipid bilayers and their overall stability on the platform was assessed by Electrochemical impedance spectroscopy (EIS), Raman spectroscopy and cyclic voltammetry (CV) were employed for characterisation purposes.

3.1 Methods and methods

3.1.1 Materials

Ostemer 322 was purchased from Mercene Labs AB, Stockholm, Sweden.

The rest of the materials are as described in section 2.2.1

3.1.2 Methods

3.1.2.1 Fabrication of two-photon polymerisation cavity arrays

Nanoscribe Photonic Professional GT employs direct laser writing (DLW) two-photon polymerisation to a UV-Curable photoresist to fabricate structures in the sub micrometre range. The instrument has two writing modes which moves the laser focus with respect to the photoresist. A galvo-mode for an ultra-fast layer-by-layer process and a piezo-mode for arbitrary 3D trajectories. As seen in figure 3.1, the instrument combines an inverted optical microscope, high speed galvo mirror laser scanner, a femtosecond laser and a high precision piezo-stage.

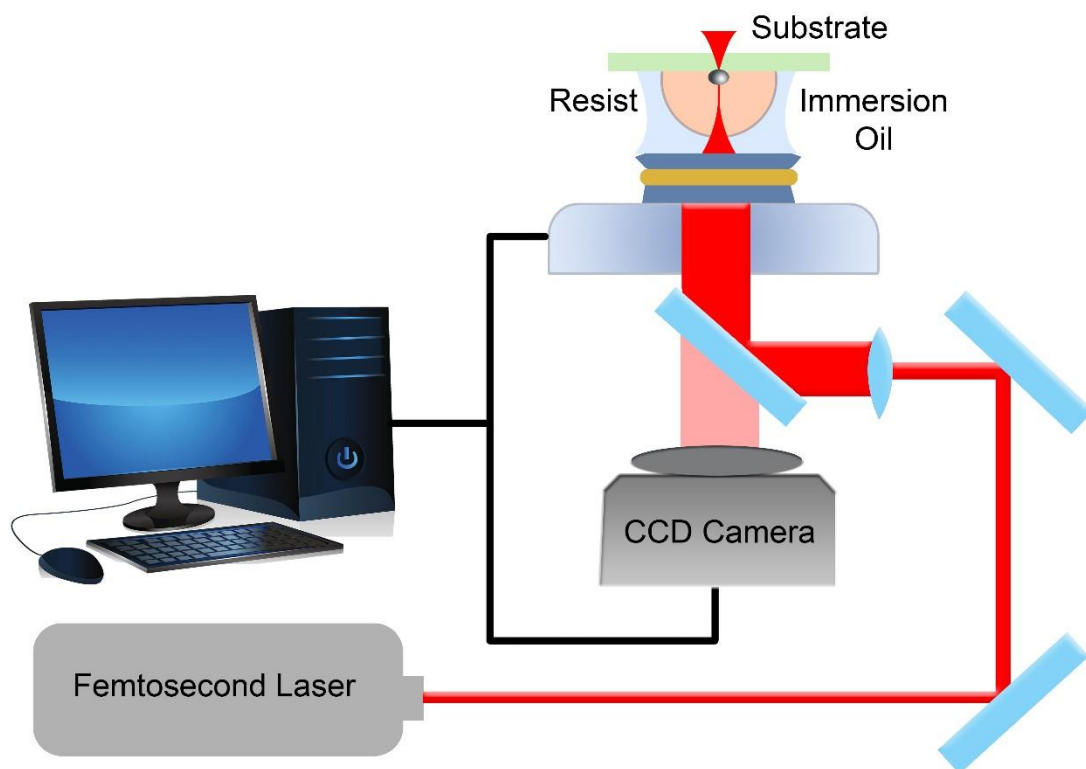


Figure 3.1: Schematic representation of how a two-photon lithography nanoscribe.

As described by Šakalys et al. cavities of interest of significant width and depth were developed on a solid works software.⁴ A 63x objective lens was used to polymerise DLL reagent on a photoresist glass slide. The array was developed in Propylene glycol monomethyl ether acetate (PGMEA) solution for 25 min to dissolve the unexposed photoresist. The structure was developed in NOVEC solution for 2 min to wash out residual PGMEA.

As shown in figure 3.2, the slide was placed onto a primary template mould and covered with PDMS at a ratio of 10:1 and was desiccated overnight prior to overnight thermal curing at 100 °C. A secondary mould was removed from the primary PDMS template and was thermally treated at 100 °C overnight. After the overnight curing, Ostemer 322 was mixed at a ratio 521:479 and was desiccated for 1 hr. Following desiccation the Ostemer 322 was then placed onto the secondary mould and was further desiccated.^{3,4,5,6,7} The template was treated for 30 mins at 365 nm, the semi cured Ostemer 322 was removed from the mould, followed by 90 nm thickness of gold was sputter coated using an Cressington automatic coater onto the array. Post coating the arrays were thermally cured for 2 days at room temperature.

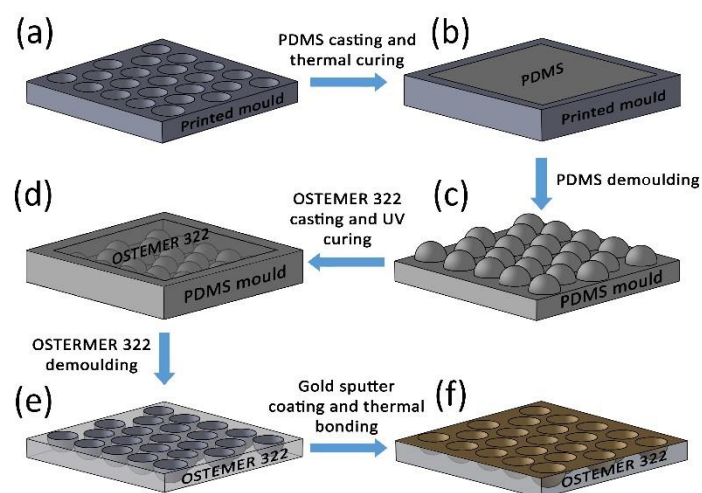


Figure 3.2: A schematic representation of how two-photon polymerisation microcavity arrays platforms are prepared. (a) The DLL was photo treated to form cavities on a glass slide containing photoresist. (b) The glass slide with the cavities present was cured on a first primary template and was treated thermally overnight. (c) Ostemer 322 ratio of 521:479 was mixed and desiccated for 1hr before being added to the primary mould. The mould was desiccated for 2 hrs at room temperature. (d) The mould was UV treated using a 365 nm lamp for 30 mins. (e) The substrates were removed from the master mould. (f) The chips were sputter coated with 90 nm of gold. (g) The chips were then thermally cured for 2 days at room temperature Schematic representation courtesy of Dr. Rokas Šakalys.

3.1.2.2 Simulations

All simulations in figure 3.4 were performed with a resolution of 8 nm and the conformal variant 2 was used as the mesh refinement method. Simulations were carried out for cavities both with and without nanostructures, where the illuminator laser bandwidth was set at 0.02 nm and a central wavelength of 785 nm. All simulations were completed with a zero degree angle on the laser.

Further experimental procedures and equipment carried out as per chapter 2, section 2.

3.2 Results and Discussion

3.2.1 Optimisation of cavity for SERs

Numerical simulations were carried out by Dr Kho Kiang, (Keyes research group, DCU) using Lumerical finite different time domain (FDTD) solutions software to model the optical properties of the cavities. This was done to evaluate the regions of highest electric field enhancement. As seen from figure 3.4, the size, shape, depth and the nanostructure within the cavities have a great influence on the plasmonic enhancement observed.^{5,8,9,10}

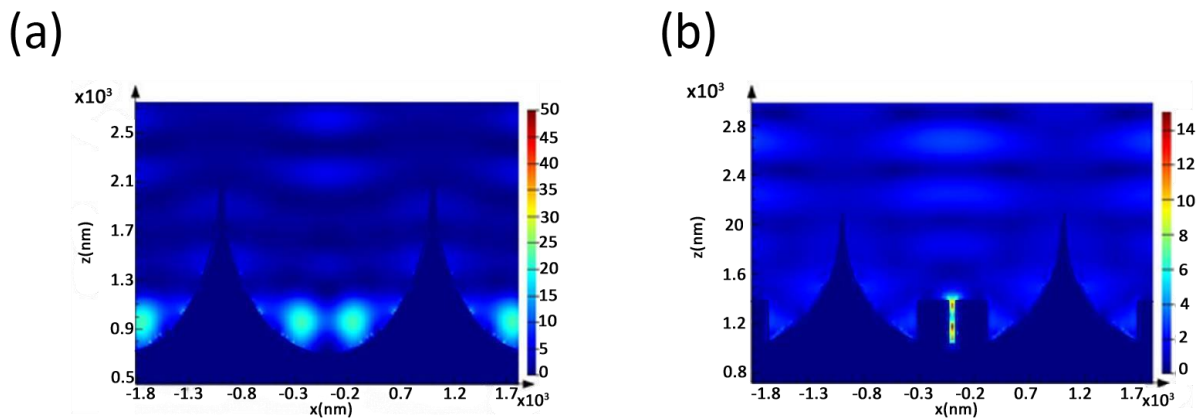
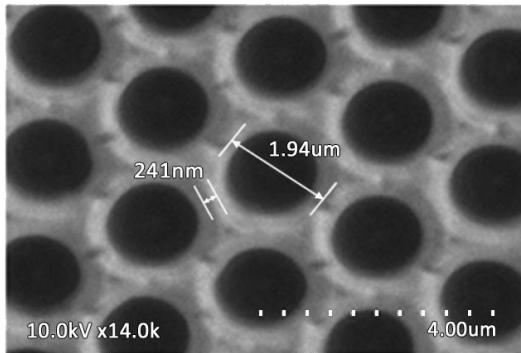


Figure 3.4: Simulations of 2 μm cavities at 785 nm. a) Simulation of a cavity with no nanostructures. b) Simulation of a cavity with nanostructures present. Carried out by Dr. Kho Kiang.

Figure 3.4 shows the FDTD simulation at an excitation wavelength of 785nm that was consistent with the previous work carried out by Bartlett et al. and Šakalys et al.^{2,5}

Using the cavity and nanostructure dimensions from the simulations, both arrays with and without nanostructures were fabricated. Figure 3.5 shows scanning electron microscopy (SEM) images of (a) a top view of microcavity arrays and (b) a side view of a singular microcavity array following fabrication.

(a)



(b)

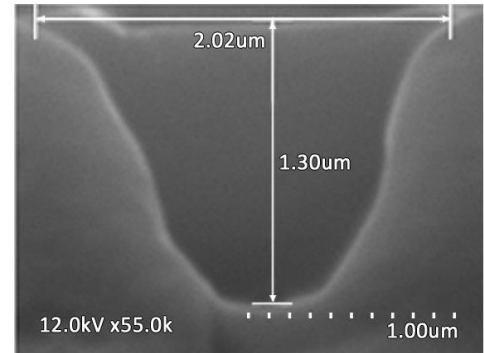
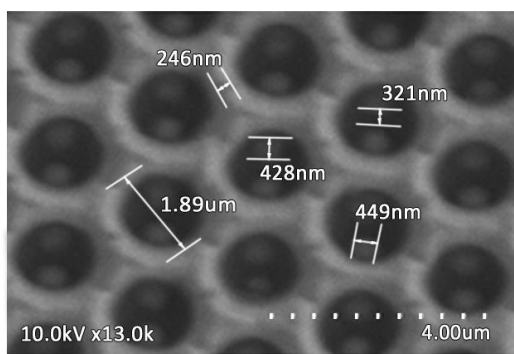


Figure 3.5: SEM images of microcavity array. (a) Top view (b) Side view of cavity pore.

Courtesy of Dr. Rokas Šakalys.

Figure 3.6 shows SEM images of (a) a top view of microcavity arrays and (b) a side view of a singular microcavity array following fabrication containing nanostructures present. The fact that these arrays have near identical measurements from SEM, demonstrates the reproducibility of the platform.

(a)



(b)

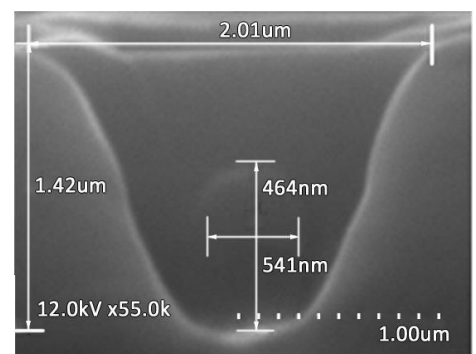


Figure 3.6: SEM images of microcavity array with nanostructures present. a) Top view with nanostructures present b) Side view of cavity pore with nanostructures present. Courtesy of

Dr. Rokas Šakalys.

To validate the data received from the simulations Raman spectras of DRAQ7 sonicated in cavities both with and without nanostructures as per figure 3.7 were collected by Dr. Rokas Šakalys. The concentration of the probe was identical in both cases. The orange spectra is of DRAQ7 in a cavity with no nanostructures present and the black spectra is of DRAQ7 which shows a significant increase in intensity in cavities with nanostructures.

This confirms that the plasmonic field, is greater inside the nanostructured arrays, consistent with simulation, indicating that the SERS enhancement is greater.

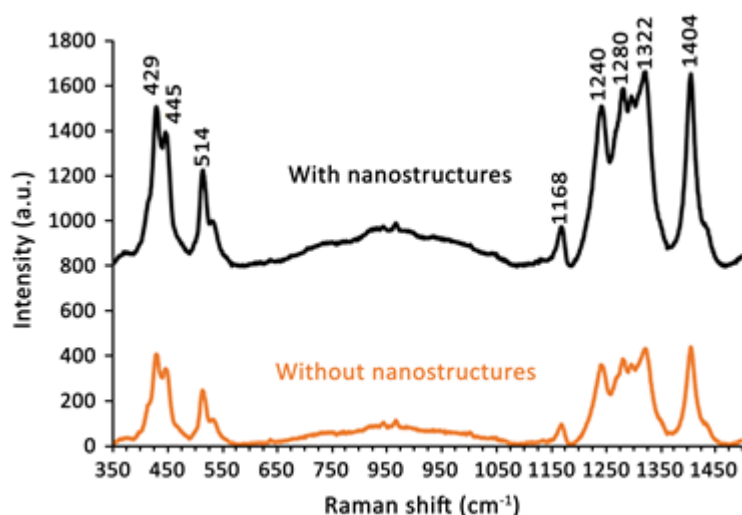


Figure 3.7: Raman spectra of 5 μM DRAQ7 sonicated in 2 μM two-photon polymerised microcavity array both with and without nanostructure using 785 nm excitation line at an incident laser power of 2.4 mW. The orange spectra is of unmodified cavities and where black is of cavities with nanostructure present. Courtesy of Dr. Rokas Šakalys

3.2.2 Characterisation and functionalisation of two-photon polymerised microcavity array

The microfabricated gold microcavities were characterised using SEM to ensure consistency in pore structure and packing as seen in figure 3.8. The 2 μm gold cavity arrays were fabricated using the master templated method as described in section 3.1.2.1. The images show that the two-photon polymerised method produced well-ordered compact arrays. This approach uses a combination of 3D printing and soft lithography methods which produces reproducible platforms of a submicron resolution unlike polystyrene lithography arrays which requires intensive user skill due to risk in forming defected regions through multilayers or discontinuity of sphere packing.

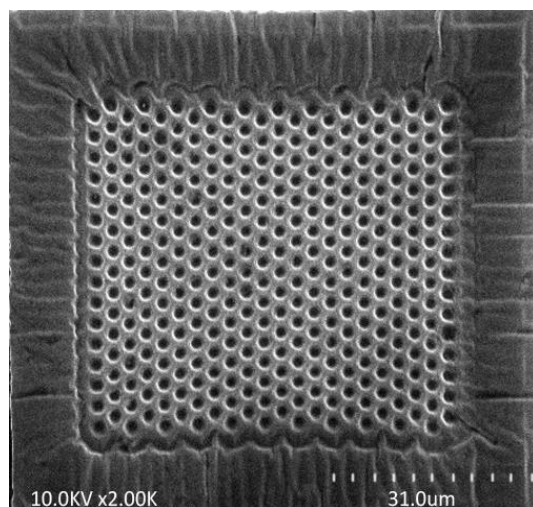


Figure 3.8: SEM image of the microcavity array platform.

3.1.2.1 Optimisation of microcontact printing parameters

The modification of the top surface of the microfabricated pore array was carried out in a similar way to that described for the polystyrene sphere lithography arrays in chapter 2. The microcontact printing (μCP) parameters were optimised through cyclic voltammograms of the array functionalised at different time intervals followed by different pressure intervals were used to evaluate SAM formation via surface blocking.

In figure 3.9, a PDMS template was functionalised as per section 2.1.2.3 were 10 mM 6-mercapto-1-hexanol was in contact with the microcavity array for 15 min, 30 min and 24 hr time periods followed by characterisation through CV. The ΔE of an unmodified array was 0.1 V however, after μ CP for 15min, 30 min and 24 hr contact printing, in the voltammograms there was an shift in the anode peak area was measured at 0.304 V for 15 min, 0.326 V for 30 min and 0.338 V for 24 hr. As there was little difference in the anodic peak between 30 min and 24 hr voltammogram, the 30 min μ CP was used as the parameter to find the pressure to apply for optimum surface coverage.

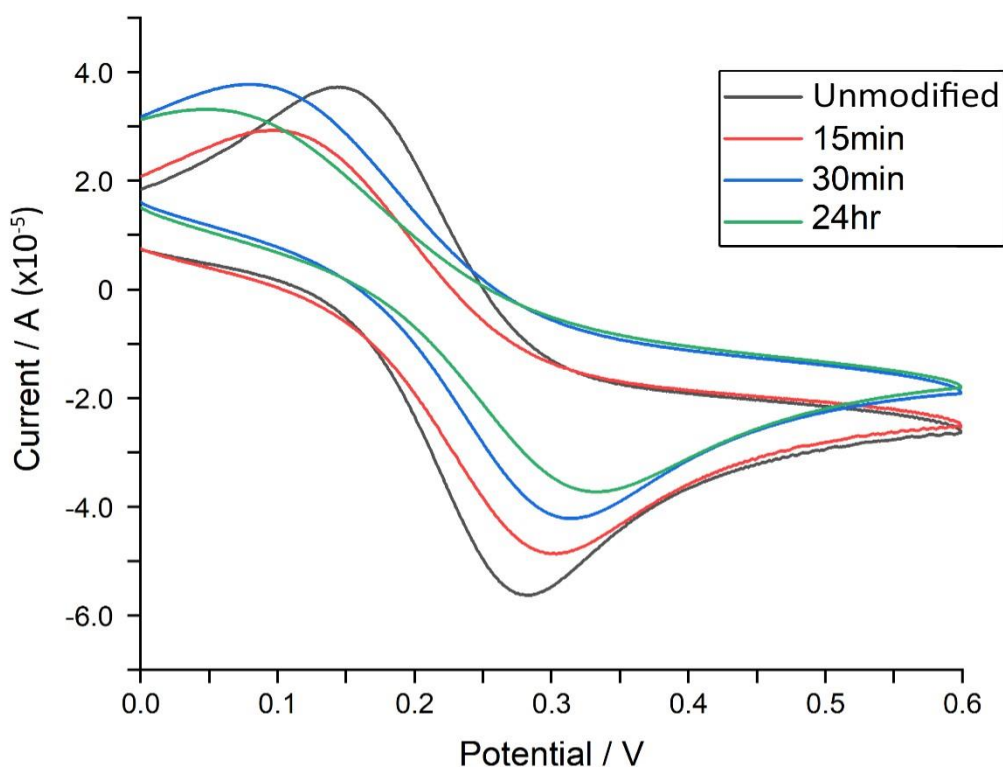


Figure 3.9: Comparison of voltammetry of two-photon polymerised microcavities platform at different μ CP time intervals of 10 mM 6-mercapto-1-hexanol using cyclic voltammetry.

Where the grey is no an unmodified array, red is coverage after 15 min μ CP, blue is coverage after 30 min μ CP and green is coverage after 24 hr μ CP. All electrodes were measured using a standard 3 electrode set up in using 10 mM potassium ferricyanide in 1 M KCl as the supporting electrolyte and measured from 0 to 0.6 V (vs. Ag/AgCl) at a scan rate of 100 mV/s.

Using the 30 min as the fixed time for the μ CP, the voltammograms of the arrays modified using 30 min under different applied pressures ranging from 0 Pa to 1.8 Pa are shown in figure 3.10. The peak to peak separation of the functionalised array with 30 min μ CP with no pressure was 0.317 V, which is similar to that of figure 3.9. However, after 30 min μ CP with a pressure of 0.6 Pa, a significant increase in surface coverage was intimated as the shift in the anodic peak potential to 0.328 V.

There was very little change seen in the surface coverage of the modified array after 30 min with 0.9 Pa μ CP and 1.8 Pa voltammograms with the shift of the anodic peak from 0.328 V to and 0.341 V. The small changes in surface coverage with increasing pressure between 0.6 Pa and 1.8 Pa suggest a plateau in surface coverage has been reached and consequently that 0.6 Pa being deemed the optimum pressure from this study.

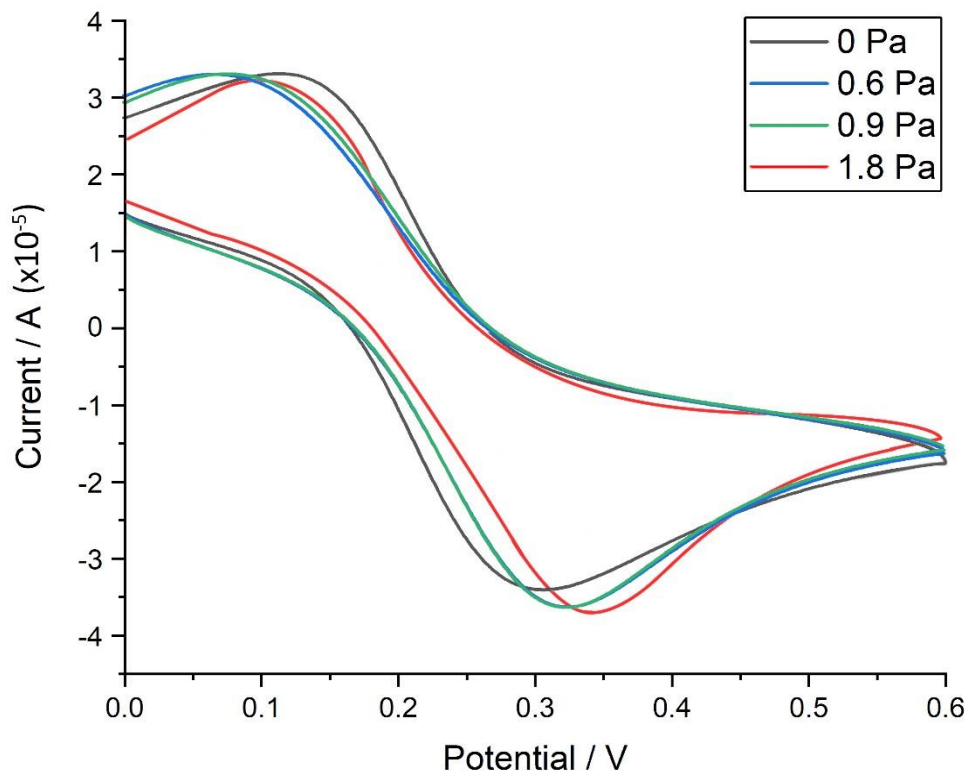


Figure 3.11: Comparison of voltammetry of two-photon polymerised microcavities platform at different μ CP pressure intervals of 10 mM 6-mercapto-1-hexanol using cyclic voltammetry. Where the grey is the CV of 30 min contact with no pressure, blue CV is of 30 min contact with 0.6 Pa, green CV is 30 min contact with 0.9 Pa, and red CV is of 30 min contact with 1.8 Pa. All electrodes were measured using a standard 3 electrode set up in using 10 mM potassium ferricyanide in 1 M KCl as the supporting electrolyte and measured from 0 to 0.6 V (vs. Ag/AgCl) at a scan rate of 100 mV/s.

3.2.3 Electrochemical Impedance Spectroscopy of Lipid membrane on a printed array

Figure 3.11 shows EIS of an unmodified two-photon polymerised array that was functionalised by μ CP in 10 mM 6-mercapto-1-hexanol for 30 min under 0.6 Pa of pressure which causes an increase in the resistance of the array. It is seen with the addition of a bilayer onto the array through the Langmuir-Blodgett method followed by vesical fusion.

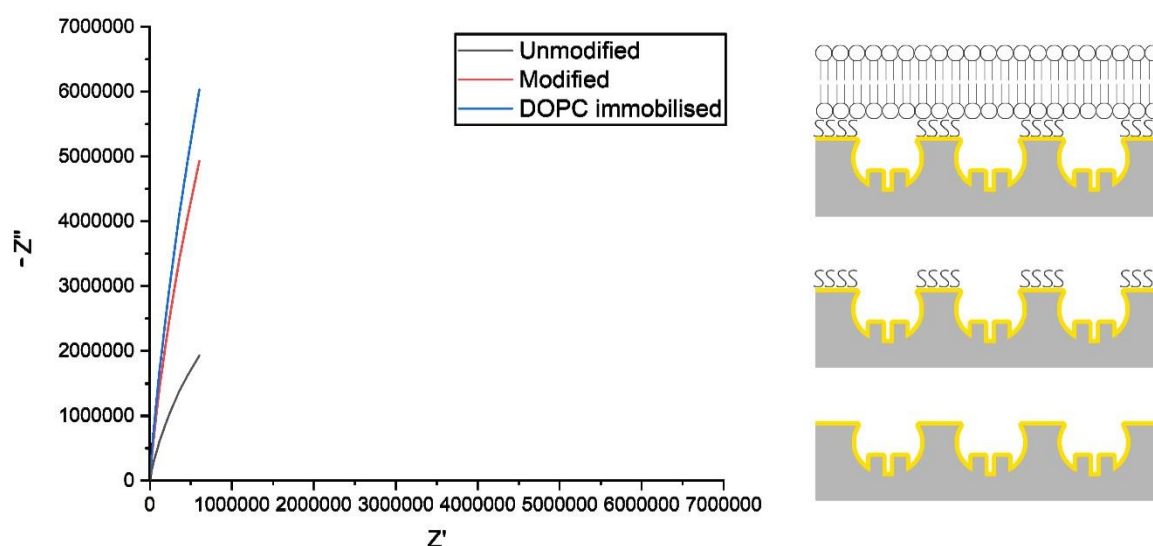


Figure 3.11: Electrochemical impedance spectroscopy Nyquist plot of the fabrication steps for MSLB, using LB followed by vesicle fusion on a two-photon polymerised microcavity array modified with 10 mM 6-mercapto-1-hexanol. Grey represents unfunctionalised microcavity array red represents the microcavity array functionalised in 1-mercapto-6-hexanol where blue presents the microcavity array supporting a DOPC bilayer. All measurements were measured in triplicate and conducted using a 30 min μ CP time with 0.6 Pa pressure in PBS buffer at pH 7.4 within the experimental window of 20 hrs. A standard 3-electrode system at 0 V (vs Ag/AgCl) using an AC amplitude of 0.01 V with a frequency range of 1 MHz to 0.01 Hz.

EIS was carried out to confirm the formation and stability of lipid membranes on three separate SAMs using three separate electrodes. EIS can be used to establish the formation of bilayers by measuring the resistance variation over time.^{11,12,13} If the bilayer film was to be unstable this would cause a change in the film resistance.

Representative EIS data are shown in figure 3.13 on DOPC supported 10 mM 6-mercapto-1-hexanol on MSLB (a) below, the membrane resistance of the DOPC symmetric bilayer was found to be stable for 8 hrs. The data in (b) figure 3.13 indicates that the impedance response of the SAM significantly changes after μ CP but with very little change after 60 min.

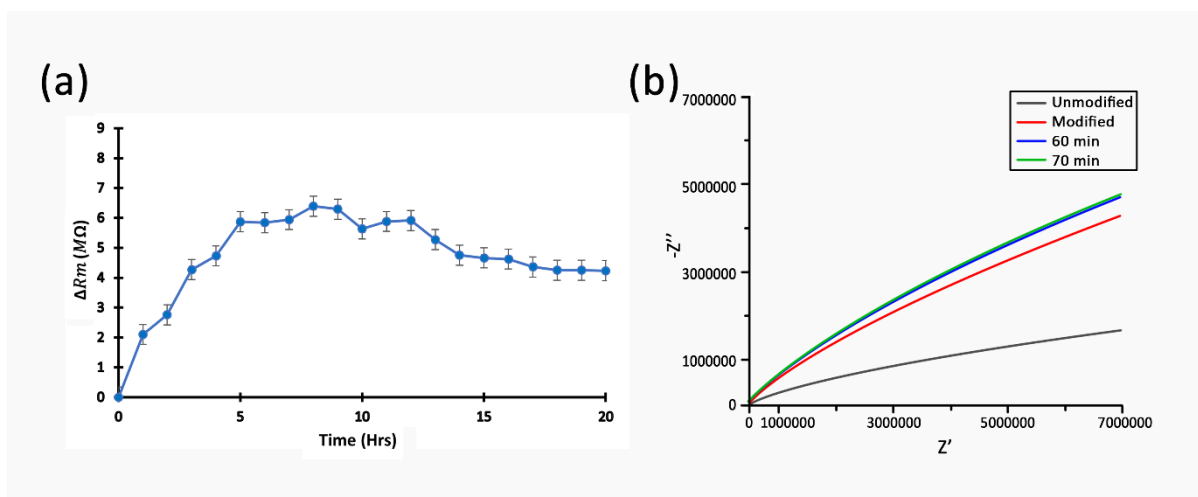


Figure 3.13: The relative change in resistance of a DOPC bilayer prepared using LB followed by vesicle fusion on a two-photon polymerised microcavities platform pre-aqueous filled microcavity array platform modified using 10 mM 6-mercapto-1-hexanol. (b) Nyquist plot of this substrate, unfunctionalised (grey), post after functionalisation (red), 60 min post modification (blue) 70 min post modification (green). All measurements were conducted using a 30 min μ CP time with 0.6 Pa pressure in PBS buffer at pH 7.4 within the experimental window of 20 hrs. A standard 3-electrode system at 0 V (vs Ag/AgCl) using an AC amplitude of 0.01 V with a frequency range of 1 MHz to 0.01 Hz.

The arrays functionalised using 10 mM hydroxyl terminated PEG thiol to support a DOPC membrane were next examined by EIS. As shown in the figure 3.14 below, the membrane resistance of the DOPC symmetric bilayer was found to be stable for 8 hrs. In comparison to DOPC membrane stability using 6-mercapto-1-hexanol, the relative change in membrane resistance is similar to that of membrane stability using hydroxyl terminated PEG thiol.

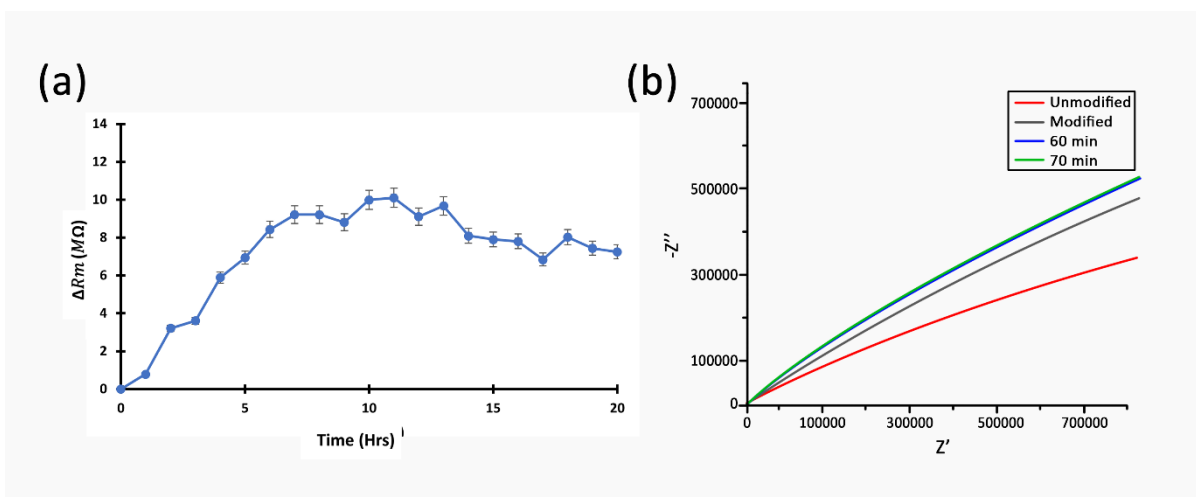


Figure 3.14: The relative change in resistance of a DOPC bilayer prepared using LB followed by vesicle fusion on a two-photon polymerised microcavities platform pre-aqueous filled microcavity array platform modified with 10 mM hydroxyl terminated PEG thiol. (b) Nyquist plot of this substrate, unfunctionalised (red), post after functionalisation (grey), 60 min post modification (blue) 70 min post modification (green). All measurements were conducted using a 30 min μ CP time with 0.6 Pa pressure in PBS buffer at pH 7.4 within the experimental window of 20 hrs. A standard 3-electrode system at 0 V (vs Ag/AgCl) using an AC amplitude of 0.01 V with a frequency range of 1 MHz to 0.01 Hz.

The array was functionalised using 10 mM 6-mercaptohexanoic to support a DOPC membrane. As shown in the figure 3.15 below, the membrane resistance of the DOPC symmetric bilayer was found to be stable for 5 hrs.

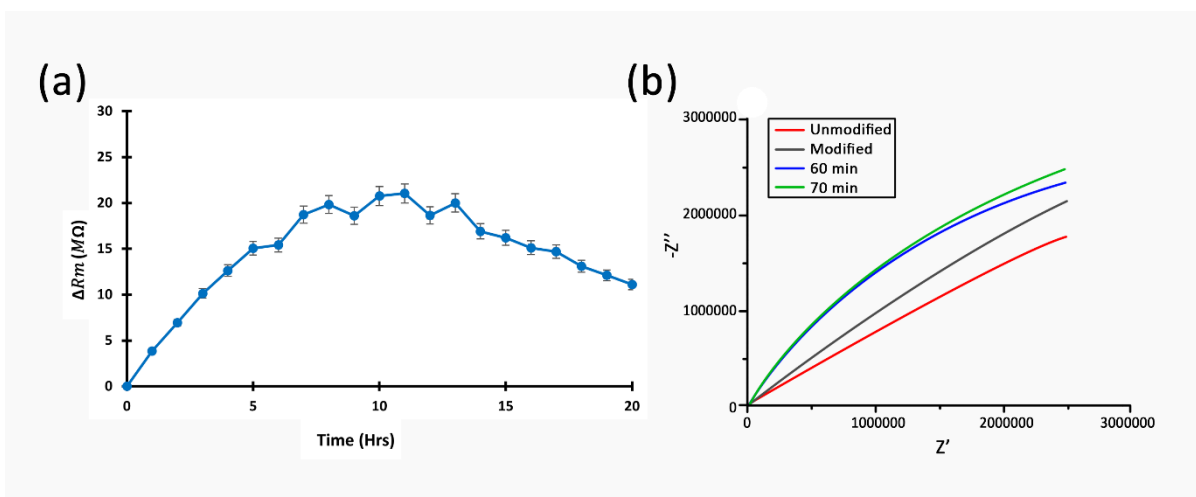


Figure 3.15: The relative change in resistance of a DOPC bilayer prepared using LB followed by vesicle fusion on a two-photon polymerised microcavities platform pre-aqueous filled microcavity array platform modified with 10 mM 6-mercaptopentanoic acid. (b) Nyquist plot of this substrate, unfunctionalised (red), post after functionalisation (grey), 60 min post modification (blue) 70 min post modification (green). All measurements were conducted using a 30 min μ CP time with 0.6 Pa pressure in PBS buffer at pH 7.4 within the experimental window of 20 hrs. A standard 3-electrode system at 0 V (vs Ag/AgCl) using an AC amplitude of 0.01 V with a frequency range of 1 MHz to 0.01 Hz

Membrane stability results from hydroxyl terminated end groups of both the 6-mercapto-1-hexanol and the hydroxyl terminated PEG thiol yielded similar results in terms of membrane stability of 8 hrs over a 20 hr period. This was expected as both SAMs terminated with the same hydroxyl terminated end group. In figure 3.15, 6-mercaptopentanoic acid with a carboxylic acid end termini had a shorter membrane stability of approximately 5 hrs in contrast to the hydroxyl terminated SAM.

The Nyquist plots, of 6-mercapto-hexanol, hydroxyl terminated PEG thiol and 6-mercaptopentanoic acid SAM formation on the gold interface was stable after 60 mins which suggests the difference in stability was due to the SAM end termini.

The change in membrane resistance between the two hydroxyl terminated SAMs was between 8 to 10 m Ω , were as for the carboxylic acid had a much greater change in membrane resistance between 16 to 18 m Ω . The similarity within the stability results within the two sections indicates that the array developed by electrochemical deposition along with the two-photon polymerised microcavities both offer a suitable means of supporting lipid membranes.

3.2.4 Determination of Lipid Bilayer formation and stability

3.2.4.1 Surface enhanced Raman Spectroscopy

Similar to section 2.2.3.1, the top surface of the two-photon polymerised microcavity array platform was modified with 10 mM 6-mercapto-1-hexanol using 30 min μ CP under 0.6 Pa. DOPC lipid membrane was formed using the Langmuir-Blodgett method on the microcavity array platform followed by vesicle fusion.

After the formation of a DOPC bilayer on the functionalised microcavity array, its presence and integrity was confirmed using Raman spectroscopy to evaluate permeation of the impermeable probe DRAQ7 into the cavities.¹⁴ A 785 nm wavelength was chosen as it coincides with DRAQ7 which is a cell impermeable dye and the anticipated plasmon excitation for the gold substrates. Figure 3.12 shows a spectrum of a DOPC bilayer supported by 10 mM 6-mercapto-1-hexanol on a microcavity array platform. Initially, a spectrum was taken after the five hours after bilayer formation with no vibrational modes from the DRAQ7 were evident.

After plasmonic disruption of the membrane, vibrational modes 429, 445 cm⁻¹ as well as 1240, 1280 and 1322cm⁻¹ which is unique to DRAQ7 are evident which indicates the presence of a lipid membrane. Vibrational modes 640, 850 and 980cm⁻¹ unique to DOPC further indicates the presence of a bilayer as it forms an effective barrier across the pores that is disrupted on application of plasmonic heating permitting DRAQ7 diffusion into the cavities.

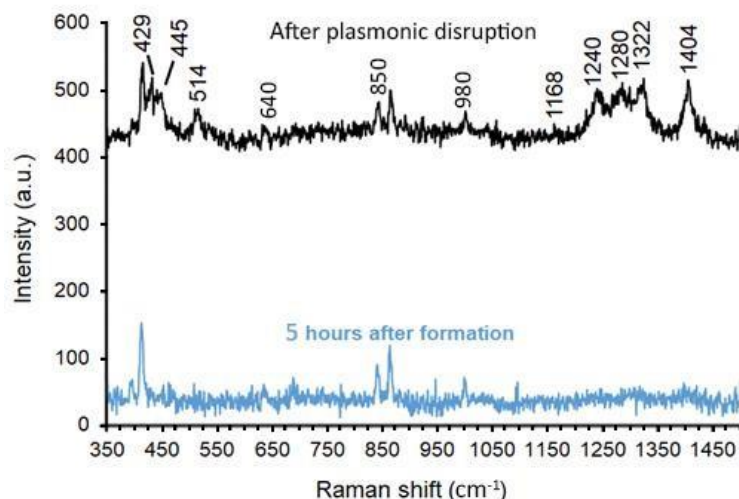


Figure 3.12: Shows an overlay of Raman spectras of a DOPC bilayer with 5 μM DRAQ7 using 785 nm excitation line at an incident laser power of 2.4 mW over two-photon polymerised microcavity array. The blue spectra was obtained within the five hours after the formation of a DOPC bilayer, with no DRAQ7 signatures detected. The black spectra is of DOPC bilayer after plasmonic disruption were DRAQ7 signatures seen. The array was functionalised using 10 mM 6-mercapto-1-hexanol for 30 min μCP time with 0.6 Pa pressure.

3.2.4.2 Cyclic Voltammetry of Lipid membrane on a gold array

Similar to section 2.3.3.2, cyclic voltammetry was used to investigate the surface coverage of the SAMs and lipid membranes on the electrode surface. Figure 3.16 shows CVs of a microcavity array, where the top surface is unmodified with the anodic peak being present at 0.250 V, another where the surface was modified by 10 mM 6-mercapto-1-hexanol using 30 min μCP with 0.6 Pa of pressure where the anodic peak shifted to 0.363 V, followed by the support of a lipid bilayer on the SAM coated array where the anodic shifted to 0.424 V.

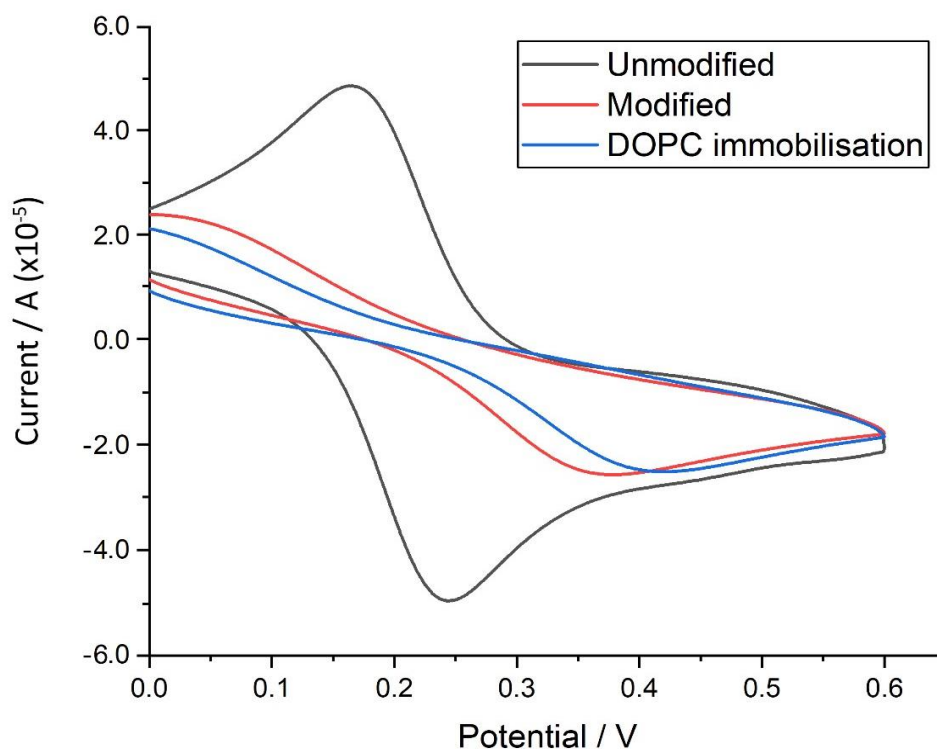


Figure 3.16: CVs of a two-photon polymerised microcavities array with 6-mercapto-1-hexanol on the top surface supporting a DOPC bilayer using LB followed by vesicle fusion on a PS lithographically prepared pre-aqueous filled microcavity array platform. The grey voltammogram is the unmodified array, red voltammogram is the array functionalised with 10 mM 6-mercapto-1-hexanol using a 30 min μ CP time with 0.6 Pa pressure and blue is the support of the DOPC lipid membrane. All electrodes were measured in triplicate using a standard 3 electrode set up in using 10 mM potassium ferricyanide in 1 M KCl as the supporting electrolyte and measured from 0 to 0.6 V (vs. Ag/AgCl) at a scan rate of 100 mV/s.

In figure 3.17, after the deposition of 10 mM hydroxyl terminated PEG thiol, the redox signal of the probe was no longer seen. This loss in redox signal seen in the voltammogram signifies a “blocking effect” by the modified surface, toward the redox probe and is greater compared to that of figure 3.16. The shift in position of the anodic peak of 0.253 V from the unmodified array to 0.41 V following the functionalisation of the array using hydroxyl terminated PEG thiol is 0.157 V in comparison to 0.113 V of figure 3.16.

Furthermore, after the addition of a DOPC membrane onto the array surface, there is almost complete suppression of the redox activity of the probe which indicates a continuous well packed membrane that effectively inhibits the permeation of small ions to the underlying gold surface.

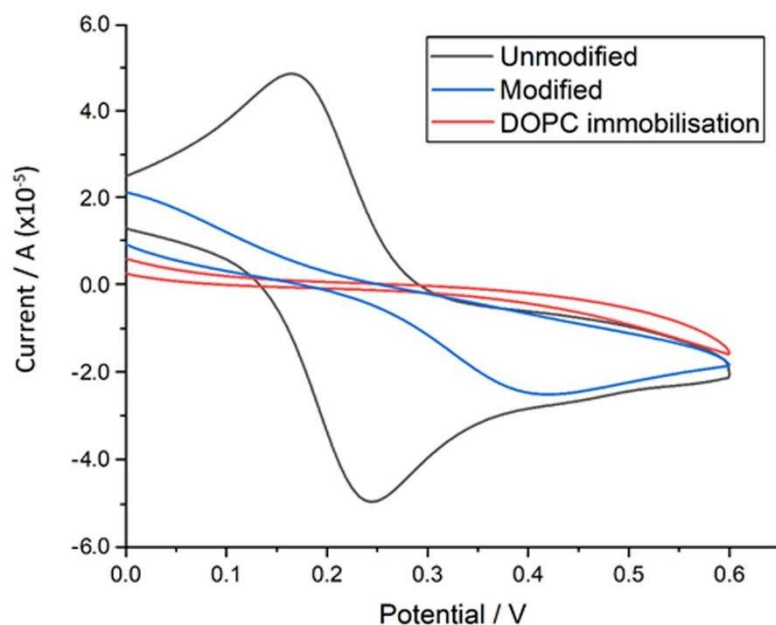


Figure 3.17: CVs of a two-photon polymerised microcavities array with hydroxyl terminated PEG thiol on the top surface supporting a DOPC bilayer using LB followed by vesicle fusion on a PS lithographically prepared pre-aqueous filled microcavity array platform. The grey voltammogram is the unmodified array, red voltammogram is the array functionalised with 10 mM hydroxyl terminated PEG thiol using a 30 min μ CP time with 0.6 Pa pressure and blue is the support of the DOPC lipid membrane. All electrodes were measured in triplicate using a standard 3 electrode set up in using 10 mM potassium ferricyanide in 1 M KCl as the supporting electrolyte and measured from 0 to 0.6 V (vs. Ag/AgCl) at a scan rate of 100 mV/s.

In figure 3.18 after the deposition of carboxylic terminated 10 mM 6-mercaptophexanoic acid. The shift in the anodic peak from 0.250 V to the functionalised array of 0.401 V. Furthermore, the addition of a DOPC membrane onto the array surface further suppressed the redox signal of the probe with the anodic peak shifting to 0.43 V.

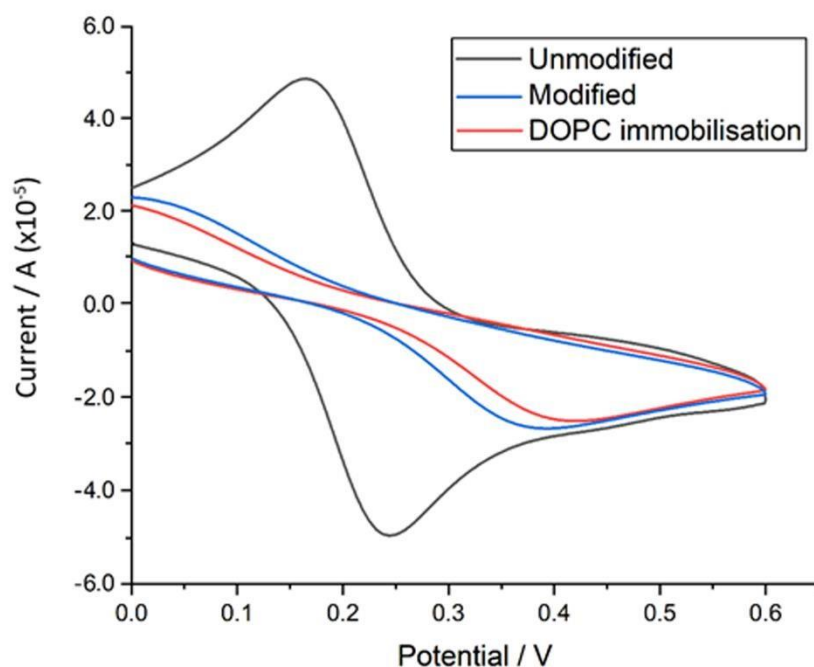


Figure 3.18: CVs of a two-photon polymerised microcavities array with 10 mM 6-mercaptohexanoic acid on the top surface supporting a DOPC bilayer using LB followed by vesicle fusion on a PS lithographically prepared pre-aqueous filled microcavity array platform. The grey voltammogram is the unmodified array, red voltammogram is the array functionalised with 6-mercaptohexanoic acid using a 30 min μ CP time with 0.6 Pa pressure and blue is the support of the DOPC lipid membrane. All electrodes were measured in triplicate using a standard 3 electrode set up in using 10 mM potassium ferricyanide in 1 M KCl as the supporting electrolyte and measured from 0 to 0.6 V (vs. Ag/AgCl) at a scan rate of 100 mV/s.

The hydroxyl terminated PEG thiol was able to block ferrocyanide oxidation in comparison to the 6-mercapto-1-hexanol and 6-mercaptohexanoic acid. These results demonstrate that the DOPC membrane is well assembled on hydroxyl terminated PEG thiol, allowing for a continuous well packed layer which effectively blocks the permeation of small ions to the underlying gold surface.

3.3 Conclusions

In closing, building on the current electrochemical deposited arrays as described in chapter 2, a two-photon polymerised microcavities platforms offers a unique electrochemical alternative to investigate SAMs with differing end termini to support lipid membranes. This is a much needed technique in which stable membranes applied on biomimetic platforms can be used in the pharmaceutical industry to assess drug membrane interactions. These experiments focused on improving MSLB by exploring the stability of a DOPC bilayer when various SAMs were used. These experiments demonstrated that 6-mercapto-1-hexanol was superior as a surface modifier in comparison to 6-mercaptohexanoic acid and hydroxyl terminated PEG thiol for bilayer stability. The MSLB platform provides a biomimetic environment allowing for stable lipid membranes to potentially be used in pharmaceutical and other sectors. EIS stability experiments show that DOPC membranes supported by the hydroxyl terminated PEG thiol to have greater stability but a smaller change in membrane resistance in comparison to 6-mercapto-1-hexanol and 6-mercaptohexanoic acid.

3.4 References

- (1) Mativenga, P. Micromachining. *CIRP Encyclopedia of Production Engineering* **2018**, 1–5. https://doi.org/10.1007/978-3-642-35950-7_17-4.
- (2) Ziaie, B.; Baldi, A.; Atashbar, M. Z. Introduction to Micro/Nanofabrication. In *Springer Handbook of Nanotechnology*; Bhushan, B., Ed.; Springer Handbooks; Springer: Berlin, Heidelberg, 2004; pp 147–184. https://doi.org/10.1007/3-540-29838-X_5.
- (3) Eschimese, D.; Vaurette, F.; Troadec, D.; Leveque, G.; Melin, T.; Arscott, S. Size and Shape Control of a Variety of Metallic Nanostructures Using Tilted, Rotating Evaporation and Lithographic Lift-off Techniques. *Sci. Rep.* **2019**, *9* (1), 7682. <https://doi.org/10.1038/s41598-019-44074-w>.
- (4) Šakalys, R.; Kho, K. W.; Keyes, T. E. A Reproducible, Low Cost Microfluidic Microcavity Array SERS Platform Prepared by Soft Lithography from a 2 Photon 3D Printed Template. *Sensors and Actuators B: Chemical* **2021**, *340*, 129970. <https://doi.org/10.1016/j.snb.2021.129970>.
- (5) Kotlarek, D.; Fossati, S.; Venugopalan, P.; Quilis, N. G.; Slabý, J.; Homola, J.; Lequeux, M.; Amiard, F.; Chapelle, M. L. de la; Jonas, U.; Dostálek, J. Actuated Plasmonic Nanohole Arrays for Sensing and Optical Spectroscopy Applications. *Nanoscale* **2020**, *12* (17), 9756–9768. <https://doi.org/10.1039/D0NR00761G>.
- (6) Sharma, N.; Keshmiri, H.; Zhou, X.; Wong, T. I.; Petri, C.; Jonas, U.; Liedberg, B.; Dostalek, J. Tunable Plasmonic Nanohole Arrays Actuated by a Thermoresponsive Hydrogel Cushion. *J. Phys. Chem. C* **2016**, *120* (1), 561–568. <https://doi.org/10.1021/acs.jpcc.5b10336>.

- (7) El Fissi, L.; Fernández, R.; García, P.; Calero, M.; García, J. V.; Jiménez, Y.; Arnau, A.; Francis, L. A. OSTEMER Polymer as a Rapid Packaging of Electronics and Microfluidic System on PCB. *Sensors and Actuators A: Physical* **2019**, *285*, 511–518. <https://doi.org/10.1016/j.sna.2018.11.050>.
- (8) Bartlett, P. N.; Baumberg, J. J.; Birkin, P. R.; Ghanem, M. A.; Netti, M. C. Highly Ordered Macroporous Gold and Platinum Films Formed by Electrochemical Deposition through Templates Assembled from Submicron Diameter Monodisperse Polystyrene Spheres. *Chem. Mater.* **2002**, *14* (5), 2199–2208. <https://doi.org/10.1021/cm011272j>.
- (9) Jose, B.; Steffen, R.; Neugebauer, U.; Sheridan, E.; Marthi, R.; J. Forster, R.; E. Keyes, T. Emission Enhancement within Gold Spherical Nanocavity Arrays. *Phys. Chem. Chem. Phys.* **2009**, *11* (46), 10923–10933. <https://doi.org/10.1039/B908385E>.
- (10) Gimenez, A. V.; Kho, K. W.; Keyes, T. E. Nano-Substructured Plasmonic Pore Arrays: A Robust, Low Cost Route to Reproducible Hierarchical Structures Extended across Macroscopic Dimensions. *Nanoscale Adv.* **2020**, *2* (10), 4740–4756. <https://doi.org/10.1039/D0NA00527D>.
- (11) Robinson, J.; Berselli, G. B.; Ryadnov, M. G.; Keyes, T. E. Annexin V Drives Stabilization of Damaged Asymmetric Phospholipid Bilayers. *Langmuir* **2020**, *36* (19), 5454–5465. <https://doi.org/10.1021/acs.langmuir.0c00035>.
- (12) McConnell, N. Microcavity Supported Lipid Bilayers; Biomimetic Models of the Cell Membrane. 164.

- (13) Gufler, P. C.; Pum, D.; Sleytr, U. B.; Schuster, B. Highly Robust Lipid Membranes on Crystalline S-Layer Supports Investigated by Electrochemical Impedance Spectroscopy. *Biochimica et Biophysica Acta (BBA) - Biomembranes* **2004**, *1661* (2), 154–165. <https://doi.org/10.1016/j.bbamem.2003.12.009>.
- (14) Akagi, J.; Kordon, M.; Zhao, H.; Matuszek, A.; Dobrucki, J.; Errington, R.; Smith, P. J.; Takeda, K.; Darzynkiewicz, Z.; Wlodkowic, D. Real-Time Cell Viability Assays Using a New Anthracycline Derivative DRAQ7®. *Cytometry A* **2013**, *83* (2), 227–234. <https://doi.org/10.1002/cyto.a.22228>.

Chapter 4: Future applications of microcavity array platform

This thesis focuses on developing a rapid and easy means to selectively functionalise pore arrays designed for bilayer support with bilayer stability promoted by self-assembled monolayers.

Microcavity array methods were developed and compared at two different pore array substrates with SAMs with different end terminus through a new microcontact printing (μ CP) method.

Chapter 2 details the fabrication of sphere lithography electrochemically deposited array followed by an investigation of the use of different SAM end termini through μ CP to support a lipid bilayer.

Initial studies focused on simple planar gold substrates where it was found the μ CP method was just as effective in surface modification as the solution deposition method. Following the optimisation of μ CP parameters, electrochemical impedance spectroscopy (EIS) stability experiments shows that DOPC membranes supported by hydroxyl terminated PEG thiol to show greater stability than that of 6-mercapto-1-hexanol and 6-mercaptohexanoic acid.

Chapter 3 describes the transition from the Polystyrene spheres (PS) lithography electrochemical deposited array towards the fabrication two-photon polymerised microcavity array. This transition towards the two-photon polymerised microcavity array showed an improvement in cavity size reproducibility in comparison to the PS lithography microcavity array. It describes the use of μ CP on different SAM end termini used in chapter 2 on lipid membrane stability. The optimisation of the nanostructures at the bottom of the cavity array along with hydroxyl terminated PEG thiol allowing for a stable biomimetic environment offers the platforms use as a drug permeation model in the pharmaceutical sector. EIS stability experiments showing that DOPC membranes supported by the hydroxyl terminated PEG thiol to have greater stability and also a smaller change in membrane resistance in comparison to 6-mercapto-1-hexanol and 6-mercaptohexanoic acid.

Cyclic Voltammetry, (CV) also demonstrated that the DOPC membrane was continuous and well packed on hydroxyl terminated PEG thiol in comparison to 6-mercapto-1-hexanol and 6-mercaptohexanoic acid on both platforms.

In chapter 3 drug permeation studies would be the next logical step after the optimisation of the stability of lipid membranes on the two-photon polymerised microcavity array. Next, it would be interesting to compare drug permeation of a lipid bilayer spanned over two-photon polymerised microcavity array platform supporting cells. Figure 4.1 below shows CVs of gold cavity array platforms functionalised using Collagen IV through μ CP in 10 mM potassium ferricyanide at different time intervals while figure 4.2 shows cyclic voltammograms of microcavity array platform using 30 min μ CP time using different pressures.

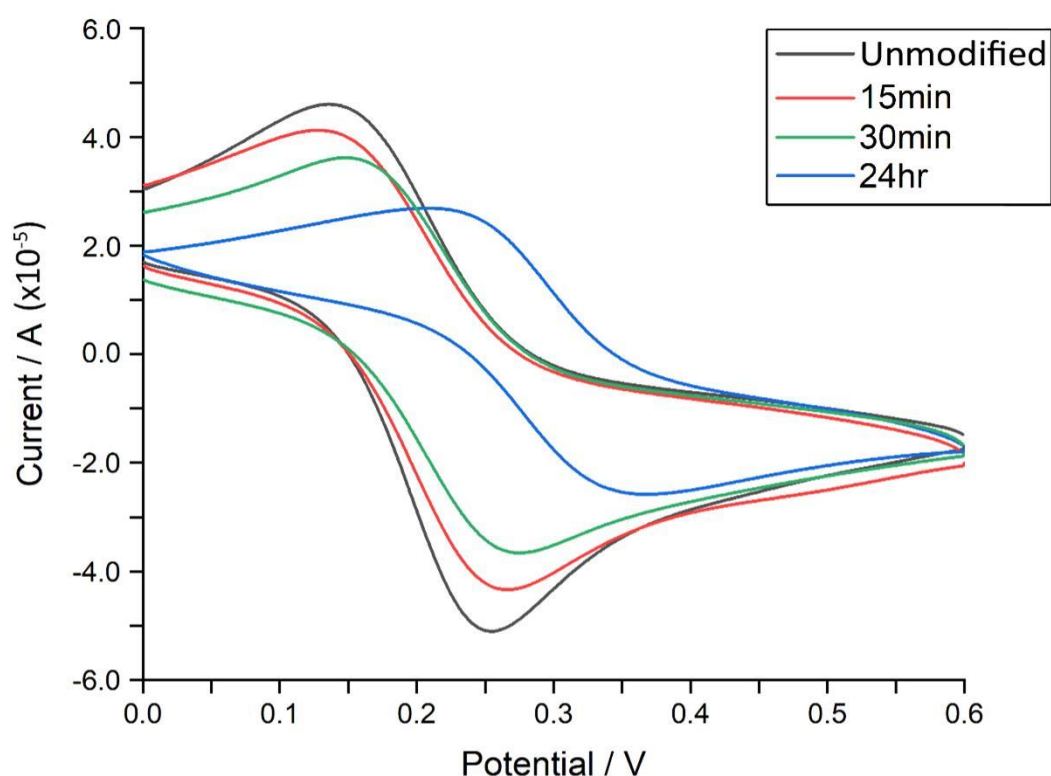


Figure 4.1: Comparison of voltammetry of two-photon polymerised microcavities platform at different μ CP time intervals using Collagen IV. Where the grey is no an unmodified array, red is coverage after 15 min μ CP, blue is coverage after 30min μ CP and green is coverage after 24 hr μ CP. All electrodes where measured using a standard 3 electrode set up in using 10 mM potassium ferricyanide in 1 M KCl as the supporting electrolyte and measured from 0 to 0.6 V (vs. Ag/AgCl) at a scan rate of 100 mV/s.

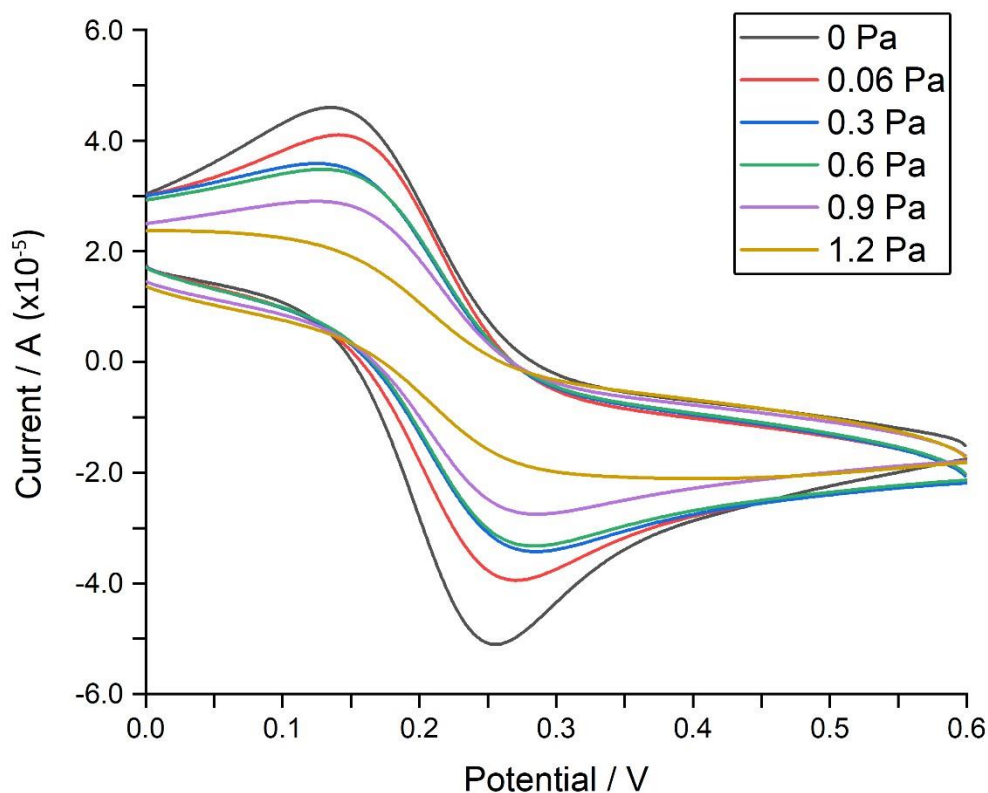


Figure 4.2: Comparison of voltammetry of two-photon polymerised microcavities platform at different μ CP pressure intervals of Collagen IV using cyclic voltammetry. Where the grey is the CV of 30 min contact with no pressure, red CV is of 30 min contact with 0.06 Pa, blue CV is 30 min contact with 0.3 Pa, green CV is of 30 min contact with 0.6 Pa, purple CV is of 30 min contact with 0.9 Pa and gold CV is of 30 min contact with 1.2 Pa. All electrodes were measured using a standard 3 electrode set up in using 10 mM potassium ferricyanide in 1 M KCl as the supporting electrolyte and measured from 0 to 0.6 V (vs. Ag/AgCl) at a scan rate of 100 mV/s

Collagen is the most common protein within the body which provides structural support in connective tissue. It is abundant in the extracellular matrix and behaves as a signalling beacon through biomolecular interactions.^{1,2} The functionalisation of the two-photon polymerised array with the natural protein scaffold further improves the biomimetic properties of the array.

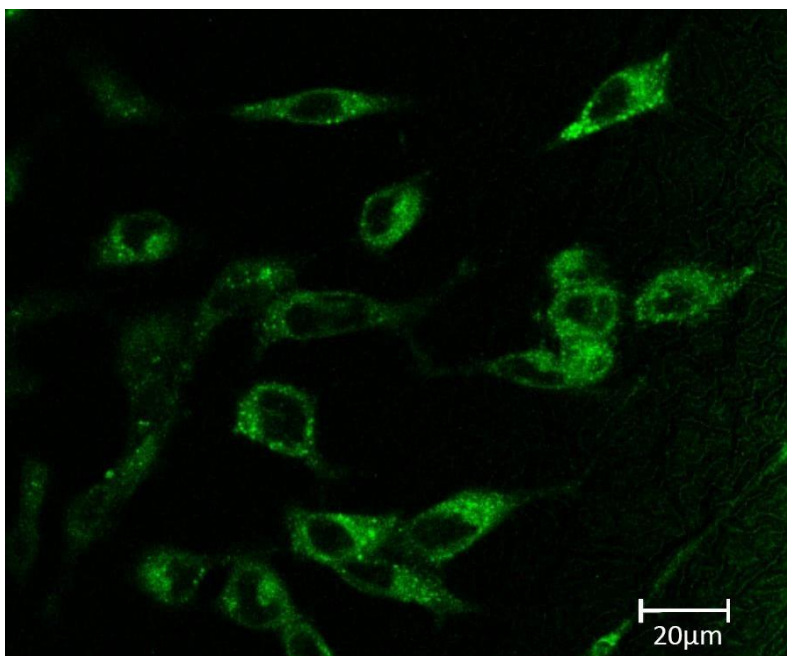


Figure 4.3: Confocal imaging of A549 cells on two-photon polymerised microcavity array functionalised using Collagen IV using 30 min μ CP under 0.6 Pa and 10 μ M Dppz – Ar – BODIPY courtesy of Darragh O’Connor. The excitation and emission wavelengths (λ_{ex} / λ_{em}) were 498/511–570 nm.

4.1 References

- (1) Alberts, B.; Johnson, A.; Lewis, J.; Raff, M.; Roberts, K.; Walter, P. *Molecular Biology of the Cell*, 4th ed.; Garland Science, 2002.
- (2) Valiente-Alandi, I.; Schafer, A. E.; Blaxall, B. C. Extracellular Matrix-Mediated Cellular Communication in the Heart. *J. Mol. Cell. Cardiol.* **2016**, *91*, 228–237. <https://doi.org/10.1016/j.yjmcc.2016.01.011>.

